Synthesis, electrochemistry and application of 2D and 3D graphene-composite materials

Gao, Hongcai

2013

Gao, H. (2013). Synthesis, electrochemistry and application of 2D and 3D graphene-composite materials. Doctoral thesis, Nanyang Technological University, Singapore.

https://hdl.handle.net/10356/54847

https://doi.org/10.32657/10356/54847

NANYANG TECHNOLOGICAL UNIVERSITY

SYNTHESIS, ELECTROCHEMISTRY AND APPLICATION OF 2D AND 3D GRAPHENE-COMPOSITE MATERIALS

GAO HONGCAI

School of Chemical and Biomedical Engineering

2013

SYNTHESIS, ELECTROCHEMISTRY AND APPLICATION OF 2D AND 3D GRAPHENE-COMPOSITE MATERIALS

GAO HONGCAI

School of Chemical and Biomedical Engineering

A thesis submitted to the Nanyang Technological University
in fulfilment of the requirement for the degree of
Doctor of Philosophy

2013

ACKNOWLEDGEMENTS

Foremost, my special thanks go to Nanyang Technological University for providing me the scholarship to undertake the Ph.D. program with full research scholarship throughout these years.

Sincerely, I want to thank my main advisor, Asst Prof Duan Hongwei, for his intellectual support, guidance and encouragement during my studies. In addition to the breadth of his knowledge, Dr. Duan has been a source of careful and thoughtful discussion that was the key to the development of my research work. Furthermore, he also allowed us great freedom in project advancement and management, which greatly benefited me. I also thank my co-supervisor, Prof. Ching Chi Bun, who initiated the project and gave me plenty of valuable advice. It has been a great honor to train with them.

My laboratory colleagues have also been instrumental in broadening my thoughts, providing an environment conducive to the rapid exchange of ideas and support. I would also want to thank Dr. Xiao Fei, Dr. Sun Yimin, Dr. Fang Zheng, Song Jibin, Zan Xiaoli, and Zhou Jiajing for their generous help. Working with them is a wonderful experience while sharing their knowledge on research.

Many thanks also go to Dr. Wang Xiujuan and some of my friends, Dr. Yuan Jifeng, Hong Jindui, Xue Tong, and Huang Ke, for their continuous support and encouragement through all these years in the University.

Finally, I will give my utmost thanks to my family. They have always been supportive to me especially when I felt frustrated during the experiments. Thanks to their selfless love, care, and encouragement throughout these years.

And most of all, I must express special thanks to my loved wife, for her understanding, support, patience, and love.

TABLE OF CONTENTS

SUMMARY

Graphene materials represent promising candidates in the field of electrochemistry. In addition, they are also versatile building blocks that can be self-assembled into macroscopic 2D and 3D graphene materials, such as graphene films, graphene papers, graphene hydrogels, and graphene foams. Herein, we prepared 2D and 3D macroscopic graphene materials and their composites by several approaches, including electrochemical, vacuum filtration, and chemical reduction. We also demonstrated their electrochemical applications as biosensors, fuel cells, and supercapacitors.

We first prepared PtNi alloy nanoparticles modified graphene film through a facile and green one-step electrochemical reduction process from GO and metal precursors, by which well-dispersed alloy nanoparticles with high density were loaded on the electrochemically reduced GO (ERGO) . When used for glucose sensing, we found that the PtNi-ERGO nanocomposite based nonenzymatic sensor possesses many merits in terms of high selectivity, superior resistance to poisoning, low detection limit, rapid response, excellent reproducibility and stability, which outmatches the performance of other nonenzymatic Pt-based glucose sensors that have been reported previously. The combination of these unique characters has enabled the application of this new type of nanoelectrocatalyst loaded electrodes for real human samples.

We then fabricated a free-standing electrode by electrodeposition of Cu nanocubes on graphene paper (GP). The resultant Cu-GP electrode exhibits remarkable catalytic activity and stability towards the oxidation of hydrazine. An in-situ formed thin layer of Cu hydroxide/oxide on Cu nanocube surfaces

can lower the overpotential and stabilize the catalyst in alkaline conditions. A totally-irreversible and diffusion-controlled oxidation of hydrazine occurs on Cu-GP with nitrogen and water as the reaction products. The use of free-standing Cu-GP electrodes directly for direct hydrazine fuel cells (DHFC) would greatly simplify the manufacturing of electrode assemblies of fuel cells and offers new possibilities for the development of flexible power sources.

We then incorporated CNTs and Mn_3O_4 nanoparticles into graphene papers to construct flexible and all-solid-state asymmetric supercapacitors with a polymer gel electrolyte. The flexible device, benefiting from the remarkable electrical and mechanical properties of graphene papers, the functionalities of CNTs and Mn_3O_4 nanoparticles, and the excellent electrochemical properties of polymer gel electrolyte, have demonstrated extraordinary performance for supercapacitor applications, such as significantly improved energy density and excellent cycling performance. The integration of chemically tunable components of graphene, CNTs, functional nanoparticles, and polymer gel electrolytes opens the possibility for further screening of functional nanomaterials towards flexible and portable supercapacitors, batteries, fuel cells, biosensors, and other electronic devices.

At last, we synthesized graphene hydrogel (GH) with 3D interconnected pores by reducing GO with an eco-friendly reagent under mild conditions. Vertically-aligned MnO_2 nanoplates were uniformly deposited on porous nickel foam under cathodic conditions. We then fabricated asymmetric supercapacitor by employing these two kinds of materials as negative and positive electrodes, respectively. Benefitting from 3D GH with well-preserved graphene sheets, vertically-aligned MnO_2 nanoplates with sufficient free spaces, and the robust

contact between MnO_2 and nickel foam, the asymmetric supercapacitor of GH//MnO_2-NF exhibits stable cycling performance and remarkable energy density. Such asymmetric supercapacitor offers great promise in the application of energy storage systems with high-performance arising from the advantages of low-cost, facile fabrication process, improved energy and power density, as well as eco-friendly nature.

LIST OF FIGURES

LIST OF ABBREVIATIONS

AA	ascorbic acid
AAP	acetaminophen
AFM	atomic force microscopy
AP	acetamidophenol
BET	Brunauer-Emmett-Teller
BJH	Barrett-Joyner-Halenda
CNTG	carbon nanotubes-reduced graphene oxide
CNTs	carbon nanotubes
CRGO	chemically reduced graphene oxide
CV	cyclic voltammetry
CVD	chemical vapor deposition
DCE	1,2-dichloroethane
DHFC	direct hydrazine fuel cells
DMSO	dimethyl sulfoxide
EDS	energy dispersive X-ray spectroscopy
EIS	electrochemical impedance spectroscopy
EPD	electrophoretic deposition
ERGO	electrochemically reduced graphene oxide
fcc	face-centered cubic
FT-IR	Fourier transform infrared
FTO	fluorine tin oxide
GCE	glassy carbon electrode
GH	graphene hydrogel

GO	graphene oxide
GP	graphene paper
GP	graphene paper
ITO	indium tin oxide
LbL	layer-by-layer
LFP	lithium ion phosphates
LSV	linear sweep voltammetry
LTO	lithium titanium oxide
MG	Mn_3O_4 nanoparticles-reduced graphene oxide
MPTMS	3-mercaptopropyl trimethoxysilane
NF	nickel foam
NO	nitric oxide
OPH	organophosphorous hydrolase
PAAK	potassium polyacrylate
PAH	poly(allylamine hydrochloride)
PANI	polyaniline
PB	prussian blue
PBS	phosphate buffer solution
PDDA	poly(diallydimethylammonium)
PEI	poly(ethyleneimine)
PPY	polypyrrole
PS	polystyrene
PSS	poly(sodium 4-styrene sulfonate)
PTFE	polytetrafluoethylene
PVA	poly(vinyl alcohol)

PVDF	polyvinylidene fluoride
PZC	point of zero charge
rGO	reduced graphene oxide
RSD	relative standard deviation
SCE	saturated calomel electrode
SEM	scanning electron microscopy
SPI	sulfonated polyimide
STM	scanning tunneling microscopy
SWNTs	single-walled carbon nanotubes
UA	uric acid
UV	ultraviolet
XPS	X-ray photoelectron spectroscopy
XRD	X-ray Diffraction

PUBLICATIONS

[1] Gao HC, Xiao F, Ching CB, Duan HW. 2012. Flexible All-Solid-State Asymmetric Supercapacitors Based on Free-Standing Carbon Nanotube/Graphene and Mn_3O_4 Nanoparticle/Graphene Paper Electrodes. *ACS Appl Mater Interfaces* 4:7019-7025.

[2] Gao HC, Xiao F, Ching CB, Duan HW. 2012. High-Performance Asymmetric Supercapacitor Based on Graphene Hydrogel and Nanostructured MnO_2. *ACS Appl Mater Interfaces* 4:2801-2810.

[3] Gao HC, Wang YX, Xiao F, Ching CB, Duan HW. 2012. Growth of Copper Nanocubes on Graphene Paper as Free-Standing Electrodes for Direct Hydrazine Fuel Cells. *J Phys Chem C* 116:7719-7725.

[4] Gao HC, Xiao F, Ching CB, Duan HW. 2011. One-Step Electrochemical Synthesis of PtNi Nanoparticle-Graphene Nanocomposites for Nonenzynnatic Amperometric Glucose Detection. *ACS Appl Mater Interfaces* 3:3049-3057.

[5] Xiao F, Li YQ, Gao HC, Ge SB, Duan HW. 2013. Growth of coral-like PtAu-MnO_2 binary nanocomposites on free-standing graphene paper for flexible nonenzymatic glucose sensors. *Biosens Bioelectron* 41:417-423.

[6] Yuan JF, Gao HC, Sui JJ, Duan HW, Chen WN, Ching CB. 2012. Cytotoxicity Evaluation of Oxidized Single-Walled Carbon Nanotubes and Graphene Oxide on Human Hepatoma HepG2 cells: An iTRAQ-Coupled 2D LC-MS/MS Proteome Analysis. *Toxicol Sci* 126:149-161.

[7] Xiao F, Song JB, Gao HC, Zan XL, Xu R, Duan HW. 2012. Coating Graphene Paper with 2D-Assembly of Electrocatalytic Nanoparticles: A

Modular Approach toward High-Performance Flexible Electrodes. *ACS Nano* 6:100-110.

[8] Yuan JF, Gao HC, Sui JJ, Chen WN, Ching CB. 2011. Cytotoxicity of single-walled carbon nanotubes on human hepatoma HepG2 cells: An iTRAQ-coupled 2D LC-MS/MS proteome analysis. *Toxicol Vitro* 25:1820-1827.

[9] Yuan JF, Gao HC, Ching CB. 2011. Comparative protein profile of human hepatoma HepG2 cells treated with graphene and single-walled carbon nanotubes: An iTRAQ-coupled 2D LC-MS/MS proteome analysis. *Toxicol Lett* 207:213-221.

1. Introduction

1.1 Introduction of graphene

Continuous efforts have been devoted into the theoretical analysis and experimental investigation of layered graphite materials [1]. As early as 1960s, single-layered graphene oxide (GO) was prepared by dispersing of graphite oxide into diluted aqueous NaOH solution. The oxygen functional groups dissociated in alkaline conditions resulted in the formation of negatively charged graphite oxide sheets. The electrostatic repulsion forces between these sheets drove the formation of single-layered GO [2]. In 1970s, Blakely et al. found that carbon dissolved in transition metals can form mono- and multi-layered carbon film on the top-surface of these metals possibly due to the phase separation of the components [3]. This layered carbon was confirmed by scanning tunneling microscopy (STM) almost twenty years later [4]. Very recently, increasing attention has been paid on this two-dimensional material since 2004 when single-layered graphene was obtained by the Scotch-tape approach [5]. The graphene sheets with 2D layered structure comprised by sp^2-hybridized carbon atoms possesses unique chemical and physical properties, and therefore may play an evolutional role in the fields of electronics, energy, environment, and health sciences. The electron mobility of graphene can reach 2.0×10^5 cm^2 V/s at low temperatures because of the weak electron-photon interactions [6]. Single-layered structure endows graphene sheets with very high theoretical specific surface area (2630 m^2/g) [7]. The graphene materials also exhibit excellent thermal stability at high temperatures of about 2600 K [8], thermal conductivity between 3080 to 5150 W/mK [9], remarkable mechanical

strength with Young's modulus of around 1.0 TPa [10], and outstanding optical transmittance of 97.7% [11]. To realize its practical applications, it is a crucial issue to develop environmentally-benign and efficient methods to achieve the production of graphene and its composites.

1.2 Preparation of graphene

Although the scotch-tape method can directly produce high-quality and single-layered graphene, it is not suitable for large-scale applications. Several alternative approaches have been developed to produce large amounts of graphene materials, including epitaxial growth [12], sonication-assisted liquid-phase exfoliation [13], chemical exfoliation [14], chemical vapor deposition (CVD) [15], and organic synthesis [16].

Epitaxial growth and CVD methods are suitable to produce high quality and large area graphene sheets, however, the chemical rout to produce graphene materials via oxidation-exfoliation-reduction of graphite powder has aroused the most intense research interest, because of its unique advantages including high productivity, facile post functionalization, tunable properties of resulting composites, and ease of operation in solution without the need for special equipments (**Figure 1.1**) [17]. This method involves the chemical oxidation of graphite into graphite oxide, followed by exfoliation of graphite oxide into single layer graphene oxide (GO), and chemical reduction of GO into reduced graphene oxide (rGO) [18].

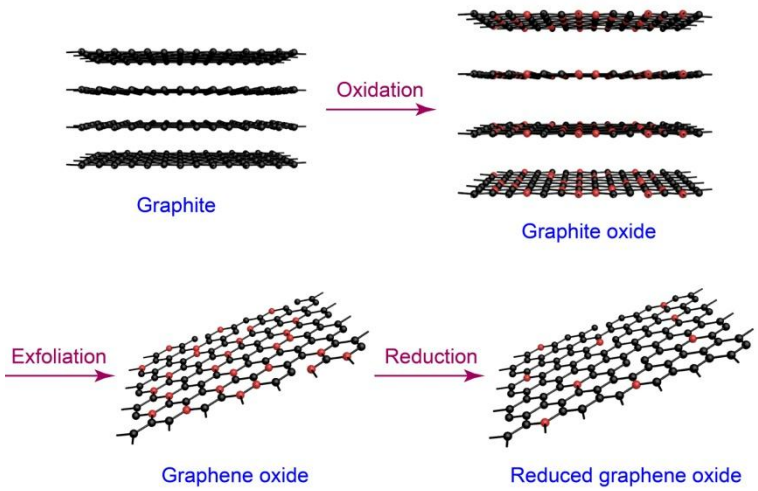

Figure 1.1 The oxidation-exfoliation-reduction approach for the preparation of reduced graphene oxide from graphite.

1.2.1 Preparation of graphene oxide

Various oxidants have been applied for the oxidation of graphite powder into graphite oxide. The history for the preparation of graphite oxide can be dated back to as early as 1859, when $KClO_3$ and fuming HNO_3 were used to oxidize graphite powder and led to the formation of a material with carbon to oxygen ratio around 2 :1 [19]. The method using $KClO_3$ and HNO_3 as oxidation agents must be handled with special caution because of the generation of highly toxic gas of chlorine dioxide (ClO_2) and the possible production of explosions [20].

In 1958, an alternative approach was developed by Hummers et al. to synthesize graphite oxide with similar level of oxidation where $NaNO_3$, $KMnO_4$ and concentrated H_2SO_4 were used as oxidation agents [21]. This method can avoid the generation of hazardous ClO_2 gas, can be completed within relatively shortened reaction time, and therefore is widely adopted for the preparation of graphite oxide. The application of additional mechanical energy input, such as

mechanical shaking and sonication, can to promote the exfoliation of graphite oxide into single- or few-layered graphene oxide [22, 23].

1.2.2 Reduction of graphene oxide

In the preparation of graphite oxide, the oxidation process of graphite by strong oxidants leads to the formation of disrupted sp^2 bonding networks, and hence both of the oxidation products including graphite oxide and graphene oxide are electrically insulating materials. The chemical structure of GO can be described as graphene sheets with epoxy, carboxyl, and hydroxyl groups [24]. A reduction process can be applied to recover the electrical conductivity by restoring the π-network, and the product of this reaction is usually termed as reduced graphene oxide (rGO). The reduction process can be achieved through a number of approaches, including chemical [25], electrochemical [26], microwave [27], photochemical [28], photothemal [29] and microbial reductions [30]. One of the approaches can also be possibly coupled with another in order to achieve higher reduction efficiencies of GO. For example, when some eco-friendly chemicals (e.g., hydrogen peroxide and ammonium peroxy disulfate) are combined with a microwave irradiation, high quality graphene is obtained from natural graphite directly within a short reaction time of 3 min [27].

Chemical reduction of GO. GO can be reduced by a wide range of synthetic and natural reagents. The advantage of chemical reduction method is that it can be carried out at relatively low temperature or with only moderate heating. In addition, the requirement for equipments of this reduction approach is not as crucial as other methods including thermal, photo, and microwave reduction. In 1960s, chemical reduction was carried out by $TiCl_3$ and NaI in

acetic anhydride, leading to the reduced oxide with carbon to oxygen atomic ratio of 7 [31]. Hydrazine was used for the reduction of graphite oxide even before the successful preparation of single-layered graphene [32]. Then hydrazine was applied for the reduction of graphene oxide and proves to be one of most efficient agents to remove oxygen functionalities on GO [25, 33]. The reduction by hydrazine can lead to the formation of rGO with relatively high carbon to oxygen atomic ratio of 12.5 and excellent electrical conductivity of 99.6 S/cm [34]. Metal hydride is another kind of reducing agents, however, their reactivity with water limits their applications in the reduction of GO usually dispersed in water. Until recently, the successful reduction of GO was achieved by freshly prepared solution of sodium borohydride ($NaBH_4$) [24]. The additional advantage of using borohydride is that fewer heteroatoms are possibly introduced into reducing products than hydrazine. Nevertheless, the alcohol groups on GO cannot be efficiently removed by $NaBH_4$ because of its low activity for the reduction of expoxy and carboxy groups.

In addition, these two strong reducing agents are both highly toxic which limits their practical applications for large scale production of rGO. Therefore, a number of environmentally-benign chemicals have also been developed as the reducing agents for GO, including hydrogen iodide [35], ascorbic acid [36], alkaline solution [37], glutathione [38], urea [39], amino acids [40], dopamine [41], iron power [42], aluminum powder [43], zinc powder [44], low valence metal ions [45], reducing sugar [46], tea water [47], and carrot root [48]. Among them, ascorbic acid can be accepted as the ideal substitute for hydrazine and $NaBH_4$ due to its non-toxicity, remarkable stability in water, and high deoxygenation efficiency. The atomic ratio in the prepared rGO can be as high

as 12.5 when using ascorbic acid as the reducing agent, which is comparable to that of prepared by hydrazine reduction [34].

Another chemical reduction method is hydrothermal or solvethermal reduction. For the hydrothermal reduction method, the oxygen functional groups on GO are removed in pure aqueous or organic solvents without the addition of any reducing reagents. However, long reaction time (typically more than 12 h) and high pressure are usually required for this reduction method. Hydrothermal conditions can generate protons from water, and the hydrothermal reduction mechanism of GO can be considered similar to the proton catalyzed dehydration reaction of alcohols [49]. Because of the reversible properties of proton catalyzed dehydration and hydration reactions, there should always be some residual oxygen functionalities on rGO even at the end of the reactions. Simultaneous exfoliation and reduction of graphite oxide can be achieved by thermal annealing method with the formation of rGO.

Electrochemical reduction of GO. Electrochemical reduction of GO is typically achieved by applying a negative potential to a GO film casted on a conducting substrate. The electrochemical reduction of GO has several advantages in comparison with chemical and thermal reduction methods [50]. First, this method using electrons acting as the reductant agent is intrinsically environmentally-friendly, and possibly leads to the formation of rGO without heteroatoms contaminations by eliminating the need for toxic reducing chemicals. Furthermore, highly negative potentials, readily obtainable by simply adjusting the electrochemical parameters, are beneficial for the removal of more oxygen functionalities and the production of rGO with high qualities. At last, the resulting rGO is usually in good contact with an electrically

conductive substrate, which simply the electrode fabrication process and is suitable for further electrochemical applications [51].

On the other hand, cathodic electrodeposition has also been widely employed to prepare a wide range of metal or metal oxide particles on conducting substrates, therefore, it is also possible to prepare metal or metal oxide nanoparticle modified rGO through a one-step manner under cathodic conditions [26, 52]. The prepared nanoparticles were directly immobilized on the surface of rGO without any linker molecules, which can facilitate the electron transfer between these two components.

Thermal reduction of GO. The early studies showed that upon heating, graphite oxide can release H_2O, CO, and CO_2, which may represent the carbonization or graphitization of carbon materials [53, 54]. The successful exfoliation of single-layered graphene relies on the sufficient oxidation of graphite and the adequate pressure systems during the direct thermal treatment process [55]. Therefore, some special equipments are generally necessary in order to obtain rapid heating rates (typically 2000 ℃/min), high temperatures of about 800-1000 ℃, and inert atmospheres (usually high vacuum, argon gas, or hydrogen gas) [56]. A number of products can be generated from the rapid temperature increase, including carbon dioxide, carbon monoxide, water, and other small hydrocarbon molecules from the oxygen functional groups on graphite oxide. These generated gases at high temperatures can create a huge pressure increase between the stacked layers, and eventually result in the exfoliation of stacked platelets [57].

Microwave and photo irradiation represent another two kinds of thermal resources applied for the reduction of GO. Compared with the traditional thermal heating methods, uniform and rapid thermal heating can be generated by microwave irradiation within a short time at ambient conditions [58]. The microwave heating can also promote chemical reactions by lowering the activation energies.

Through either the chemical reduction method or the conventional heating method, it is challenging to reduction GO if it is mixed with or incorporated into other materials, such as polymers. Since the presence of polymers may prevent the reducing agents from fully reduction of GO, or it may be not stable upon heating at high temperatures. Inspired by the flash reduction of GO where a small amount of thermal energy led to the sufficient removal of oxygen functional groups [59], photothemal reduction of GO was developed [29]. It was found that a camera flash can provide 9 times of thermal energy needed for heating GO above 100 ℃, which is more than sufficient to initiate the thermal deoxygenation of GO. In addition, the photothermal method also enables patterning GO or GO/polymer films by flashing through a photomask, which has aroused widespread interest [60].

Photo catalyzed reduction of GO. The typical inorganic photocatalysts, including semiconductors (ZnO and TiO_2) (**Figure 1.2**) [28, 61] and plasmonic metal nanoparticles (Ag nanoparticles) [62], were also successfully used in the UV-assisted reduction of GO. However, these inorganic materials cannot be easily removed from the prepared rGO sheets, possibly affecting the properties and limiting the application fields of the resulting materials. The development of organic photocatalysts is a promising way to tackle these problems. Clean

rGO sheets were prepared with the aid of a photocatalyst of Hantzsch 1,4-dihydropyridine (HEH) under UV irradiations. rGO prepared by the photo-induced reduction method exhibits the comparable electrical conductivity (46.8 S/cm) to rGO prepared by hydrazine reduction [63].

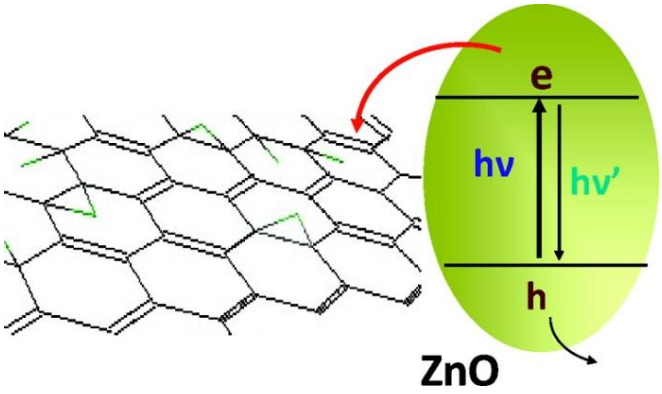

Figure 1.2 Illustration of the mechanisms of photochemical induced electron transfer from photocatalyst ZnO to GO [61].

Microbial reduction of GO. The microbial technology was first achieved for reduction of GO in a strictly anaerobic environment [64]. However, a following work found that the anaerobic condition is not necessary for the microbial reduction [30]. In both works, GO was reduced by a dissimilatory metal-reducing bacteria, e.g. *Shewanella* cells. These cells can generate electrons in the metabolic process, and these electrons are transferrable by the anaerobic respiration of the cells from the cell interior to electron acceptors in the environments, for example, solid metal oxide particles. The cell membrane of c-type cytochromes plays a role in promoting the direct electron transfer to GO, and the redox active species produced by the cells also function as electron transfer mediators. Both of the direct and indirect pathways are likely involved in the process of extracellular electron transfer [30]. Recently, the reduction of GO by cells of *Escherichia Coil* was also reported in anaerobic conditions

containing glucose, and the glycolysis process from the metabolic activity of the cells is possibly involved in the reduction of GO [65].

1.3 Self-assembly of graphene

There is a variety of interactions between GO/rGO sheets and their composites, including hydrogen bonding, ionic, amphiphilic, and π-π interactions. Because of the presence of these interactions, GO/rGO sheets can function as building blocks and be self-assembled into 2D and 3D macroscopic materials, exhibiting unique structures and properties [66]. The strategies are actively explored for the preparation of this kind of 2D and 3D graphene based materials.

1.3.1 Methods to prepare 2D graphene materials

Langmuir-Blodgett method for monolayer graphene film. Langmuir-Blodgett technique can achieve the deposition of nanoparticles and macromolecules on substrates as large-area and monolayer thin films with precisely controlled thickness [67, 68]. This approach was also applied to prepare transparent graphene thin films that are suitable for optoelectrical applications. Unlike the traditional transparent electrodes of ITO and FTO, graphene films can be prepared in large scale with low-cost, and also are suitable in the application of flexible electronic devices. The negatively charged GO sheets can form a stable monolayer film at the interfaces of air and water/methanol because of the electrostatic repulsion preventing the overlapping of these sheets. After the deposition, it is simple to transfer the GO monolayer to flat substrates. We can get different densities of GO sheets from

dilute, close-packed, to wrinkled structures in the deposited films by varying the deposition conditions [69-71].

Improved stability of rGO in organic solvents was achieved by chemical modification. Transparent and conducting film was then prepared through Langmuir-Blodgett technique from the mixture of water and DCE (1,2-dichloroethane) containing the modified rGO [72]. It is also possible to prepare hybrid films composed by GO and SWNTs with precisely controlled composition by this technique, without additional chemical modification, since GO can act as the surfactant to disperse SWNTs [73]. The hybrid thin films exhibit improved optoelectrical properties compared with pristine GO or CNTs thin films prepared by the same method [74].

Layer-by-layer assembly method for multi-layered graphene composite film. Layer-by-layer (LbL) technique has been widely adopted for the fabrication of multi-layered film materials with tunable composition and architectures. The driving forces involved in the layer-by-layer assembly generally include the electrostatic interactions, hydrogen bonding, and covalent bonding. Based on the electrostatic interactions between different charged species, multi-layered films of CNTs and rGO have been fabricated by the layer-by-layer assembly technique from rGO with negatively charged surfaces and amine-functionalized CNTs with positively charged surfaces [75]. Positively charged rGO sheets were prepared by chemical modification with a polymer of poly(ethyleneimine) (PEI). Hybrid films were also fabricated from the PEI functionalized rGO and acid treated CNTs with negatively charged surface, based on the electrostatic interactions [76]. CNTs incorporated into the hybrid films functioning as spacers can avoid the aggregation of rGO sheets

caused by the strong π-π interactions between their basal planes. Multilayer films of rGO/poly(vinyl alcohol) (PVA) were also successfully prepared based on the hydrogen bonding interactions between the two components [77]. Based on the electrostatic interaction, this layer-by-layer technique also extends to prepare multi-layered films composed by negatively charged rGO sheets and inorganic nanoparticles by introducing a positively charged polymer of poly(diallydimethylammonium) (PDDA) between rGO and the MnO_2 nanoparticles [78].

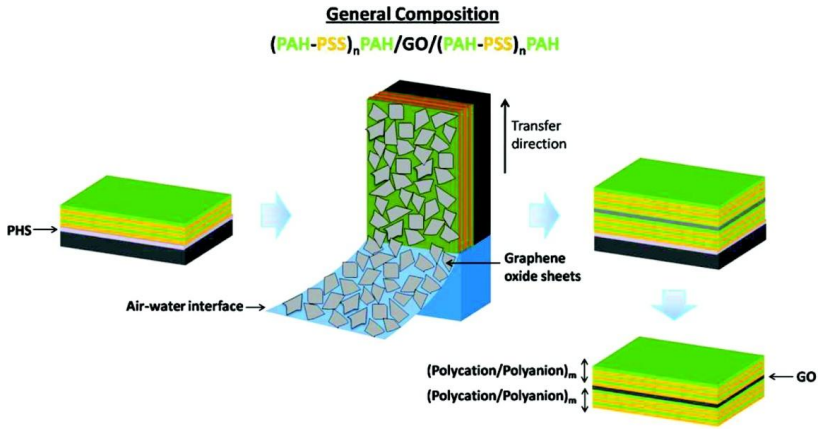

Figure 1.3 The fabrication process for multi-layered polymer films with an incorporated GO layer [79].

Layer-by-layer technique can also be coupled with Langmuir-Blodgett to prepare multi-layered films with novel structures. A polymer bi-layers film was first obtained by spin-coating of positively charged polymer of poly(allylamine hydrochloride) (PAH) and negatively charged polymer of poly(sodium 4-styrene sulfonate) (PSS), and this film was terminated with positively charged PAH. GO wan then deposited on the multi-layered PAH/PSS film by Langmuir-Blodgett technique. After furthering coating GO layer with PAH and PSS, multi-layered polyelectrolytes incorporated with a GO layer were finally

obtained. The incorporation of the GO layer improved the mechanical performance of the polyelectrolytes multi-layer (**Figure 1.3**) [79].

Vacuum filtration method for free-standing graphene paper. Paper-like films can also be obtained through vacuum filtration of nanoscale inorganic materials with platelet morphology including vermiculite and mica [80]. Free-standing graphene paper was first prepared by filtrating the aqueous dispersion of GO through a porous membrane filter [81]. The volume or concentration of GO dispersion determines the thickness of the paper. In addition, this kind of paper is usually characterized by multi-layered structures, because the graphene sheets are spontaneously arranged in a sheet-by-sheet manner at the liquid-solid interface [82]. After annealing at 220 ℃, the Young's modulus and tensile strength of the paper increased from ~20 GPa and ~150 MPa to 41.8 GPa and 293.3 MPa, respectively. The mechanical performance outperforms other inorganic paper-like materials such as graphite foils. The conductivity of the graphene paper treated at temperature of 500 ℃ can be as high as 351 S/m [83]. Due to the colloidal nature of GO and rGO sheets, they can be well-mixed with some polymers and inorganic materials. Therefore, it is possible to prepare graphene-based composite by filtration of their mixtures. In order to improve the biocompatibility, Tween was introduced into the graphene paper, and this paper exhibits no cytotoxicology to mammalian cell lines, and opens the way for potential medical applications [84].

Aiming to improve the electrochemical performances, a conducting polymer, polyaniline (PANI), was also incorporated into the graphene paper through this technique. However, due to the different surface charges between PANI nanofibers and rGO sheets, the pH value of their mixture should be

carefully adjusted to around 9 in order to obtain a stable mixture of these two components. In the as-prepared PANI-rGO paper, the PANI nanofibers are uniformly sandwiched between the rGO sheets, leading to the increased interlayer distance between the rGO sheets [85]. Due to the presence of surface functionalities, a wide range of metal oxide nanoparticles were attached onto the rGO sheets, including SnO_2, NiO, MnO_2, and SiO_2. Composite paper with multi-layered structures was then readily prepared by filtration of modified rGO sheets [86]. This sandwiched structure is also beneficial to buffer the volume change when used in energy storage devices [87].

Solvent evaporation method for free-standing graphene paper. In the solvent evaporation method, GO can be self-assembled at the air-water interface by heating its dispersion at about 80 ℃ for about 40 min, and after remove the extra solution, a free-standing paper-like material can also be readily obtained. The surface area of air-liquid interface and the self-assembly time determines the size and thickness of the paper [88]. The heating induced self-assembly was also successfully extended to directly prepare hydrazine reduced GO membrane at the air-water interface with moderate stirring (400 rpm) at the same temperature for 12 h [89]. This method was also applied to prepare hybrid films composed by GO and CNTs. The relative percentage of each component in the solution is identical to them in the hybrid film [90].

We found that after the water completely removed, GO membrane was deposited at the bottom of a polytetrafluoethylene (PTFE) mode with low surface energy, and can be easily peeled off from the substrate to form a free-standing paper [91]. Another study found that rGO paper can be prepared and peeled off after heating the mixture of GO with a reducing agent of hydrogen

iodine (HI) at 90 ℃ for 2 h on flat PTFE substrate. The residual iodine can be removed by washing with ethanol and water [92]. However, the mechanical properties of graphene paper prepared by solvent-evaporation method are usually inferior compared with the paper prepared by vacuum filtration method.

Electrochemical deposition method for graphene thin films. Electrophoretic deposition (EPD) is a technique to deposit thin films through the movement of charged colloidal particles under electrical fields towards the electrode with opposite charges [93]. It is crucial to prepare stable colloidal dispersions for the electrophoretic deposition. Compared with other film preparation methods, electrophoretic deposition can precisely control the film thickness with excellent uniformity at high deposition rates. In addition, this method is easy to scale up, and suitable to a wide range of inorganic, polymer, and composite colloidal particles [94]. The charged surfaces of GO and rGO enables the electrophoretic deposition of their films. By applying a positive potential of 10 V, the negatively charged GO sheets can form uniform films in 10 min, and that the oxygen functionalities were successfully eliminated in the anodic electrophoretic deposition process possibly because of the presence of a series reactions including oxidation of carboxylate, oxidative decarboxylation, and dimerization of radicals (**Figure 1.4**). Consequently, the electrophoretic deposited GO paper exhibits a two fold increase of electrical conductivity compared with GO paper prepared by filtration method [95].

Porous graphene film was prepared from this technique by using aluminon as a charging and dispersing additive. The application of dispersing agents can also avoid the introduction of charged defects into the pristine carbon nanomaterials [96]. The electrophoretic deposition method is also applicable to

three-dimensional substrates. GO was reduced by p-phenylene diamine to introduce positively charged surfaces of $-N^+$, and then deposited on porous nickel foam by this method [97]. Transparent film of MoS_2-rGO was recently prepared by electrophoretic deposition of MoS_2 modified graphene sheets. The dispersion of MoS_2-rGO in a mixed solvent of acetone and ethanol was found to be stable as long as one week because of the presence of residual oxygen functionalities on rGO [98]. By changing the composition ratios of rGO and CNTs in solution, hybrid films with different contents of rGO and CNTs were readily obtained from this method [99]. This method was also extended to prepare multi-layered films of rGO and quantum dots by repeated electrophoretic deposition of rGO and the quantum dots on flat substrates, and the number of the layers was controlled by the times of electrophoretic deposition [100].

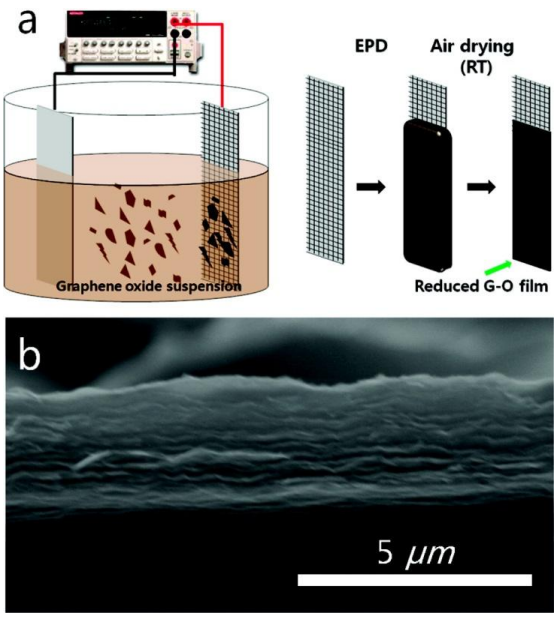

Figure 1.4 The electrophoretic deposition process for the preparation of rGO film from GO solutions, and the SEM picture of rGO film at a cross-section view [95].

The simultaneous electrodeposition and electrochemical reduction of GO on a conducting substrate was also reported [101]. This deposition process usually employs a negative potential around -1.0 or -1.2 V, or a repeated cyclic voltammetry (CV) with the lower potential of about -1.2 V. This one-step method can be achieved in a solution with pH values from 1.5 to 12.5, simplify the electrode fabrication process, and allows one to control the film thickness by varying the deposition time or the cyclic voltammetry numbers. The conductivity of GO dispersion which can be adjusted by adding electrolyte is an important factor affecting the deposition process, and the deposition can be achieved only with the conductivity of solution from 4 to 25 mS/cm. No detectable deposition occurred when the conductivity of the solution is too low. Nevertheless, if the conductivity is higher than 25 mS/cm, GO solution will become unstable [102].

Because both of the electrochemical reduction of GO and metal ions take place at cathodic conditions, composite film composed by rGO and metal nanoparticles was successfully prepared by a cyclic voltammetry method from the mixtures of GO and metal ion salts. The composite film exhibits sandwiched structure with metal nanoparticles intercalated between the rGO sheets with improved electrical conductivity than the pristine rGO film [103]. By changing the higher and lower potentials in CV scans, the simultaneous electrochemical reduction of GO and electropolymerization of monomers was also reported. These two reactions occur independently, and lead to the formation of hybrid film of rGO and conducting polymers (polyaniline or polypyrrole) with layer-by-layer structures. The top layer can be adjusted as

conducting polymers or rGO by simply varying the directions of CV scans [104].

1.3.2 Methods to prepare 3D graphene materials

Hydrothermal reduction for graphene hydrogel. 3D macroscopic materials, i.e., graphene hydrogel, can be prepared by hydrothermal treatments of GO dispersions with concentration not lower than 2 mg/mL at 180 ℃ [105]. Although containing about 97.4% of water, the as-prepared graphene hydrogel possesses a high electrical conductivity (5×10^{-3} S/cm), and is mechanically stable with a modulus as high as 450-490 kPa. Before the hydrothermal reduction, owing to the presence of carboxyl, carbonyl and epoxy groups, the GO sheets are hydrophilic and well dispersed in water. With increasing the reduction time, the oxygen functionalities on GO sheets were eliminated gradually, and the conjugated structures were restored. The hydrophobic and π-π interactions from the conjugated structure on rGO sheets lead to the random self-assembly of the flexible sheets in three dimensional and the formation of macroscopic hydrogel with a wide range of pore size distribution from sub-micrometer to a few micrometers. If the concentration of GO is lower than 2 mg/mL, the partial overlapping and cross-linking is more difficult to take place between the rGO sheets well dispersed in water, eventually with the formation of their dispersions or aggregated powders [49].

Chemical reduction for graphene hydrogel. The high temperature and long reaction time of the hydrothermal method limits the large scale production of graphene hydrogel. With the aid of certain reducing agents, the self-assembly of rGO sheets can take place along with their chemical reduction under mild condition (~ 95 ℃) in a shorter reaction time (within 3 h) [106]. The reducing

agents used to prepare graphene hydrogel include ascorbic acid, hydroiodic acid, sulfur-containing chemicals, and hydroquinone. The elimination of any physical disturbance during the reaction is a crucial factor for the formation of graphene hydrogel [107]. Graphene hydrogel can be further functionalized by introducing other components. The presence of GO can help the dissolution of CNTs, and CNTs can be attached to GO sheets without serious aggregation [108]. After heating the mixture of GO and CNTs containing a reducing agent of ascorbic acid, hybrid hydrogel of rGO/CNTs was obtained with 3D interconnected walls composed by both of rGO sheets and CNTs [109].

When noble metal ions ($PtCl_6^{2-}$) were added into GO solutions containing ascorbic acid, the hybrid hydrogel of rGO-Pt nanoparticles was prepared from a one-pot synthesis after heating the mixture for several hours without stirring [110]. Taking advantage of the simultaneous reduction of GO by Fe(II) and deposition of metal oxide nanoparticles, 3D graphene hydrogel modified with ion nanoparticles was successfully prepared through a one-step approach (**Figure 1.5**). By simply adjusting the pH of the solutions, the composition and morphology of iron oxide nanoparticles can be readily controlled [111].

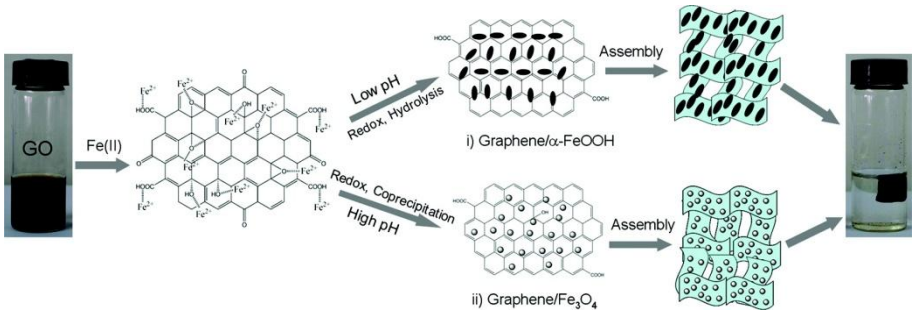

Figure 1.5 A one-step procedure for the preparation of iron oxide nanoparticle modified graphene hydrogel [111].

Template-directed method for 3D graphene materials. Compared with hydrothermal or chemical reduction methods, template-directed methods provide approaches to synthesis of 3D graphene materials with well-controlled and tunable pore size distributions by varying the diameter of the templates. Polystyrene (PS) and silica colloidal particles are commonly employed as sacrificial templates for the preparation of hollow porous materials, and these two colloids have also be extended to prepare 3D graphene materials with different pore size distribution. By carefully adjusting the pH values of the two solutions to 2.0, both PS colloids and rGO are positively charged and can form a homogenous mixture. Then the mixture was exposed to filtration through an anodizc membrane with pore size of 200 nm. During the filtration, the pH of the solution was adjusted to 6, which can make the two components with oppositely charged surfaces and stimulate the electrostatic interactions between them. The change of pH to 6 was critical to incorporate PS particles uniformly distributed in the PS-rGO foam. Porous rGO foam with uniform pore structures was finally obtained after removal PS particles by toluene. Porous rGO foam with uniform pore structures was finally obtained after removal PS particles by toluene [112]. Capillary modeling represents a more general approach to push GO sheets wrapped on template particles by capillary force, without the need of specific interactions. Capillary modeling and template removal was achieved in one step in a device for aerosol spray pyrolysis, leading to the formation of hollow rGO capsules with uniform size distribution [113].

However, the pore size of the PS template porous rGO film is limited to the range of micrometer due to the relatively larger size of PS particles (20 μm). Taking advantages of the amphiphilic nature of GO [73], the hydrophobic

interaction was used to prepare nanoporous graphene foam by using methyl functionalized silica as the templates, by mixing GO with the modified silica particles to obtain GO wrapped silica particles (**Figure 1.6**). The reduction of GO was obtained by annealing the composite at high temperature in inert atmosphere, and the silica was removed by HF etching. The pore size of rGO foam can be tuned from 30 to 120 nm by changing the size of silica nanoparticles [114].

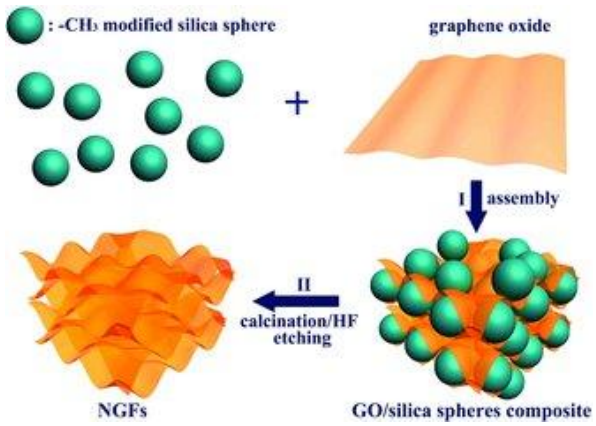

Figure 1.6 The process for the preparation for the nanoporous graphene foam with silica nanoparticles as the templates [114].

Chemical vapor deposition for 3D graphene materials. The chemical vapor deposition (CVD) method can produce graphene materials with higher electrical conductivity and fewer defects than rGO materials prepared from wet-chemical approaches. In order to synthesis of 3D graphene materials by CVD method, porous nickel foam with 3D interconnected branches was first employed as the substrate and template. Methane was used as the carbon precursor, decomposed at 1000 ℃ under atomic pressure, and then deposited on nickel foam. The prepared graphene foam is a monolithic material with 3D interconnected graphene sheets and density as low as 5 mg/cm^3, comparable to

the lightest aerogel (2-3 mg/cm^3). Wrinkles were also observed on the graphene sheets possibly due to the different thermal expansion coefficients between nickel and graphene [115].

Afterwards, a safe and cheap carbon precursor of ethanol was employed to prepare graphene foam by CVD method. The prepared graphene foam exhibits almost the same morphology compared with that from the methane CVD method [116]. A two-step CVD approach was applied to prepare 3D graphene-CNTs foam. 3D graphene foam was first prepared on nickel foam by using ethanol as the carbon precursor. The catalyst for CNTs growth was then deposited on the graphene foam by immersing into a solution containing nickel salts. CNTs were the grown on the graphene foam also using ethanol as the precursor, and finally the nickel foam was removed by HCl solution [117]. The monolithic graphene foam can be further modified with metal oxide or polymers by different approaches, including hydrothermal synthesis [118], wet-chemical reaction [119], and electrochemical deposition [120].

1.4 Application of self-assembled graphene

The self-assembled macroscopic graphene materials exhibit unique structures and properties. They can be further functionalized with a wide range of metal nanoparticles, polymers, and biomolecules, and then used as electrodes for electrochemical biosensors, fuel cells, supercapacitors, and lithium ion batteries.

1.4.1 Self-assembled graphene materials for electrochemical biosensors

Graphene paper as flexible substrate for electrochemical biosensors. Besides the highly conductive nature, self-assembled graphene paper also

processes excellent flexibility. The design of flexible biosensor can meet the increasing demand for portable devices for medical applications. There are two types of electrochemical biosensors, i.e., enzymatic biosensors based on the use of enzyme and nonenzymatic biosensors based on the use of metal or metal oxide catalysts. A hybrid film was prepared by filtration of Nafion functionalized rGO sheets, and then modified by organophosphorous hydrolase (OPH). The remarkable electrical conductivity of rGO sheets and the low interfacial resistance of Nafion endow the OPH modified hybrid film exhibiting excellent electrochemical performance for the detection of organophosphate with a sensitivity of 10.7 nA/μM and detection limit of 0.137 μM. After 100 binding cycles, the sensitivity of the flexible biosensor is still as high as 9.7 10.7 nA/μM [121].

In order to achieve the real-time detection of biomolecules released from living cells, RGD-peptide modified graphene paper was prepared by covalent binding of the peptide to a free-standing graphene paper prepared by filtration of pyrenebutyric acid modified rGO sheets. The RGD-peptide can facilitate the attachment of growth of cells on the free-standing graphene paper. This flexible electrode can be employed for the real-time monitoring of nitric oxide (NO) released from endothelial cells attached to the RGD modified graphene paper. The graphene paper biosensor possesses good flexibility and can keep its original performance after 45 times of bending and relaxing cycles [122].

A nonenzymatic biosensor was also developed by transferring 2D assembled gold nanoparticles at oil-water interface to free-standing graphene paper through dip-coating method (**Figure 1.7**). The closely packed gold nanoparticles on the graphene paper exhibits excellent electrochemical

performance for the electro-oxidation of glucose. The biocompatibility also allows monitoring hydrogen peroxide at low concentration in living cells [91]. A flexible electrode composed by triple components of platinum nanoparticles, Graphene paper modified with MnO_2 nanowires was fabricated, and applied for the detection of H_2O_2 from living cell. The growth of MnO_2 nanowires on graphene paper can increase the surface areas of the 2D assembled substrate and provide more growing sites for the platinum nanoparticles. The variation of amperometric response is less than 5% after 100 repeated bending [123].

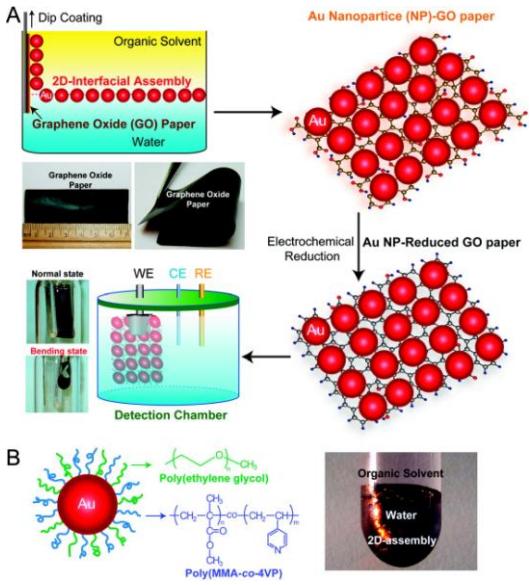

Figure 1.7 Fabrication process for the free-standing electrodes by dip-coating self-assembled gold nanoparticles onto a graphene paper [91].

3D graphene for electrochemical biosensors. Compared with the 2D graphene paper, the 3D graphene foam-like materials can provide increased surface areas for loading enzymes and metal or metal oxide catalysts. Prussian blue (PB) modified graphene hydrogel with controllable ratio between the two components was prepared by adding $FeCl_3$ solution containing a reducing agent of ascorbic acid into the mixture of GO and ferricyanide. The detection limit for

hydrogen peroxide is as low as 5 nM [124]. By a hydrothermal method, Co_3O_4 nanowires were uniformly deposited onto 3D graphene foam prepared by a CVD method. When used as free-standing electrode, the detection limit of Co_3O_4 nanowires modified graphene foam is 25 nM [118]. Graphene-nickel core-shell electrode was prepared by annealing lithographically defined 3D porous carbon coated nickel at 750 ℃ for 20 min with the flow of forming gas containing 5% H_2 and 95% N_2. The electrode exhibits a good linear range to glucose concentration (1 to 10 mM) [125]. A variety of noble metal nanoparticles, including Pt, Au and Pd were electrodeposited on the 3D graphene foam prepared by lithographic method, and hydrogen peroxide can be reduced at 0.1 V while the reduction peak was observed at -0.1 V on these kinds of electrodes [126].

1.4.2 Self-assembled graphene materials for electrochemical energy conversion

Graphene paper for electrochemical energy conversion. A one-step electrochemical method was used to prepare Pt nanoparticles modified graphene film supported on a conducting substrate. This strategy is based that both GO and noble metal ions can be reduced rGO and metal nanoparticles at the negative potentials. The prepared electrode materials exhibit a three folds increase of peak current toward methanol oxidation, and the peak current is as high as 195 mA per mg Pt for graphene film based electrode. The onset potential was also decreased from 0.60 V for Vulcan supported Pt nanoparticles to 0.35 V for the rGO film supported catalyst. The peak ratio of the forward scan to the backward scan increased to 1.26 for the rGO film based catalyst compared with value of 1.01 for Vulcan based catalyst [26]. PtAu alloy

nanoparticles were deposited on rGO film. The alloy nanoparticles with a mass ratio of 2 : 1 possesses the highest activity for both of the reactions. The long-term stability for methanol oxidation is also improved by the support materials of rGO because of its ability to effectively remove the poison species formed on nanoparticles during the oxidation process of methanol [127].

Graphene paper based materials can also be used in proton exchange membrane, a crucial components in the assembly of direct liquid fuel cells. The development of high temperature fuel cells (above 100 ℃) can significantly increase the performance by increasing the electrode reaction kinetics, improving the electro-activity toward CO tolerance, and facilitating the thermal and water management. The evaporation of water from Nafion membrane limits its operation temperature below 80 ℃ at low humidity environment. A composite membrane of GO-Nafion was prepared by casting 3-mercaptopropyl trimethoxysilane (MPTMS) functionalized GO mixed with Nafion solution in ethanol. Compared with the pristine Nafion membrane, the hybrid membrane exhibits almost 3 times increase of proton conductivity at high temperature of 120 ℃ with a humidity of 25% [128]. Sulfonated polyimide (SPI) was mixed with GO solution in dimethyl sulfoxide (DMSO) and then casted into glass molds to prepare SPI-GO proton exchange membrane. The hybrid membrane with 0.5wt% of GO exhibits nearly 2 folds increase of proton conductivity compared with Nafion at 90 ℃. Furthermore, GO in the hybrid membrane can prevent methanol molecules crossing over the membrane, and improve the mechanical properties of the membrane [129]. Sulfonic acid functionalized GO sheets were used to prepare paper-like materials and directly used as proton exchange membrane in liquid fuel cells. Although this membrane exhibits

satisfied proton conductivity and mechanical stability, the problems of fuel crossover and long-term stability need to be addressed before its practical applications [130].

3D graphene materials for electrochemical energy conversion. The 3D graphene materials modified with noble metal nanoparticles, transition metal oxide nanoparticles, or nitrogen doping have been investigated as electrocatalysts for oxygen reduction reactions and liquid fuel oxidation reactions. 3D nitrogen-doped graphene aerogel modified with Fe_3O_4 nanoparticles was produced from a two-step method: hydrothermal treatment of a solution with GO, iron acetate, and polypyrrole (PPY) at 180 ℃; and then thermal annealing at 600 ℃ in nitrogen atmosphere (**Figure 1.8**). In the hydrothermal process, three reactions occurred simultaneously: the reduction and self-assembly of rGO sheets into 3D structures, the incorporation of nitrogen atoms by PPY, and the nucleation and growth of Fe_3O_4 nanoparticles on the graphene sheets. Compared with nitrogen-doped graphene sheets and nitrogen-doped carbon black both modified with Fe_3O_4 nanoparticles, the nitrogen-doped graphene aerogel modified with Fe_3O_4 nanoparticles exhibits an improved catalytic activity towards oxygen reduction reactions of the 3D material [131].

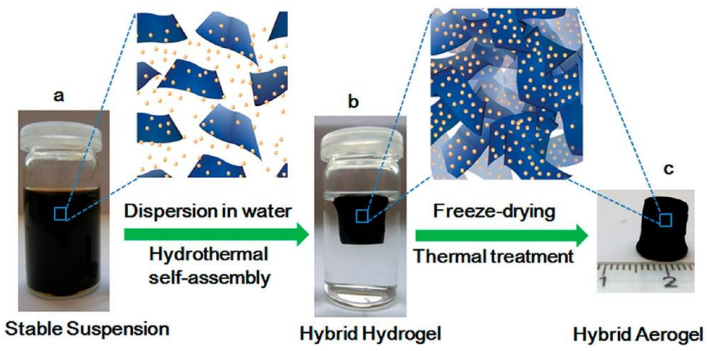

Figure 1.8 Preparation process of the 3D nitrogen doped graphene hydrogel loaded with metal oxide nanoparticles [131].

Cobalt-nitrogen doped graphene aerogel was also prepared through a supermolecular interaction promoted gelation process followed by thermal treatment. After shaken the mixture of GO, melamine, and cobalt nitrate vigorously for a few seconds, graphene hydrogel was formed. In this process, besides providing nitrogen source for doping, melamine also acts as cross-linker molecules to promote the gelation process. Finally, the catalyst was obtained by thermal treatment at 600 ℃. Compared with cobalt-nitrogen modified graphene sheets, the 3D catalyst also exhibits a more positive onset potential and higher cathodic current density for oxygen reduction reaction, with performance close to the commercial Pt catalyst based on 20% Pt on carbon black [132].

The 3D graphene materials modified with noble metal nanoparticles were also employed as electrocatalyst for liquid fuel oxidation reactions. Through a ferritin-templated method, Pt nanoparticles with the diameter of about 3 nm were deposited on 3D graphene materials prepared from CVD method. The size and self-assembly of Pt nanoparticles on graphene sheets was readily controlled the nanocage structure of ferritin. The prepared Pt-3D graphene materials possess nearly 30% increase of electrochemically active surface areas compared with Pt-rGO and Pt-carbon black. The anodic current density of methanol oxidation is also higher on Pt-3D graphene than the other control samples [133]. Ternary alloy nanoboxes of Pt/PdCu functionalized 3D graphene materials were prepared via a two-step solvethermal method, and used as catalysts for ethanol oxidation reactions. PdCu nanocubes modified 3D graphene materials were first

prepared by treating the mixtures of GO, $PdCl_2$, $CuSO_4$ $5H_2O$, and glutamate in ethylene glycol with pH adjusted to about 13 at 160 ℃. The prepared material was further placed in an ethylene glycol solution containing H_2PtCl_6 $6H_2O$ and glutamate, and heated at the same temperature for another 3 h to get the ternary alloy nanocubes modified 3D graphene materials. Compared with Pt and PdCu electrocatalysts, the ternary alloy nanocubes functionalized 3D graphene materials exhibit significantly improved activity towards ethanol oxidation in alkaline media. In addition, a four-fold increase of oxidation current density is also obtained compared with the commercial available electrocatalyst of Pt-carbon black [134].

1.4.3 Self-assembled graphene for electrochemical energy storage

Graphene paper for electrochemical energy storage. Graphene paper can be used as free-standing electrodes for electrochemical energy storage. However due to the decrease of specific surface areas caused by restacking of graphene and absence of active functionalities, the performance of pristine graphene paper is inferior. Different strategies have been applied to introduce active materials into the graphene paper including various transition metal oxides or conducting polymers expecting to improve the performance. Polyaniline (PANI) was directly grown on graphene paper by an electrochemical polymerization method. The prepared paper exhibits favorable flexibility, mechanical strength, and electrochemical performance. The obtained maximum capacitance of the sample can reach 233 F/g, exhibiting nearly 60% improvement of performance compared with pristine graphene paper (147 F/g) [135]. A composite paper of graphene-PANI nanofiber with sandwiched structure was prepared by vacuum filtration method with the PANI nanofibers

incorporated into the layer structures of graphene sheets. The composite paper with 44% graphene exhibits 10 times conductivity of PANI film, and improved capacitance (210 F/g at 0.3 A/g). Moreover, the composite paper can retain a good performance (197 F/g) at higher current density (3.0 A/g) [85]. Co_3O_4 microspheres were grown on a hybrid paper rGO-CNT through a hydrothermal method. The Co_3O_4 microspheres were densely packed on the hybrid paper to form a monolayer. At the same time, GO is also reduced in the hydrothermal process under alkaline conditions. The capacitance of the composite paper was 378 F/g at 2 A/g. It can keep 78% of the specific capacitance while the current rising to 8 A/g [136].

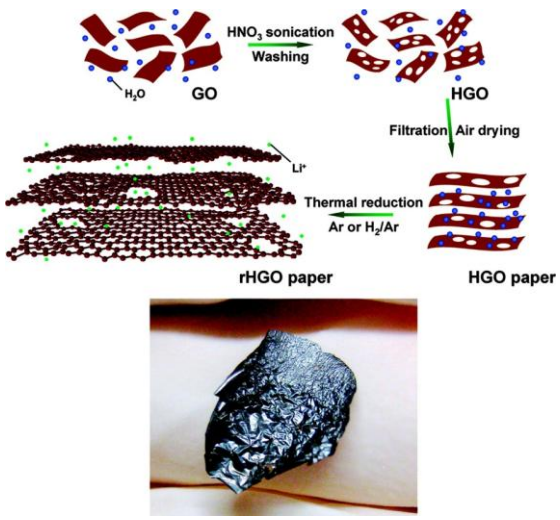

Figure 1.9 Preparation of holey graphene paper from graphene oxide, and a picture of the sample [137].

The application of graphene paper for lithium ion batteries has also been actively explored. In order to increase the accessible volume of graphene paper, defects was first introduced into GO sheets by sonication of GO dispersions in concentrated HNO_3. Holey defects with a wide range of size distributions were generated on the GO sheets. Graphene paper was prepared by filtration of the

GO solutions and thermal annealing of the obtained GO paper in argon/hydrogen atmospheres (**Figure 1.9**). The holey graphene paper possesses unconspicuous loss of electrical conductivity although a lot of pores were introduced into the rGO sheets. The holey graphene paper prepared under different conditions exhibits increased discharging capacity (399-459 mAh/g) compared with pristine graphene paper (313-336 mAh/g) at C/7.4 [137].

A thin film of V_2O_5 nanoparticles was grown on the graphene paper by pulsed laser deposition method to prepare the free-standing anode electrode for lithium ion batteries. The prepared graphene paper electrode exhibits comparable performance with graphene power. The stabilized capacity of the material is about 300 mAh/g at C/2. The capacity of graphene paper kept to more than 200 mAh/g at 1C, and nearly no decrease of the performance was observed after 185 cycles. However, the performance of graphene powder decreased to about 50% of its initial value after 135 cycles [138]. Anionic surfactants were used to get a stable dispersion of graphene materials prepared from thermal expansion of graphite oxide. The surfactants adsorbed on the surface of graphene can also bind metal ions to form an ordered structure. After the crystallization of metal oxide nanoparticles between the graphene sheets, composite materials with sandwiched structures were prepared. The specific capacity of SnO_2-graphene paper electrode is about 625 mAh/g at 0.01 A/g. The sandwiched structure can also buffer the volume change of metal oxide nanoparticles during charge/discharge process, and nearly on fading of capacity of the materials was observed after 100 charge/discharge cycles [86]. Vacuum filtration was employed to prepare a composite paper composed by V_2O_5 nanowire and graphene. V_2O_5 nanowires were incorporated into the graphene

sheets to form a multi-layered structure. The specific capacity of the composite paper with 50% V_2O_5 nanowires is 293.7 mAh/g at 0.1 A/g. After 200 cycles, the specific capacity still can hold to 230.5 mAh/g. The composite paper with 15% V_2O_5 nanowires exhibits superior capacity retention even after 100 0000 cycles at 10 A/g [139].

3D graphene materials for electrochemical energy storage. Propylene carbonate is widely used as organic solvent in supercapacitors. A solvothermal reduction method was applied to prepare graphene hydrogel by heating the dispersion of GO in the solvent of propylene carbonate at 180 ℃. The electrical conductivity of the prepared sample is about 2 S/m, which is about 4 times of graphene hydrogel prepared from hydrothermal reduction method (0.5 S/m). The cell voltage of the supercapacitor can be enlarged to 3 V in propylene carbonate. The specific capacitance can reach 140 F/g at 1 A/g. Because of the improved electrical conductivity, the supercapacitor also processes a characteristic of high rate capability. The capacitance of the supercapacitor is 90 F/g at 30 A/g. [140].

Hydrothermal method was also employed to prepare graphene hydrogel doped with nitrogen and boron by heating the mixture of GO and ammonia boron trifluoride (NH_3BF_3) at 180 ℃. The capacitance of the co-doped sample is 239 F/g at 1 mV/s, higher than specific capacitances of nitrogen doped, boron doped, and un-doped graphene hydrogel (190, 228, and 181 F/g) [141]. 3D graphene-polypyrrole foam was prepared from a one-step method by heating a solution containing GO and 5 vol% pyrrole at 180 ℃ for several hours. The prepared graphene foam exhibits 5 times volume compared with the graphene hydrogel without the functionalization of polypyrrole. The functionalized

graphene hydrogel was composed by thinner interconnected walls than the pristine graphene hydrogel. The capacitance of the polypyrrole-graphene hydrogel was 350 F/g at 1.5 A/g. Importantly, the electrochemical performance of polypyrrole-graphene hydrogel remains almost constant even at highly compressed state [142].

A flexible and light-weight lithium ion battery was fabricated using CVD grown graphene foam as the current collector. Lithium titanium oxide (LTO) and lithium ion phosphates (LFP) were deposited on the graphene foam through hydrothermal method, and employed as anode and cathode electrodes, respectively. The electrical conductivity of the graphene foam can reach about 1000 S/m. The remarkable electrical conductivity and porous structures enables a fast charge transportation of the electrodes. For the LTO-graphene foam electrode, the specific capacity is 170 and 160 mAh/g (at 1 C and 30 C). When the rate increased to 200 C, the electrode can retain about 80% of the specific capacity at 1 C rate. After 20 times bending, only a decrease less than 1% was observed compared with the original battery [143].

Ultrathin graphite foam with remarkable mechanical strength was prepared by precipitation of thin layers of graphite from methane at 1050 ℃. Nickel foam was easily removed without any polymer supporting layers. The slurry containing LFP, carbon black, and polyvinylidene fluoride (PVDF) was then drop-casted onto the graphite foam to prepare the electrode for lithium ion batteries. Compared with the aluminum foil based electrode, the LFP-ultrathin graphite foam exhibits an almost one-fourth increase of specific capacity with a maximum capacity of 102 mAh/g if the total weight of electrode materials were considered [144]. Another 3D hybrid material composed by TiO_2, rGO, and

CNTs was prepared through controlled hydrolysis of tetrabutyl titanate in ethanol solution containing rGO and CNTs. CNTs in the 3D materials can prevent the aggregation of graphene sheets and provide additional charge transport channels for TiO_2 nanoparticles. The hybrid material delivers a capacity of 163.7 mAh/g at 1 C, while TiO_2-rGO (155.4 mAh/g) and pristine TiO_2 (141.3 mAh/g) nanoparticles exhibit lower specific capacity [145].

A capillary driven self-assembly method was adopted to prepare crumpled graphene sheets wrapped silicon nanoparticles by passing the mixture of GO and silicon nanoparticles through a pre-heated tube furnace (**Figure 1.10**). When employed as anode, the capacity of the battery can reach 1200 mAh/g at 0.2 A/g. Importantly, 83% of the initial capacity can be retained after 250 charge/discharge cycles, and the Coulombic efficiency can reach an equilibrium value of 99% after 5 cycles and 99.5% after 10 cycles [146].

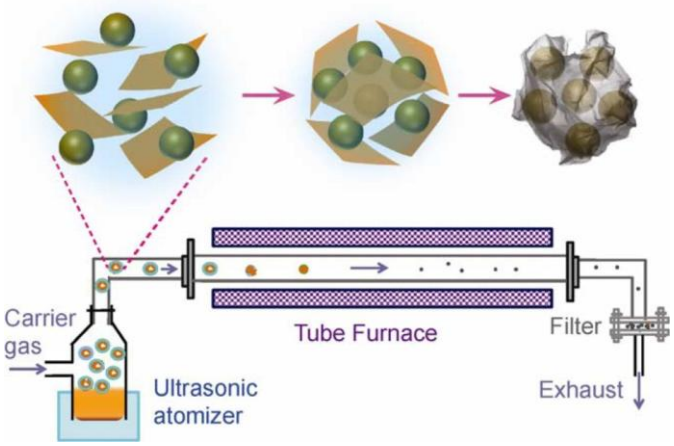

Figure 1.10 The preparation process for crumpled graphene wrapped silicon nanoparticles [146].

1.5 Objective of research projects

Although graphene materials process excellent chemical and physical properties, its practical application is hindered by large-scale production through efficient and environmentally-friendly method. Graphene can be prepared effectively by the oxidation-exfoliation-reduction approach in a large-scale. However, in the reduction process, highly toxic chemicals, including hydrazine and sodium borohydride, are widely applied to prepare rGO. Another challenge is to assemble this nanomaterial into macroscopic materials which can be easily handled for various applications.

The object of this research project is to develop eco-friendly methods for the preparation of graphene materials, and find suitable approaches to assemble them into 2D and 3D macroscopic materials with different functionalities. Their potential application of the self-assembled materials in the field of electrochemistry was also investigated in order to address the current issues of health and energy sciences.

We first achieved the simultaneous reduction of GO and deposition of PtNi alloy nanoparticles through an electrochemical approach with the aid of ultra-sonication. The alloy nanoparticles directly grown on rGO film exhibit excellent catalytic activity for glucose electro-oxidation, and can detect in real samples.

Free-standing graphene paper was then prepared through filtration of hydrothermally reduced GO, and modified with copper nanocubes by electrodeposition method. The prepared electrode was employed as flexible electrodes for direct hydrazine fuel cells. The formation of oxide layer on the

surface of copper nanocubes can lower the oxidation potential of hydrazine, and prevent further corrosion of copper.

We also prepared graphene paper functionalized with carbon nanotubes and metal oxide nanoparticles. The incorporation of these functionalities into graphene paper led to the formation of flexible electrodes with sandwiched structure and can also prevent the stacking of graphene sheets. These paper electrodes were further applied to construct a flexible asymmetric supercapacitor with the aid of a polymer gel electrolyte.

Graphene hydrogel with 3D inter-connected pores was also prepared through a one-step chemical reduction and self-assembly method by using an environmentally-benign agent of glutathione. The formation of 3D structures is also beneficial to prevent the aggregation of graphene sheets and increase overall specific surface areas. The prepared graphene hydrogel was directly cut into pieces and used as electrodes for supercapacitors.

2. Graphene film modified with PtNi nanoparticles for nonenzymatic glucose biosensor

2.1 Introduction

Graphene is an emerging type of supporting substrates for functional nanomaterials due to a host of intriguing properties, e.g., large surface areas, excellent electrical conductivity, flexibility and chemical inertness [17, 147, 148]. The integration of graphene and nanoparticles of diverse chemical composition has been actively explored for applications ranging from electrocatalysis, photocatalysis to energy harvesting and storage [149-153]. Preparation of the nanocomposites is typically a two-step procedure involving the reduction of GO as well as attachment of metal nanoparticles [154-156]. In the existing approaches, a layer of organic linker molecules is commonly used to anchor metal nanoparticles on graphene substrates [157]. Although metal nanoparticles can be loaded on graphene in relatively high density in these processes, the use of the organic molecules to link the two components can slow down the direct electron transfer to some extent and possibly block the available active sites on metal nanoparticles and graphene, leading to reduced catalytic activities. Moreover, the possible contamination of chemically reduced GO (CRGO) by the excessive reagents used in GO reduction is also an underlying factor to affect the electrocatalytic performance of the nanocomposites. Therefore, a straightforward green approach toward the nanocomposites free of chemical reducing agents and organic linkers is highly desirable and practically useful for efficient electrocatalysis. For example, metal or metal oxide nanoparticles can be directly decorated on rGO sheets through

self-propagating domino-like reactions when the GO films containing different metal salt precursors were exposed to local hot spot [59].

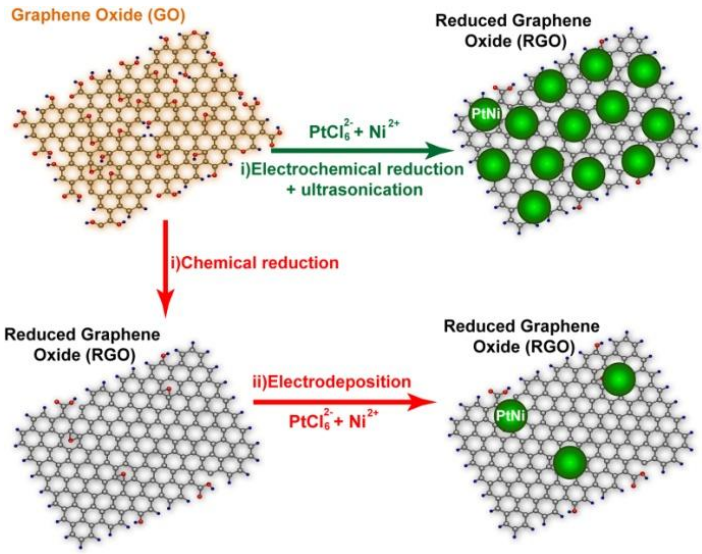

Figure 2.1 One-step and two-step methods for the preparation of PtNi-RGO [158].

In this chapter, we report a one-step ultrasonication-assisted electrochemical approach for the preparation of nanocomposites of graphene and PtM (M= Ni and Co) alloy nanoparticles and their uses for highly selective nonenzymatic glucose detection [158]. As illustrated in **Figure 2.1**, our results have shown that at a highly negative potential, the simultaneous electrochemical reduction of GO and electrodeposition of alloy nanoparticles led to nanocomposites with dense loading of nanoparticles evenly distributed on the electrochemically reduced GO (ERGO) support. Electrodeposition is kinetic-controlled process involving preferential nucleation and subsequent growth of nanoparticles on an appropriate electrode surface. The formation of nuclei of nanostructures strongly depends on the interaction between the electrodeposited metal with the substrate (of which the electrode is built). GO

process abundant surface functional groups (-OH, C-O-C and -COOH) providing nucleation sites for noble metal nanoparticles [155, 156]. One major finding is that ultrasonication during the electrodeposition can prevent agglomeration of deposited metal nanoparticles and is critical for the formation of well-dispersed nanoparticles. The ultrasonic irradiation can lead to both chemical and physical effects, including enhancement of mass transportation, surface cleaning and formation of radicals, and thereby significantly minimizes the aggregation and reduces the diameter of the nanoparticles. Ultrasonic-electrodeposition is classified into indirect ultrasonication and direct ultrasonication [159]. In indirect ultrasonic-electrodeposition, the electrolyte solution containing nanoparticles is irradiated by ultrasonic waves before the deposition process to ensure a good dispersion. In direct ultrasonic-electrodeposition, the electrolyte is under continuous ultrasonic irradiation during the electrodeposition. In this work, we use direct ultrasonic-electrodeposition, by which the binding with the active sites and the dispersion of nanoparticles by ultrasonication occur at the same time. In contrast, nanocomposites of PtNi nanoparticles and CRGO fabricated in two steps (chemical reduction of GO followed by the electrodeposition of metal nanoparticles) have shown sparsely loaded nanoparticles (**Figure 2.1**) due to the lack of functional binding sites in CRGO. Very recently, one-step reduction of both metal ions precursor and GO has been used to prepare metal nanoparticle-CRGO composites, for example, the self-propagating domino-like reactions [59]. However, most of the methods were limited to the simultaneous chemical reduction by using reducing agent [160], sonolysis [161], and microwave irradiation [157, 162]. The one-step electrochemical reduction under

ultrasonication in our strategy eliminates the potential contamination in chemical reduction [50, 51, 163] and the use of the organic linkers, representing a rapid, efficient, and green approach to fabricate highly active electrocatalysts.

Our choice of glucose as the analyte of interests is motivated by the practical medical needs for diagnosis of human diseases such as diabetes and hyperglycemia [164]. Enzymatic biosensors based on enzymes such as glucose dehydrogenase or glucose oxidase are attractive platforms because of their high sensitivity and excellent selectivity [95, 165-167]; however, the insufficient long-term stability is the main disadvantage of enzymatic glucose sensors arising from their intrinsic dependence on enzyme activity [168, 169]. To address this limitation, major research efforts have been devoted to developing nonenzymatic biosensors, such as Pt-based amperometric glucose sensors. Although early research has demonstrated that bulky Pt electrodes suffer from sluggish kinetics to produce significant faradaic currents and severe interferences from electroactive species in body fluids [170], recent development have shown that the use of nanostructured Pt electrocatalysts could lead to greatly improved performance in glucose oxidation because of their higher active surface area [171-175]. Meanwhile, increasing evidence have confirmed that Pt-based alloys such as PtPb [171, 176, 177], PtIr [178], and PtRu [179], exhibit higher catalytic activity and anti-interference ability than pure Pt, generating more stable and larger responses. We have found that our PtNi nanoparticles-ERGO based electrode shows significantly improved response current toward glucose oxidation as well as remarkable stability, selectivity and reproducibility, in comparison with a number of control electrode materials including PtNi nanoparticles-CRGO nanocomposites. This

should result from the synergistic contribution of more efficient electrochemical reduction of GO and higher loading density of the alloy nanoparticles on ERGO.

2.2 Experimental section

Preparation of Samples. Graphite oxide was prepared according to the modified Hummers method from graphite powder [21]. Sonication is employed to achieve the exfoliation of graphite oxide into graphene oxide (GO). The CRGO was prepared by hydrazine reduction at 95 °C for 1 h [25]. 10 μL of 0.1 mg/L pretreated exfoliated GO suspension was transferred on a cleaned GCE or ITO to obtain GO coated electrode (i.e., GO/GCE). The electrochemical reduction of GO/GCE and the electrochemical deposition of PtNi nanoparticles on GO/GCE were performed in 0.2 M Na_2SO_4 solution with 0.5 mM H_2PtCl_6 and 50 mM $NiSO_4$. The deposition time was carried at -1.0 V (vs. Ag/AgCl) for 300 s with the aid of sonication [180].

Materials Characterization. Electrodeposition and electrochemical measurements, including impedance spectroscopy (EIS), cyclic voltammetry (CV), linear sweep voltammetry (LSV) and chronoamperometry, were carried on an electrochemical workstation (CHI 660D). The modified glassy carbon electrode or an indium tin oxide (ITO) glass were used as working electrodes, while Pt foil and Ag/AgCl as counter and reference electrtodes. For EIS, the frequency range was 0.1 to 1×10^5 Hz. The morphology of the prepared materials was obtained from atomic force microscopy (AFM) (Asylum Research) and scanning electron microscope (SEM) (JSM-6700F). Fourier transform infrared (FT-IR) spectra were obtained on a Perkin-Elmer Spectrum

One Spectrometer. X-ray photoelectron spectroscopy (XPS) was taken on a Kratos-Axis spectrometer.

2.3 Results and discussion

2.3.1 Characterization of PtNi-ERGO nanocomposites.

The electrochemical response of a surface is highly sensitive to its physicochemical properties. The CV of the starting GO/GCE in a potential range of -0.6 to -1.2 V exhibits a cathodic current peak at -0.95 V in phosphate buffer solution (PBS, pH = 7.4) (**Figure 2.2**A), owing to the reduction of the oxygen functionalities on GO. After electrodeposited in the metal ions precursor solution containing 0.5 mM H_2PtCl_6 plus 50 mM $NiSO_4$ for 300 s, the PtNi-ERGO/GCE was obtained, and the reduction current at this potential range disappeared. This suggests that the surface-oxygenated species at GO has be completely reduced electrochemically [51], also evidenced by the color change of the electrode coated with samples from yellow to black (**Figure 2.2**D).

The FT-IR spectrum (**Figure 2.2**B) of GO shows the presence of C-O at 1065 cm^{-1}, C-O-C at 1225 cm^{-1}, C-OH at 1400 cm^{-1}, C=C at 1620 cm^{-1}, and C=O at 1740 cm^{-1}. After electrochemically reduced, the peaks of oxygen functionalities (i.e., C-O at 1065 cm^{-1}, C-O-C at 1225 cm^{-1}, C-OH at 1400 cm^{-1} and C=O at 1740 cm^{-1}) disappear, only the peak of C=C at 1620 cm^{-1} remains, confirming the reduction of GO at negative potential [163]. There are two peaks in the Raman spectrum of GO, i.e., 1355 and 1590 cm^{-1} in accordance with the D and G bands (**Figure 2.2**C), respectively. Although both D and G bands at 1355 and 1590 cm^{-1} was observed on ERGO, the intensity ratio of D/G

increased significantly, attributing to the increased defect in ERGO than GO and indicating the successful deoxygenation in ERGO [181].

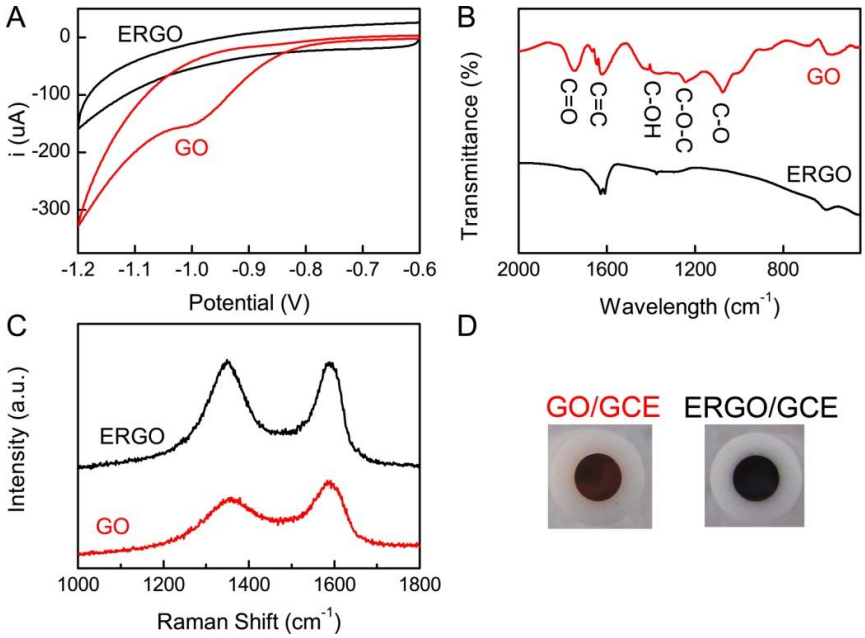

Figure 2.2 (A) CV curves of GO/GCE before and after electrochemical reduction in 0.2 M Na_2SO_4 solution with 0.5 mM H_2PtCl_6 and 50 mM $NiSO_4$. Supporting electrolyte: 0.1 M PBS (pH = 7.4); Scan rate: 50 mV/s. (B) FT-IR transmittance spectra, and (C) Raman spectra of GO and ERGO. (D) The photos of the GO modified electrode before and after electrochemical reduction.

The thickness of GO sheets is about 1.0 nm, similar to the previously reported thickness (1-2 nm) of GO sheets [5], indicating that GO was exfoliated into single or very thin layers. The GO film deposited on GCE displays the characteristic wrinkle morphology, as observed in the SEM images (**Figure 2.3**A). And the electrochemical reduction in the metal ion precursor solution (0.5 mM H_2PtCl_6 and 50 mM $NiSO_4$) led to the formation of a dense layer of spherical metal nanoparticles deposited on it (**Figure 2.3**B). Observation under higher magnification reveals the well-dispersed PtNi nanoparticles on the wrinkly ERGO support (**Figure 2.3**C). These nanoparticles exhibit faceted

characteristics and their shape are mostly spherical, with a diameter of about 80 nm. Another finding is that these nanoparticles are stable under the ultrasonic condition, and the resulting biosensor based on these nanoparticles exhibit outstanding performance with long-term stability, which to some extent manifests that the metal nanoparticles are immobilized on GO through stable bonding such as complex interaction, not simple physical adsorption [26]. Moreover, because the applied potential in the electrodeposition is far beyond the equilibrium (Nernst) potential for the reduction of Pt and Ni, the nuclei form instantly when the potential is applied, and subsequently grow with the time.

Under the same condition, electrodeposition on CRGO led to sparsely distributed nanoparticles with a range of wide size distribution (**Figure 2.3**D and E). The high surface coverage of metal nanoparticles on ERGO should benefit from the intrinsic surface properties of GO. Surface functional groups can serve as anchoring sites for the metal nanoparticles. Collectively, nanoparticles of defined sizes were formed on the GO sheets. Whereas for CRGO, most oxygenated species are removed by chemical treatment, resulting in the low affinity of the metal nanoparticles on its surface. Importantly, the highly dispersed and dense metal nanoparticles on supports without any agglomeration usually exhibit a large surface area, which corresponds to higher catalytic activity and sensitivity [182].

Additionally, the polar surface functional groups make GO highly dispersible in aqueous medium. Therefore, both of the GO film deposited from its homogenous aqueous dispersion and the resulted ERGO film is even and uniform. In contrast, as CRGO restores the sp^2 graphite structure, its dispersity in aqueous medium dramatically decreased and can only form unstable

suspension. As a result, the deposited CRGO film exhibited uneven patchy structure (**Figure 2.3**E).

PtNi nanoparticles were also deposited on single-walled carbon nanotubes (SWNTs) under the same condition for comparison. In comparison with graphene, SWNTs possess similar stable physical properties but smaller surface areas, which can be considered as rolled graphene [183]. Unlike the uniformly dispersed nanoparticles on graphene surfaces, PtNi nanoparticles are mainly grown at the tips of the SWNTs and exhibit snowflake-like agglomeration morphology with diameters from 100 to 200 nm (**Figure 2.3**F). This difference in nanoparticle deposition should be associated with the different spatial distribution of the electrical fields of graphene and SWNTs, leading to absence of PtNi nanoparticles on the sidewalls and serious aggregation on the tips of the tubes [179]. Aggregation is a serious problem in the development of nanoelectrocatalyst film since it reduces the active surface area.

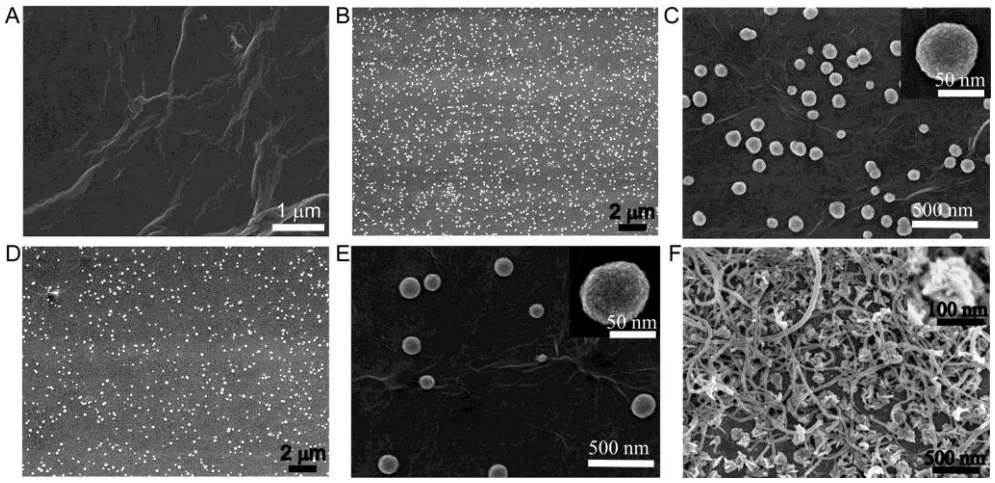

Figure 2.3 (A) SEM images of GO; SEM image of (B) PtNi-ERGO, (D) PtNi-CRGO, and (F) PtNi-SWNT. (C, E) Magnified SEM images of PtNi-ERGO and PtNi-CRGO, respectively.

The XPS peaks centered at the Pt, Ni, C and O core level regions can be assigned to Pt 4f, Ni 2p, C1s and O1s, respectively, which further support that bimetallic PtNi nanoparticles have been effectively anchored on graphene sheets (**Figure 2.4**A). Deconvolution of the Pt 4f signal in both PtNi-ERGO and PtNi-CRGO shows three pairs of doublets (**Figure 2.4**B). The most intense peaks at 71.8 eV (Pt $4f_{7/2}$) and 75.1 eV (Pt $4f_{5/2}$) is attributed to metal Pt. Peaks at 72.9 and 76.7 eV could be assigned to Pt^{2+}. The third doublet found at 74.5 and 77.7 eV appears to be Pt^{4+} [184]. High-resolution XPS scan of the PtNi-ERGO composite shows that the atomic percentage of Pt is ~10.38%, and the atomic ratio of Pt/Ni is 3/1. For PtNi–CRGO nanocomposite, the atomic percentage of Pt/Ni is similar, but the intensities of XPS peaks in the as-synthesized composites are obviously reduced and the atomic percentage of Pt decreases to ~2.28%. The decrease in Pt content is consists with the EDS result. There are systematic differences in the alloy compositions obtained from XPS and EDS. This is because EDS characterizes the entire sample, whereas XPS probes a thin surface layer. Taken together, the XPS and EDS data can provide the overall composition of as-prepared alloy nanoparticles.

The XPS spectrum of GO indicates the presence of C=C (284.6 eV) and C=O (286.7 eV) (**Figure 2.4**C) [35]. After its electrochemical or chemical reduction, the peak of C=C became dominant, and the peaks related to the oxygen species are significantly weakened. High-resolution XPS scan of the ERGO composite shows higher atomic percentage of C/O (8/1), in comparison with its precursor GO (2/1) or CRGO (7/1). This indicates the more effective deoxygenation of GO by electrochemical reduction process than chemical reduction, an important factor for improving the electrical conductivity.

Therefore, LSV, IR, and XPS collectively demonstrate that GO is successfully reduced to ERGO during the electrodeposition of PtNi nanoparticles.

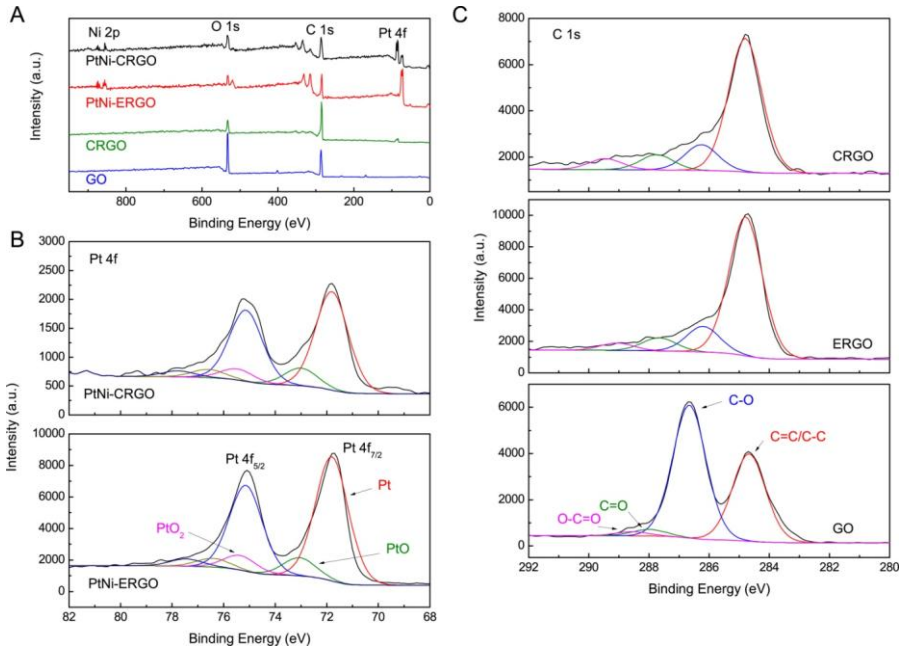

Figure 2.4 (A) XPS spectra of GO, CRGO, PtNi-ERGO and PtNi-CRGO; (B) Fitted curve of Pt 4f spectra of PtNi-ERGO and PtNi-CRGO; (C) Fitted curve of C 1s spectra of GO, PtNi-ERGO, and CRGO.

The conductivity of different composites was tested by the impedance spectroscopy on different electrodes in $[Fe(CN)_6]^{3-/4-}$. After fitting plots according to the equivalent circuit (**Figure 2.5**A), we can get the bulk resistance (R_b), Faradic resistance (R_{ct}), and Warburg impedance (W) for different electrodes. PtNi-ERGO/GCE exhibits remarkable low values of R_b (about 10 Ω), R_{ct} (about 300 Ω) and W, indicating that PtNi-ERGO/GCE is an excellent electrode material for electrochemical application. The semicircle of bare GCE is big and the electron transfer resistance is high (R_{ct} = 652 Ω). After modified with exfoliated GO acts as an insulating layer and the semicircle dramatically increases (R_{ct} = 926 Ω), making the interfacial charge transfer more difficult.

Moreover, the electrostatic repulsion between the negative surface charges of GO and ferricyanide and ferrocyanide ions impairs the access of the ions onto the electrode surface, also contributing to the increased resistance [157]. When GCE was coated with PtNi-CRGO or PtNi-ERGO nanocomposites, the electron transfer resistance decreased markedly. Two structural factors are responsible for the reduced resistance. First, PtNi alloy nanoparticles have excellent electrical conductivity and can provide essential pathways in accelerating the electron transfer. Second, due to the restoration of a sp^2 bonds, the electrical conductivity of ERGO and CRGO films is improved significantly, so the electron transfer between $[Fe(CN)_6]^{3-/4-}$ and the prepared electrodes is accelerated by ERGO and CRGO.

The CVs of PtNi/GCE, PtNi-CRGO/GCE, PtNi-SWNT/GCE and PtNi-ERGO/GCE in deaerated 0.5 M H_2SO_4 were collected at a slow potential sweep rate (i.e. 20 mV/s) and the same potential limit (**Figure 2.5**B). The typical character peaks of Pt from hydrogen adsorption-desorption as well as the oxide formation-stripping indicate that Pt-based alloy nanoparticles have been effectively loaded on the supports. No current was detected from Ni oxidation or dissolution, suggesting that the particle surface is covered by a Pt-rich layer, and that the neighboring Pt atoms stabilize the Ni atoms [185]. From hydrogen adsorption-desorption peaks we calculated the electrochemically active surface area (S_{EAS}), expressed as: $S_{EAS} = 0.1\ Q_{ads}/Q_{ref}\ L_{Pt}$, where Q_{ads} is the integrated hydrogen adsorption charge, Q_{ref} is the hydrogen adsorption charge on smooth Pt (0.21 mC/cm^2) and L_{Pt} is the Pt amount loaded (mg) [186]. S_{EAS} values follow the order of PtNi-ERGO/GCE (144.5 m^2/g) > PtNi-CNT/GCE (95.86 m^2/g) > PtNi-CRGO/GCE (56.30 m^2/g) > PtNi/GCE (27.39 m^2/g). The largest

active surface area of PtNi-ERGO/GCE indicates its promising potentials for electrocatalysis and electrochemical sensor design.

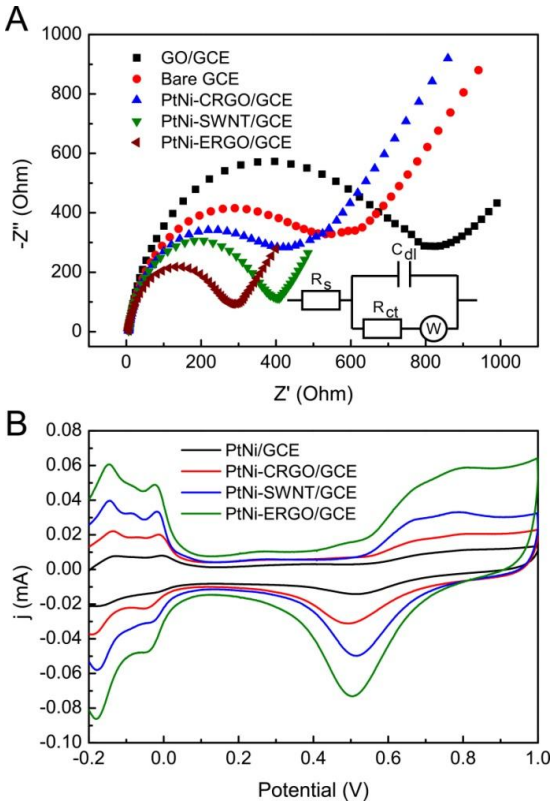

Figure 2.5 (A) Nyquist plots of GO/GCE, bare GCE, PtNi-CRGO/GCE, PtNi-SWNT/GCE and PtNi-ERGO/GCE in 0.1 M KCl with 1.0 mM $K_3Fe(CN)_6$ and 1.0 mM $K_4Fe(CN)_6$. Frequency range: 0.1 - 10^5 Hz. The inset is the equivalent circuit. (B) CVs of PtNi/GCE, PtNi-CRGO/GCE, PtNi-SWNT/GCE and PtNi-ERGO/GCE. Supporting electrolyte: 0.5 M H_2SO_4 saturated with nitrogen gas; Scan rate: 20 mV/s.

2.3.2 Electrocatalytic activity towards glucose oxidation.

In blank PBS, we observed the hydrogen adsorption-desorption waves, the typical electrical double layer region, and the Pt oxide formation/reduction waves from negative to intermediate and to positive potentials on ERGO/GCE (**Figure 2.6**A). Multiple oxidation peaks were observed during the positive potential sweep when exposed to 10 mM glucose. The current peak I at ca. -

0.35 V can be attributed to the preferentially electrosporption of glucose on the PtNi due to the formation of glucose intermediates (e.g., the enediol type). While the potential scanning positively, the adsorbed glucose intermediates are oxidized, with a small current peak (peak II at ca. 0.15 V). When the potential further increased, the accumulated intermediates will block the active sites on PtNi, which inhibits the electroadsorption of glucose and leads to the drop of current. When potentials go beyond 0.4 V, the adsorbed intermediates can be further oxidized, with the formation of gluconolactone or gluconic acid (peak III at ca. 0.55 V). At even higher potential, metal oxide are formed, and the surface becomes passivated with a decreased current again. In the negative scan, the metal oxide first inhabits the oxidation of glucose. Active sites for glucose oxidation are released in the potential range of 0.0 to -0.5 V, due to the reduction of Pt oxide on the surface [171-179].

We cannot observe redox peaks in the CVs of the bare electrodes without metal nanoparticles, suggesting there is activity towards glucose oxidation on these electrodes (**Figure 2.6**B). On PtNi/GCE, PtNi-CRGO/GCE, PtNi-SWNT/GCE and PtNi-ERGO/GCE, three oxidation peaks are observed in the anodic potential scan. PtNi-ERGO/GCE gave us the more negative potential for glucose oxidation with higher current response than those of PtNi/GCE, PtNi-CRGO/GCE and PtNi-SWNT/GCE, especially at lower potential, demonstrating that the higher electrocatalytic activity of PtNi-ERGO/GCE.

Long-term oxidation of glucose on three types of metal (i.e., PtNi, PtCo and Pt) nanoparticles-ERGO modified electrode was tested via chronoamperometric experiments under the near-peak potential (**Figure 2.6**C). Pt-ERGO/GCE suffers from serious poisoning, while PtNi-ERGO/GCE and

PtCo-ERGO/GCE demonstrate a relatively higher current density for a long period. The presence of non-noble metal in the alloy can remove poisonous intermediates and promote electron-transfer reactions owing to their superior catalytic effect to monometallic Pt nanoparticles. Two effects are contributed to the enhanced catalytic activity of bimetallic systems: One is "bifunctional effects", relating to the change of geometry of bimetallic systems with respect to monometallic systems; the other is "ligand or electronic effect", the role of Co and Ni is a catalytically enhancing agent, which could modify the electronic properties of the Pt [187]. The LSV responses of PtNi-ERGO/GCE fabricated in the electrodeposition solution with different deposition time to glucose are compared. The current increases with longer deposition time, with about 40 mV shifts to more negative potential observed (**Figure 2.6**D). This is due to the increase of PtNi alloy nanoparticle sizes and the possible reduction of S_{EAS}. The deposition time is hence fixed at 300 s.

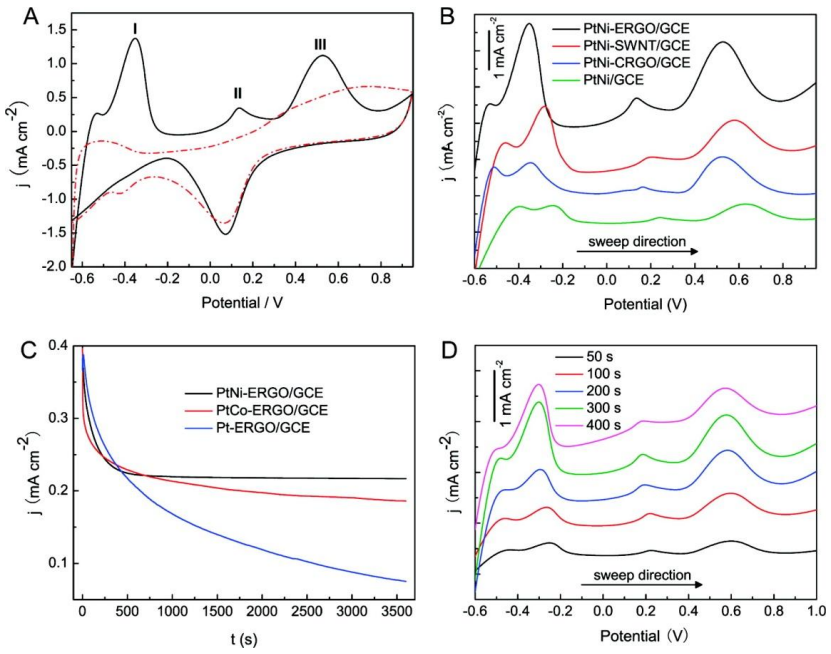

Figure 2.6 (A) CVs of a PtNi-ERGO/GCE with (red dashed line) and without (black solid line) of glucose. (B) LSVs of PtNi/GCE, PtNi-CRGO/GCE, PtNi-

SWNT/GCE and PtNi-ERGO/GCE in 10 mM glucose solution. Scan rate: 10 mV/s. (C) Chronoamperometric curves of PtNi-ERGO/GCE, PtCo-ERGO/GCE, Pt-ERGO/GCE. Applied potential: -0.35 V. (D) LSVs of PtNi-ERGO/GCE at various deposition time of 50, 100, 200, 300, and 400 s in 10 mM glucose solution. Supporting electrolyte: PBS (pH = 7.4) saturated with nitrogen gas. Scan rate: 10 mV/s.

2.3.3 Amperometric measurement of glucose.

The sensor based on PtNi-ERGO responds linearly with glucose concentration up to 35 mM, and has a detection limit of 0.01 mM (**Figure 2.7**A). These analytical performance parameters are comparable or even superior to those reported in literatures concerning the Pt-based nonenzymatic glucose sensor [158], for example, PtPb nanoparticles (linear range up to 5 mM and detection limit of 0.0018 mM) [176], PtPb networks (linear range up to 16 mM) [171], PtPb nanowire (linear range up to 11 mM and detection limit of 0.008 mM) [177], PtIr alloy (linear range up to 10 mM) [178], PtRu nanoparticle (linear range up to 20 mM and detection limit 0.05 mM) [179]. This linear response is quite appropriate for detection of glucose in real samples.

Although glucose has higher concentrations in normal physiological conditions (3.5-6.1 mM) than the redox-active interfering species, e.g. ascorbic acid (AA) (0.1 mM) uric acid (UA) (0.02 mM), and acetamidophenol (AP) (0.1 mM), their electron transfer rates are higher than that of glucose. Consequently, the oxidation current of them is comparable to that of glucose. Therefore, AA, UA and AP are major interfering species for the detection of glucose. To avoid the interference, an effective method is to detect glucose at more negative potential. We explored the influence of operating potential on the electro-oxidation of 0.5 mM AA, 0.1 mM UA, 0.1 mM urea, 0.5 mM acetaminophen

(AAP) and 0.5 mM fructose, and 5.0 mM glucose at the PtNi-ERGO/GCE. The oxidation current of glucose is quite prominent between 0 and -0.35 V, whereas the oxidation currents of AA, UA, urea and AAP are very small. Furthermore, when the potential was lowered to -0.35 V, the amperometric signals of AA, UA, AP, urea, AAP, and fructose disappeared completely (**Figure 2.7**B). Taking into account the sensitivity of the biosensor and interference of easily oxidized compounds presenting in samples, amperometric measurement of glucose was taken at -0.35 V in the following experiments.

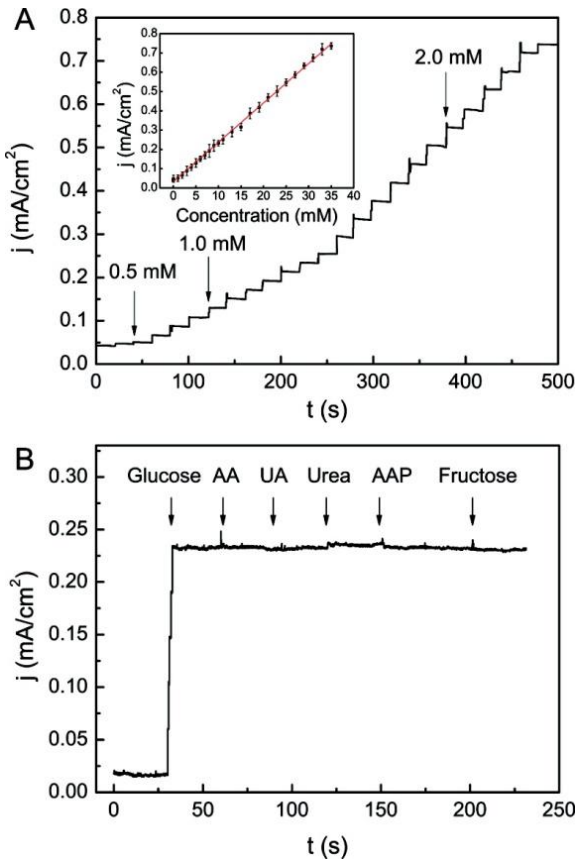

Figure 2.7 (A) Typical amperometric response of PtNi-ERGO/GCE to successive addition of 0.5, 1.0 and 2.0 mM glucose. And the calibration curve (insert). (B) Influence of interferences (0.5 mM AA, 0.1 mM UA, 0.1 mM urea, 0.5 mM AAP and 0.5 mM fructose, from left to right) on the response of 5.0 mM glucose. Applied potential: −0.35 V.

We also tested the influence of other foreign species possibly existing in real samples, including urea, fructose, ethanol, glycin, lactamine, serine, aspartic acid, cysteine, xanthine, hypoxanthine, guanine, adenine, thymine, cytosine, Al^{3+}, Fe^{3+}, Fe^{2+}, Ni^{2+}, Co^{2+}, Hg^{2+}, Ca^{2+}, Mg^{2+}, Cd^{2+}, Mn^{2+}, Pb^{2+}, Zn^{2+}, Bi^{2+}, Cl^{-}, SO_4^{2-}, SO_3^{2-}, NO_3^{-}, CO_3^{2-} and ClO_4^{-}. Our results have shown the foreign species (0.5 mM or 1.0 mM) only led to minimal changes relative to the response current of 5.0 mM glucose, generally less than 5.0%, compared with that recorded in absence of the foreign substance.

The reproducibility and stability of the sensor are also evaluated. The current response of ten electrodes modified identically to 1.0 mM glucose at -0.35 V displayed a relative standard deviation (RSD) less than 5.0 %, confirming that the sensor is highly reproducible. Ten successive measurements using one sensor yielded an RSD of 4.2 %, indicative of the stability of the sensor for long term uses. The stability of PtNi-ERGO/GCE stored at room temperature is investigated by periodically recording its current response to 10.0 mM glucose. The nonenzymatic sensor retained 93.2% and 90.5% of its initial sensitivity at 10 and 50 days post-preparation, respectively.

3. Graphene paper modified with copper nanocubes as flexible electrodes for hydrazine fuel cells

3.1 Introduction

Direct liquid fuel cells, a sort of power sources especially suitable for hybrid vehicles and portable electric devices, are actively explored in recent years [188, 189]. Hydrazine exhibits attractive features for liquid fuel cells, including high theoretical cell voltage of 1.61 V with expected high power density, high hydrogen content equivalent to methanol, easier transportation and storage than hydrogen, and no greenhouse gases emission [190]. Since the early development of hydrazine-based alkaline fuel cells [191, 192], research on direct hydrazine fuel cells (DHFC) has been focused on developing catalysts with improved performance, particularly Pt-based systems and new device designs [193-195]. Rapid progressions in the past decade have manifested that DHFC hold great promise in the commercialization of high-performance and portable fuel cells [196-198]. The catalyst layer is the critical component of fuel cell to convert chemical energy into electricity [199]. A conventional two-step method to prepare the catalyst layer involves dispersing catalyst in a binder (such as Teflon or Nafion) to form a slurry, followed by coating the slurry on carbon substrates [200]. This process usually results in serious agglomeration of catalyst particles and poor adhesion of catalyst to the substrate, which typically leads to reduced active surface areas and stability of the catalysts. And addition of the binder can possibly block active sites of the catalyst. To overcome these problems, great efforts have recently been devoted to improving the existing

systems from two aspects such as designing new building blocks (carbon substrates [201, 202] and catalysts [203]) and developing innovative approaches [204-206] for better structural integration of the components.

Graphene paper (GP), assembled from individual graphene sheets, is characterized of a unique set of electrical and structural properties, e.g., high electrical conductivity, outstanding mechanical strength, and excellent chemical and thermal stability. These properties make GP-based composites intriguing electrode materials for supercapacitors [135, 207, 208] and lithium ion batteries [137, 209] to electrochemical biosensors [91]. However, the potential of using GP to improve the performance of fuel cell has not been demonstrated, although GP appears to be suitable carbon substrates for the catalyst layer given their mechanical stability and chemical inertness [81]. On the other hand, considerable interest has been focused on developing noble-metal-free catalysts, such as Ni, Co and Cu-based catalysts for DHFC to reduce the cost and minimize the poisoning effort associated with classical Pt-based catalysts [210]. Previous reports have shown that Ni and Co-based catalysts have to function at relatively higher temperature (50-80 ℃) because of decreased activity induced by surface oxidation at low temperature [211]. In this chapter, we present the development of Cu nanocube-loaded free-standing GP (Cu-GP) as a new type of flexible electrode materials to catalyze hydrazine oxidation [212]. Our results have demonstrated that Cu nanocubes directly grown on GP substrates through template-free electrodeposition exhibits highly-stable catalytic activity against hydrazine oxidation in alkaline conditions at room temperature. We also found that an in-situ formed layer of copper hydroxide/oxide on Cu nanocube surfaces can enhance the electrocatalytic activity and stability of the electrocatalyst. We

envision that Cu-GP nanocomposites can serve as a binder-free catalyst layer in DHFC, thus effectively minimizing the above-mentioned problems.

3.2 Experimental section

Preparation of Samples. GO aqueous solution (30 mL, 0.1 mg/mL) with pH adjusted to 10 by ammonia was transferred to an autoclave with 45 mL capacity for hydrothermal treatment in an oven (180 ℃ for 12 h) to get hydrothermally reduced GO [49]. GP was prepared by filtrating the dispersion of rGO through cellulose acetate membrane filters (47 mm in diameter and 200 nm in pore size, Sartorius-Stedim). The electrodeposition of Cu nanocubes on GP was performed in KCl solution (0.1 M) containing $CuCl_2$ (10 mM) by applying a negative potential of -0.4 V (vs. SCE), which is negative enough for the electrochemical reduction of Cu^{2+} to Cu^0 [213].

Materials Characterization. Electrochemical measurements of hydrazine oxidation were tested in KOH (0.1 M) aqueous solution with hydrazine (10 mM) at 20 ℃. The working electrode was a modified GP electrode. Pt wire and a saturated calomel electrode (SCE) were used as counter and reference electrodes, respectively. X-ray diffraction (XRD) patterns were collected with a Bruker AXS D8 X-ray diffractometer equipped with monochroomatized Cu Kα radiation (λ = 1.54056 Å, 40 kV and 20 mA). Raman spectrometer (Reinshaw Raman Scope RM3000) was used to obtain the Raman spectra with wavelength of 633 nm (1.96 eV).

3.3 Results and discussion

3.3.1 Characterization of Cu-GP

We first prepared the bright yellow dispersion of graphene oxide (GO) from graphite powder by the commonly used the Hummers' method (inset of **Figure 3.1**A). After hydrothermal treatment of GO dispersion at 180 ℃ for 12 h, a stable and black dispersion of graphene was obtained (inset of **Figure 3.1**B). The distinct color change of the dispersion before and after hydrothermal reaction indicates that reduced GO (rGO) is formed. AFM images reveal that resultant GO and rGO deposited on silicon wafer by spin-coating have a typical lateral dimension of hundreds nanometers. Graphite was completely exfoliated into single-layered GO sheets, as revealed by their thickness around 1.0 nm. The thickness of hydrothermally reduced GO decreased to 0.8 nm owing to the removal of the surface oxygen functionalities on GO sheets. XPS was further employed to detect the constitutional change of hydrothermally treated GO. As shown in **Figure 3.1**C, deconvolution of the C 1s signal in GO sample displays the presence of C=C/C-C (~284.6 eV), C-O (~286.5 eV), C=O (~288.3 eV) and O-C=O (~290.3 eV) functional groups [35], with a low atomic percentage of C/O (2/1). The intensities of the peaks assigned to the heavily oxygenated carbon species decrease significantly in the reduced products, and the peak associated with C=C (~284.6 eV) becomes the dominant species (**Figure 3.1**D). And the resultant rGO sample shows a much higher atomic percentage of C/O (8/1). The effective deoxygenation of GO by the hydrothermal reduction process is expected to improve the electrical conductivity of graphene which is an essential criteria for the support material in catalyst layers [214].

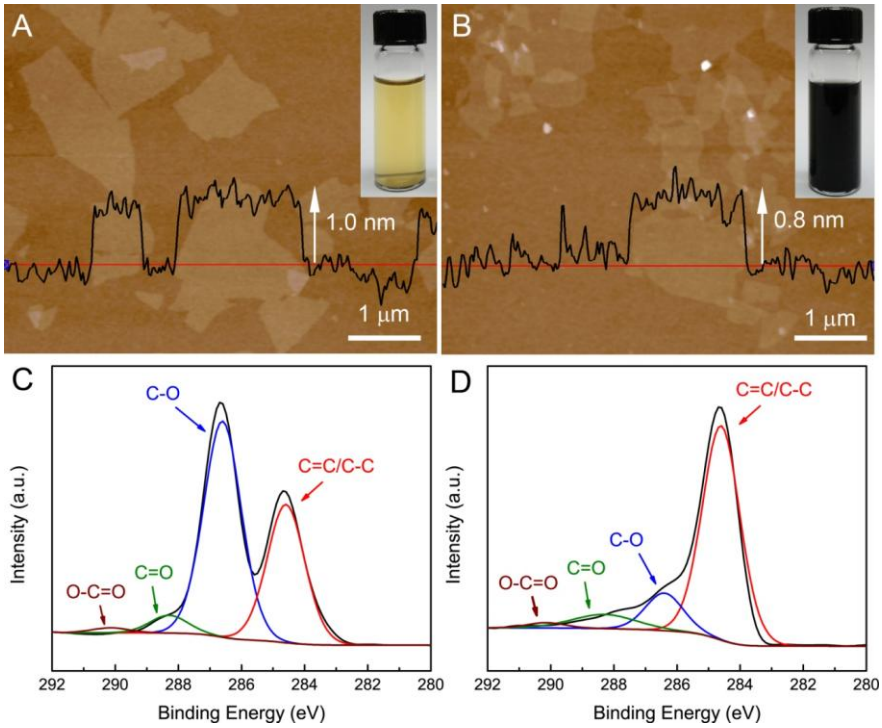

Figure 3.1 AFM images of (A) as-synthesized GO and (B) hydrothermally reduced GO spin-coated on silicon wafer, inset shows their corresponding aqueous dispersions; C 1s XPS spectra of (C) GO and (D) hydrothermally reduced GO.

The flexible free-standing GP, prepared by the vacuum filtration method, exhibits metallic luster on its surface (**Figure 3.2**A). During the filtration process, graphene sheets tend to self-assemble in a sheet-by-sheet manner at the liquid-solid interface, driving the formation of a uniform and layered GP through the entire cross-section (**Figure 3.2**B and C) [82]. Figure 3.2D shows a typical top-view SEM image of pristine GP, in which the graphene sheets assembled to form a smooth surface with characteristic wrinkles arising from the flexibility of graphene sheets (**Figure 3.2**D). GP with high electrical conductivity can be directly employed as working electrode for the electrodeposition of Cu nanocubes. The surface oxygen functionalities on graphene sheets can serve as the nucleation sites for metal nanoparticles [148,

154]. After applying a negative potential (-0.4 V) in KCl (0.1 M) and $CuCl_2$ (0.01 M) solution for 60 s, a dense layer of well-dispersed Cu nanocubes with a type size of around 50 nm was decorated on the surface of GP (**Figure 3.2**E). Energy dispersive X-ray spectroscopy (EDS) spectra show the predominant peaks corresponding to C and Cu elements (**Figure 3.2**F), also confirming the successful electrodeposition of Cu nanocubes on GP.

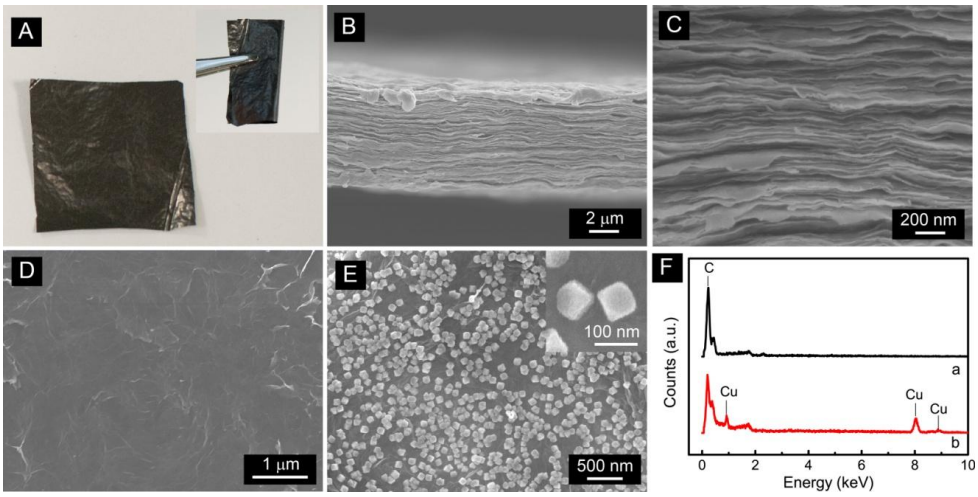

Figure 3.2 (A) Photographs of 2 cm × 2 cm GP; (B and C) SEM images of cross-section views of GP at different magnifications; (D) SEM image of a top view of GP; (E) SEM images of Cu nanocubes electrodeposited on GP; (F) EDS spectra of GP (a) and Cu-GP (b).

From the XRD patterns (**Figure 3.3**A), we calculated the relatively larger interlayer distance of GO (~0.8 nm, $2\theta = 10.3°$) due to the presence of hydroxyl, epoxy and carboxyl groups. After elimination of oxygen functionalities and possible restacking of the sheets, the interlayer distance of GP decreases to 0.34 nm ($2\theta = 25.0°$) [43]. XRD pattern of Cu-GP clearly shows three major peaks in the range of 10 to 80 °, arising from the diffraction of (111), (200) and (220) planes of Cu(0) with face-centered cubic (fcc) lattice [215]. Raman spectra were further used to determine the microstructures of GO, GP and Cu-GP

(**Figure 3.3**B). Arising from D and G bands, there are two prominent peaks (1352 and 1594 cm^{-1}) in GO and GP. However, their intensity ratio (I_D/I_G) increased from 0.8 for GO to 1.0 for GP, indicating the formation of partially ordered pristine graphene structure [35]. Deposition of Cu nanocubes did not have any impact on the Raman spectral profile of the GP substrate.

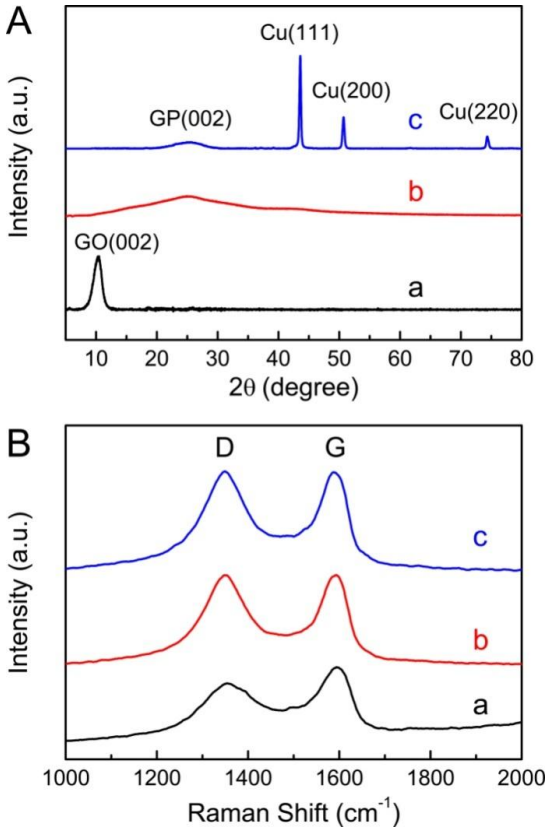

Figure 3.3 (A) XRD patterns and (B) Raman spectra of GO (a), GP (b) and Cu-GP (c).

EIS was performed to probe the impedance changes of GP and Cu-GP (**Figure 3.4**). The semicircular part of the plot at higher frequencies arises from the electron transfer limited process, and the diameter of the semicircle indicates the electron transfer resistance (R_{et}). The linear part at lower frequencies is related to the diffusion controlled process [216]. R_{et} of GP was estimated to be 315 Ω, which dropped to be 141 Ω after the electrodeposition of

Cu nanocubes, indicating that Cu nanocubes enhanced electron transfer on Cu-GP electrode.

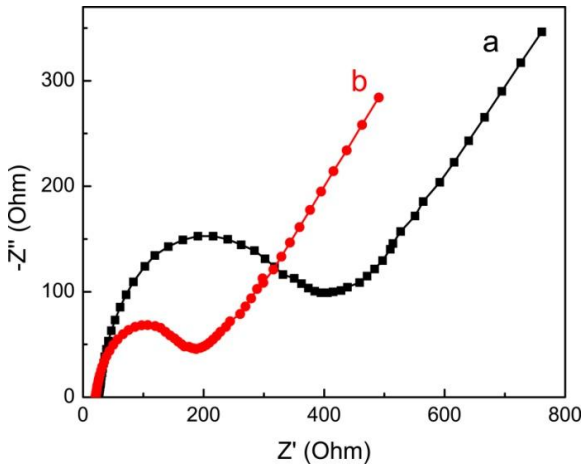

Figure 3.4 Nyquist plots of GP (a) and Cu-GP (b) in 0.1 M KCl electrolyte solution containing 1.0 mM $K_3Fe(CN)_6$ + 1.0 mM $K_4Fe(CN)_6$ in the frequency range of 0.1 Hz to 10^5 Hz.

3.3.2 Electrochemical oxidation of hydrazine on Cu-GP

The cyclic voltammograms (CV) of GP and Cu-GP in 0.1 M KOH containing 10 mM hydrazine are compared in **Figure 3.5**. On the bare GP composed of graphene sheets with defects and oxygen-functional groups as the catalytic sites, a peak current (i_p) at 0.80 V was observed arising from the hydrazine electro-oxidation [217]. In contrast, Cu-GP exhibits higher electrocatalytic activity toward hydrazine electrooxidation than GP, which is supported by a 10-fold increase of peak current and an overall negative shift of peak potential (E_p) to 0.30 V. The onset potential for hydrazine oxidation on Cu-GP is as low as -0.10 V, reflecting a fast electron-transfer reaction on the Cu-GP due to the high catalytic effect of Cu nanocubes. Furthermore, the reverse scan gives no corresponding cathodic peak, suggesting a totally irreversible oxidation of hydrazine in alkaline solutions on Cu-GP. Taking into

account the onset potentials, Cu-GP exhibits remarkable activity towards hydrazine oxidation in comparison with the rigid electrode materials previously reported, such as Ni-Co alloy (-0.39 V) [218], TiO_2-Pt hybrid nanofibers (-0.14 V) [219], Nano-Au/Porous-TiO_2 (0.00 V) [220], Pd/WO_3 (0.10 V) [221], porous Mn_2O_3 nanofibers (0.06 V) [222], and Fe_2O_3 graphite composite (0.30 V) [223]. In addition, the free-standing Cu-GP electrode offers great flexibility for potential applications in portable and microelectronic devices [224].

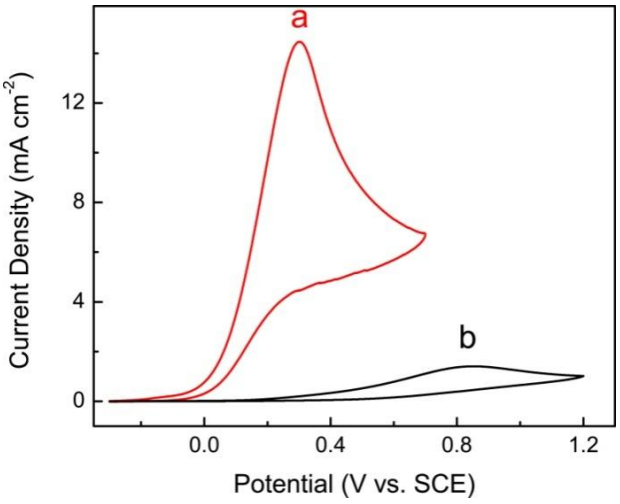

Figure 3.5 CVs of Cu-GP (a) and GP (b) in 0.1 M KOH containing 10 mM hydrazine at a scan rate of 100 mV/s.

Another interesting observation is that an anodic peak (-0.10 V) appeared in the first CV cycle of Cu-GP, and totally disappeared in the following cycles (**Figure 3.6**A). XPS spectra were used to identify the change of Cu surface species before and after the first CV cycle (**Figure 3.6**B). The presence of Cu(II) on Cu nanocubes after the first CV cycle is supported by the considerably broader Cu $2p_{3/2}$ and Cu $2p_{1/2}$ peaks, and new shake-up satellites peaks at ca. 10 eV higher binding energy from the primary copper peaks (933.7 and 953.6 eV). No such satellite peaks are present in the case of Cu metal and Cu_2O [225]. Cu

and Cu_2O cannot be easily distinguished since the shape and binding energy of their peaks are quite similar [226].

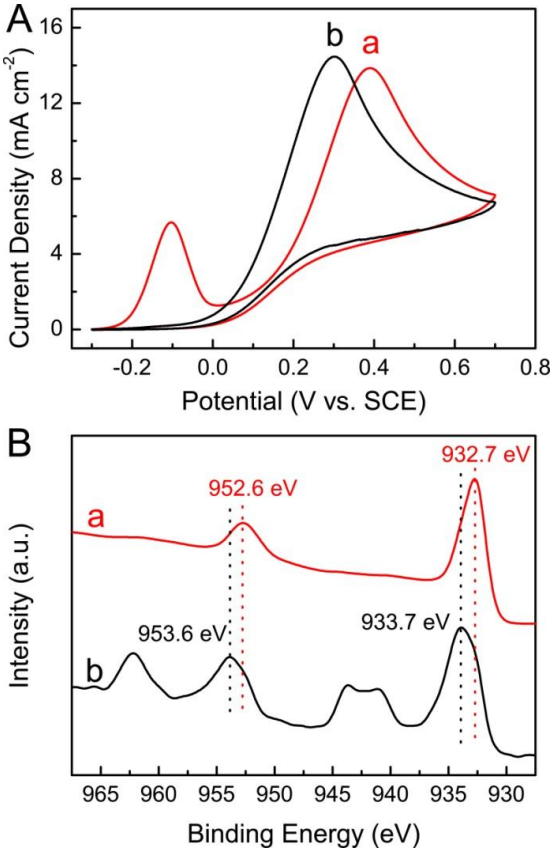

Figure 3.6 (A) Cyclic voltammograms of the first (a) and second (b) scans of Cu-GP in 0.1 M KOH containing 10 mM hydrazine at a scan rate of 100 mV /s; (B) XPS spectra of Cu-GP before (a) and after (b) the first cyclic voltammetry.

Nevertheless, the XPS results support the formation of a stable layer of Cu hydroxide/oxide on the Cu nanocube surfaces. The in-situ formed Cu hydroxide/oxide layer can transfer between different oxidation states of Cu(II) and Cu(I) and consequently act as mediators to shuttle electron transfers between hydrazine and the catalysts [227, 228]. In the first cycle, hydrazine is mainly oxidized on the bare Cu surfaces that have higher overpotential for the oxidation of hydrazine [229]. In the following cycles, hydrazine is oxidized on

the Cu hydroxide/oxide layer that formed on Cu surfaces, leading to a negative shift (about 0.1 V) of peak potential for hydrazine oxidation.

3.3.3 Electrochemical oxidation mechanism of hydrazine on Cu-GP

The effect of scan rate (v) is also investigated (**Figure 3.7**A). E_p shifted toward positive direction with increasing v, and a linear relationship is found between E_p and log(v), $E_p = 0.397 + 0.104 \log(v)$ ($r^2 = 0.998$, r: regression coefficient, E_p : V, v : V/s), demonstrating the oxidation of hydrazine on Cu-GP is an irreversible process. According to the equation: $E_p = 1/2b\log(v)$ + constant, where $b = 2.3RT/[(1-\alpha)n_\alpha F]$, if assuming the electron transfer coefficient (α) is approximately 0.5 [230, 231], the value of n_α is estimated to be 1, indicating that the one electron transfer process may be the rate-determining step for hydrazine oxidation on Cu-GP. Additionally, i_p varies linearly with $v^{1/2}$, according to the equation: $i_p = 1.181 + 42.962\ v^{1/2}$ ($r^2 = 0.998$, i_p : mA/cm, v : V/s), suggesting a typical diffusion-controlled process according to the equation, $i_p = 0.4958 \times 10^{-3} nF^{3/2}(RT)^{-1/2}(\alpha n)^{1/2}ACD^{1/2}v^{1/2}$ [232], where A stands for electrode surface area.

The diffusion coefficient (D) of hydrazine is obtained from chronocoulometry measurements according to the integrated Cottrell equation, $Q = (2nFAD^{1/2}Ct^{1/2})/\pi^{1/2} + Q_{dl} + nFA\Gamma_0$, where C is the bulk concentration of hydrazine (**Figure 3.7**B) [233]. After subtracting the background charge, plotting Q against $t^{1/2}$ yields a straight line: $Q = -1.768 + 20.157\ t^{1/2}$ ($r^2 = 0.999$, Q : mC/cm^2, t : s). We calculated D of hydrazine is 2.1×10^{-5} cm^2/s, in agreement with the values in literatures [217]. Based on the value of D, the total number of electrons (n) involved in hydrazine oxidation is then calculated to be

4 from the relationship of i_p and $v^{1/2}$. According to the previous reports [234], we proposed the following mechanism for the oxidation of hydrazine at Cu-GP.

$N_2H_4 + OH^- \rightarrow N_2H_3 + H_2O + e^-$ (slow)

$N_2H_3 + 3OH^- \rightarrow N_2 + 3H_2O + 3e^-$ (fast)

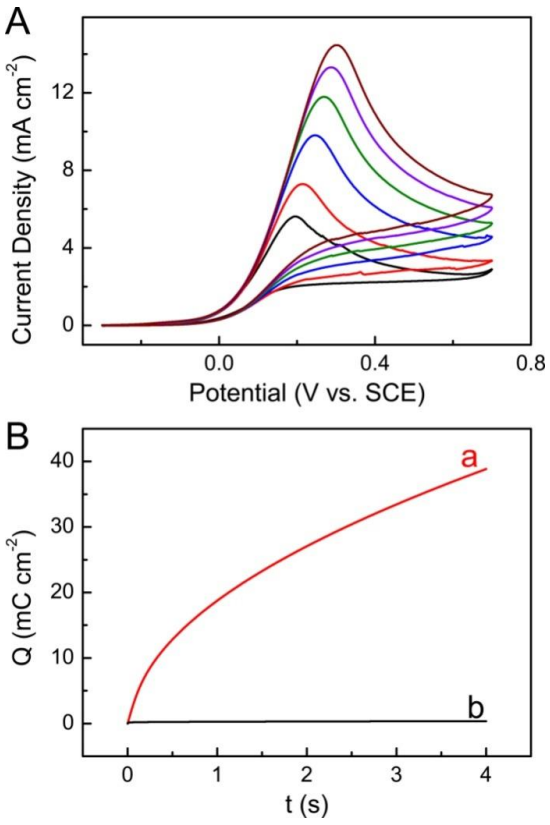

Figure 3.7 (A) CVs of Cu-GP in 0.1 M KOH containing 10 mM hydrazine at a scan rate from 10 to 100 mV/s (from bottom to top); (B) Chronocoulometric response of Cu-GP in 0.1 M KOH solutions containing 10.0 (a) and 0.0 mM (b) hydrazine.

The overall electro-oxidation of hydrazine can be expressed as $N_2H_4 + 4OH^- \rightarrow N_2 + 4H_2O + 4e^-$, with the final products of nitrogen and water. Thus, Cu-GP should not suffer from poisoning effect of oxidation products. The high stability of the nitrogen molecules also help to explain why the overall reaction

is totally irreversible as observed earlier in the CVs, which show no cathodic peak for hydrazine oxidation on Cu-GP.

Catalyst stability is crucial for the long-term operation of fuel cells. The stability of the modified electrodes is first investigated by chronoamperometry under the near-peak potentials. The result shows that the Cu-GP possesses a higher current density than GP and the current density remains steady for continuous reaction of 3000 s. The stability of the flexible Cu-GP electrode is also evaluated by monitoring the change of current density in successive detections of 10 mM hydrazine using one electrode. Agglomeration or migration of electrocatalysts on carbon support is a vital factor leading to their inferior stability and decreased activity [235]. In our approach, Cu nanocubes were directly grown on GP by electrodeposition, a robust and intimate contact is expected to form between Cu nanocubes and GP, efficiently preventing the agglomeration and enhancing the stability of the electrocatalysts. In addition, the in-situ formed Cu hydroxide/oxide constitutes a stable passivating layer and prevents Cu nanocubes from further corrosion [236]. Cu-GP also showed excellent stability for hydrazine oxidation, with 95.3% of initial peak current density retained after 200 CV cycles. And nearly no morphological and composition changes of Cu-GP were observed after 200 cycles.

4. Incorporation of CNTs and Mn_3O_4 nanoparticles into graphene paper for asymmetric supercapacitors

4.1 Introduction

Flexible energy storage devices that can function under considerable physical deformation have attracted increasing attention for portable electronics, paper-like personal gadgets, and miniature biomedical devices [138, 237, 238]. The development of supercapacitors using polymer gel electrolytes represents a promising strategy toward safe, flexible, light-weight, and all-solid-state energy storage devices [239-244]. In particular, asymmetric supercapacitors can enlarge the cell voltage beyond the thermodynamic limit of 1.2 V in aqueous electrolytes and thus significantly improve the energy density [204, 245-247]. The design of flexible asymmetric supercapacitors necessitates the advancement of free-standing paper-like electrodes, which can significantly simplify cell packing by eliminating inactive ingredients such as binders and current collectors with improved overall performance when total mass of device is taken into account [248-250].

Carbon materials as negative electrodes are typically coupled with transition metal oxide as positive electrodes to fabricate asymmetric supercapacitors because of their complementary working potential windows [251-253]. Different challenges are currently present for these two types of electrode materials when used in flexible asymmetric supercapacitors. Among the diverse types of carbon materials, graphene hold great promise in

supercapacitor applications because of the unprecedented combination of large surface area, superior electrical conductivity, and flexibility [85, 207, 254-256]. However, the strong van der Waals interaction drives restacking and aggregation of the sheets when forming free-standing paper electrodes, leading to greatly reduced surface areas [91, 208]. On the other hand, transition metal oxide, especially manganese oxide (*i.e.* MnO_2 and Mn_3O_4) [257-259], although exhibiting high energy density, have shown limited power density due to their poor electrical conductivity. In addition, it is also challenging to process transition metal oxide into flexible electrodes without adding inactive supporting materials. In response to these significant challenges, innovative graphene structures have been developed to minimize the restacking-induced surface area loss, such as holey graphene [137, 260], curved and crumpled graphene [146, 261], and 3D interconnected graphene networks [141, 262]. The morphology of graphene sheets may have a great influence on the performance of the electrode. For example, compared with the flat or wrinkle graphene sheets, the crumpled graphene exhibits better rate capability [261]. Great efforts have also been devoted to structurally integrate transition metal oxide with conductive carbon substrates, leading to hybrid electrodes with improved electrical conductivity [123, 263, 264]. Nevertheless, limited success has been achieved in producing flexible asymmetric supercapacitors with free-standing electrodes featuring optimal electrochemical properties and mechanical strength [265, 266].

In this chapter, all-solid-state asymmetric supercapacitors were constructed based on polymer gel electrolytes and free-standing paper electrodes with carbon nanotubes (CNTs) and Mn_3O_4 nanoparticles structurally intercalated

between the graphene layers (**Figure 4.1**) [267]. Taking the advantage of the colloidal nature of graphene, CNTs and Mn_3O_4 nanoparticles, our results have shown that multi-layered structures of the two paper electrodes were readily formed in the flow-directed self-assembly process, and effectively addressed the abovementioned problems associated with graphene-based negative electrodes and transition metal oxide-derived positive electrodes. The integration of free-standing paper electrodes with polymer gel electrolytes led to flexible asymmetric supercapacitors exhibiting concurrent high energy density and power density, remarkable rate capability, excellent cycling stability, and especially distinguished mechanical flexibility.

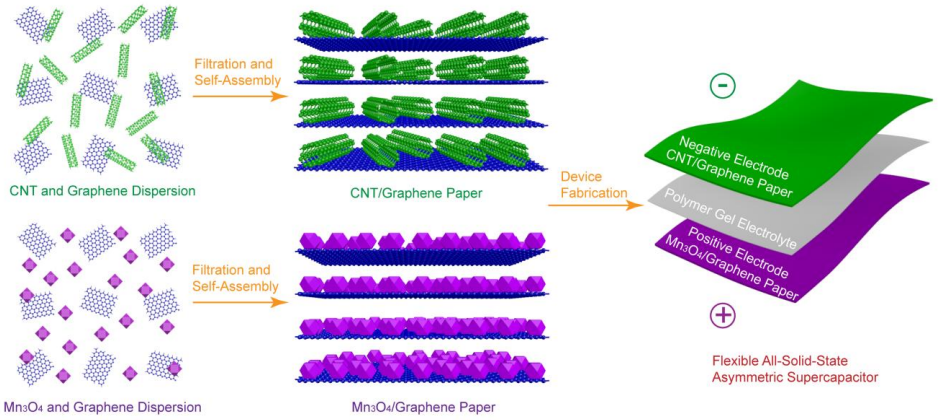

Figure 4.1 Illustration of the fabrication process for flexible asymmetric supercapacitors with polymer gel electrolyte and free-standing CNTG and MG paper electrodes [267].

4.2 Experimental section

Preparation of Samples. CNTs were purified and functionalized by reflux in concentrated HNO_3 for 6 h to introduce carboxylic groups [268]. Mn_3O_4 nanoparticles were synthesized by reacting NaOH (0.25 M, 60 mL) with $Mn(CH_3COO)_2$ $4H_2O$ (0.08 M, 90 mL) containing polyethylene glycol (30 mg)

to achieve precipitates and keep stirring for 3 h [269]. Free-standing CNT/rGO (CNTG) and Mn_3O_4 nanoparticles/rGO (MG) papers were prepared by filtrating the mixtures of rGO with CNTs or Mn_3O_4 nanoparticles through cellulose acetate membrane filters.

Materials Characterization. Zeta potentials of rGO, CNTs and Mn_3O_4 nanoparticles suspensions were measured at room temperature on ZetaPALS Zeta Potential Analyzer (Brookhaven Instruments Corporation). The tensile behaviors of rGO paper based samples were tested on an Instron Microforce Tester with a loading rate of 0.05 mm/min. Quantachrome Autosorb 6B system was used to characterize the specific surface areas and pore structures of the electrode materials using nitrogen sorption under 77.4 K, and according to BET and BJH methods.

Electrochemical Measurements. CNTG, MG and rGO papers were cut into pieces and directly used as electrodes to fabricate symmetric or asymmetric supercapacitors. Potassium polyacrylate (PAAK)/KCl gel electrolyte was prepared by adding 1.0 g PAAK into 10 mL KCl solution (1.0 M) [270]. Two strips of the paper electrodes (~1.0 mg) were immersed into the PAAK/KCl solution for 30 min. After evaporation of excess water, the two paper electrodes were assembled together under press to fabricate all-solid-state supercapacitors. The specific capacitance (C_t) of supercapacitor cells was calculated from the equation of $C_t = I\Delta t/m\Delta V$, where I is the discharging current, Δt is the discharging time, m is the total mass of active materials in two electrodes, and ΔV is the voltage drop upon discharge (excluding IR drop). In symmetric supercapacitors, the specific capacitance (C_{sc}) of the electrodes (CNTG or MG) was calculated according to $C_{sc} = 4C_t$. The energy density (E) and power

density (P) of were calculated following the equations of $E = 1/2C_t\Delta V^2$ and $P = E/\Delta t$, respectively [271-273].

4.3 Results and discussion

4.3.1 Negative electrodes

Hydrothermal reduction was employed to prepare reduced graphene oxide (rGO) [49, 212]. Compared with GO, the thickness of rGO decreases to about 0.8 nm (**Figure 4.2**A and B), matching well with that of single layered rGO reported previously [274]. And rGO has a higher carbon to oxygen ratio (8.0) than GO (2.0) (**Figure 4.2**C and D), with improved electrical conductivity. CNTs (diameter of about 2.0 nm) were purified and functionalized by reflux in concentrated HNO_3 to introduce carboxylic groups [268]. Resulting from the deprotonation of carboxylic acid groups [25], both rGO and CNTs are negatively charged with zeta potentials of -57 and -39 mV, and can form homogeneous dispersions after mild sonication of their mixtures.

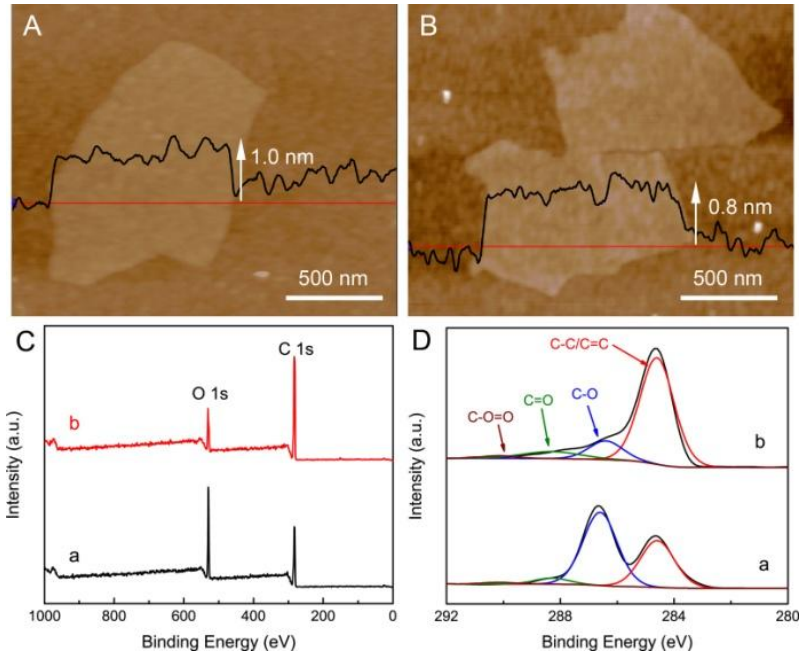

Figure 4.2 AFM images of (A) GO and (B) rGO spin-coated on silicon wafers. (C) XPS survey spectra for GO (a) and rGO (b). (D) C 1s XPS spectra of GO (a) and rGO (b).

Free-standing and flexible CNT/rGO (CNTG) papers with CNTs mass ratio of 20% (CNTG-20) and 40% (CNTG-40) were successfully prepared after filtration of their mixtures through cellulose acetate membranes (**Figure 4.3**A and B). In the hybrid CNTG papers, CNTs are uniformly incorporated between rGO sheets to form sandwich structures (**Figure 4.3**D, E and F), and tend to assemble into bundles with diameter of about 20 nm after filtration and drying. The specific surface areas of CNTG-20 and CNTG-40 were 130.7 and 197.6 m^2/g, with their pore size centered at around 3.0 nm. In contrast, rGO paper exhibits compact layered structures (**Figure 4.3**C), with surface area of 72.5 m^2/g. Apparently, incorporation of CNTs into CNTG can minimize the restacking and aggregation of rGO sheets. And as a result, more electrolyte-accessible surface areas become available, which is expected to facilitate diffusion of electrolyte ions into inner regions of electrodes [75, 275-277]. Interestingly, the tensile strengths of CNTG-20 and CNTG-40 increased to 68.2 and 46.7 MPa relative to that of the pristine rGO paper (41.7 MPa). We reason that CNTs can bridge rGO sheets together through strong π-π interactions between CNTs and rGO sheets, and thus reinforce the mechanical strength of CNTG papers [278].

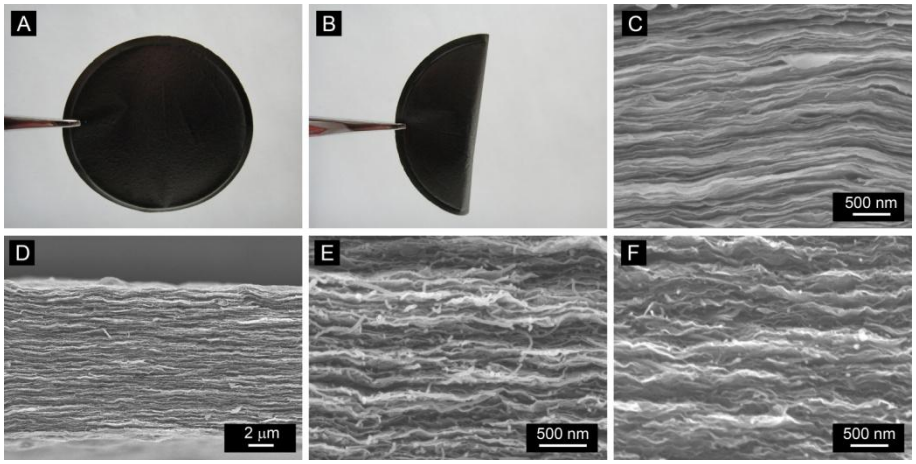

Figure 4.3 (A) Photograph of CNTG-40 paper with a diameter of 4 cm. (B) Photograph shows the free-standing CNTG-40 paper is flexible enough to be fold up. (C) Cross-section SEM images of (C) rGO paper, (D and E) CNTG-40 paper with low and high magnifications, and (F) CNTG-20 paper.

The free-standing rGO and CNTG papers were directly used as electrodes to fabricate all-solid-state symmetric supercapacitors with the polymer gel electrolyte of PAAK/KCl. The nearly rectangular cyclic voltammetry (CV) curves (**Figure 4.4**A) and the linear charge/discharge profiles (**Figure 4.4**B and C) are the typical characteristics of electric double-layer capacitors. rGO paper exhibits inferior performance (99.7 F/g at 0.5 A/g) compared with rGO powers (~ 200 F/g) reported previously [58, 279]. We reason that, in the pristine rGO paper, the strong π-π interactions between the basal planes lead to the restacking and regression of graphene sheets and therefore induce the significant loss of surface areas, which may have a great influence on the performance of the electrodes [261]. After the incorporation of CNTs into rGO paper, the specific capacitances (C_{sc}) of CNTG-40 and CNTG-20 were increased to be 302.9 and 212.9 F/g, respectively. Impressively, compared with rGO paper, CNTG papers can also retain the superior performance well even at high current densities. Specifically, the specific capacitance of CNTG-40 can

reach 220.8 F/g at 10 A/g, while the value of rGO paper dramatically decreased to 45.3 F/g (**Figure 4.4**D). This higher rate capability of CNTG paper than rGO paper further confirms the introduction of CNTs between rGO layers improves the diffusion of electrolyte ions into the inner region of paper electrodes.

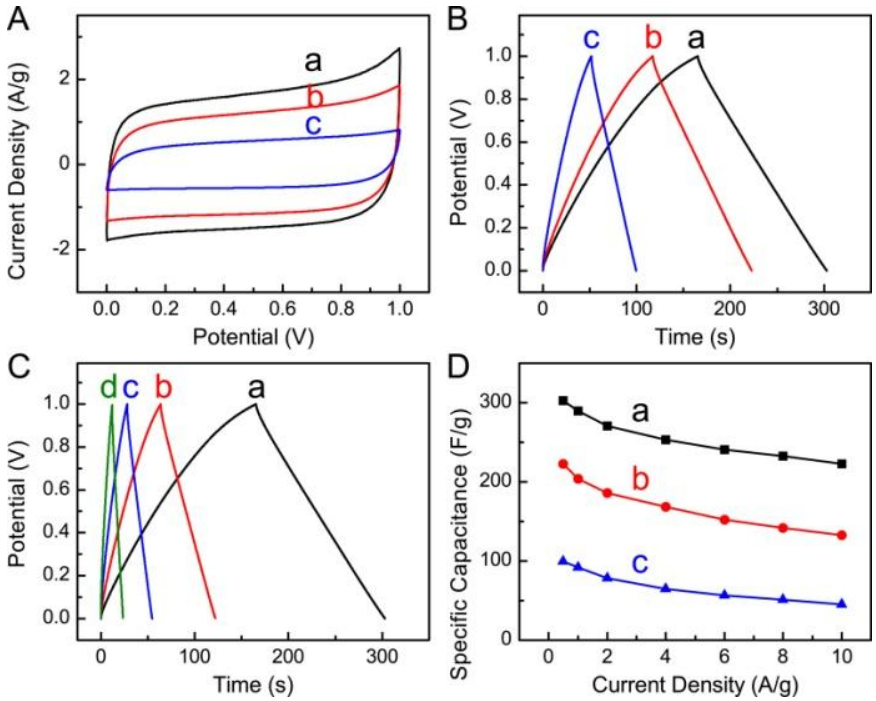

Figure 4.4 (A) Cyclic voltammograms of CNTG-40 (a), CNTG-20 (b), and rGO (c) papers at a scan rate of 20 mV/s. (B) Charge/discharge curves of CNTG-40 (a), CNTG-20 (b), and rGO (c) papers at a current density of 0.5 A/g. (C) Charge/discharge curves of CNTG-40 paper at current densities of 0.5 (a), 1 (b), 2 (c), and 4 (d) A/g. (D) Specific capacitance of CNTG-40 (a), CNTG-20 (b), and rGO (c) papers as a function of discharge current densities.

4.3.2 Positive electrodes

Mn_3O_4 nanoparticles, exhibiting octahedral morphology with particle size of 50-100 nm, were synthesized by reacting $Mn(CH_3COO)_2 \cdot 4H_2O$ with NaOH (**Figure 4.5**A) [269]. All the diffraction peaks in XRD pattern can be indexed to the tetragonal structure of Mn_3O_4. The pH_{pzc} (point of zero charge) of manganese oxide is about 2.25 [280], therefore the prepared Mn_3O_4

nanoparticles have negatively charged surfaces with zeta-potential of -29 mV in neutral solutions, and can form homogenous dispersions with negatively charged rGO (**Figure 4.5**B). Mn_3O_4 nanoparticle/rGO (MG) papers with Mn_3O_4 mass ratio of 25% (MG-25) and 50% (MG-50) were successfully prepared by filtration of their mixture. Although a large amount of Mn_3O_4 nanoparticles were intercalated into rGO papers, the free-standing MG papers are still highly flexible (**Figure 4.5**C), and feature a multi-layered structure throughout the entire cross-section, with Mn_3O_4 nanoparticles uniformly distributed between rGO sheets (**Figure 4.5**D, E, and F). Such a sandwich structure is beneficial to buffer the volume changes of Mn_3O_4 nanoparticles during continuous charge/discharge process. The incorporation of Mn_3O_4 nanoparticles can also minimize the restacking of rGO sheets, and consequently, the specific surface areas of MG-25 and MG-50 papers increased to 104.8 and 138.9 m^2/g, with their pore size distributions in the range of 2.0 to 8.0 nm. Importantly, MG papers possess excellent mechanical stability even after loading large amounts of Mn_3O_4 nanoparticles. The tensile strengths of MG-50 and MG-25 papers are still as high as 24.0 and 31.9 MPa.

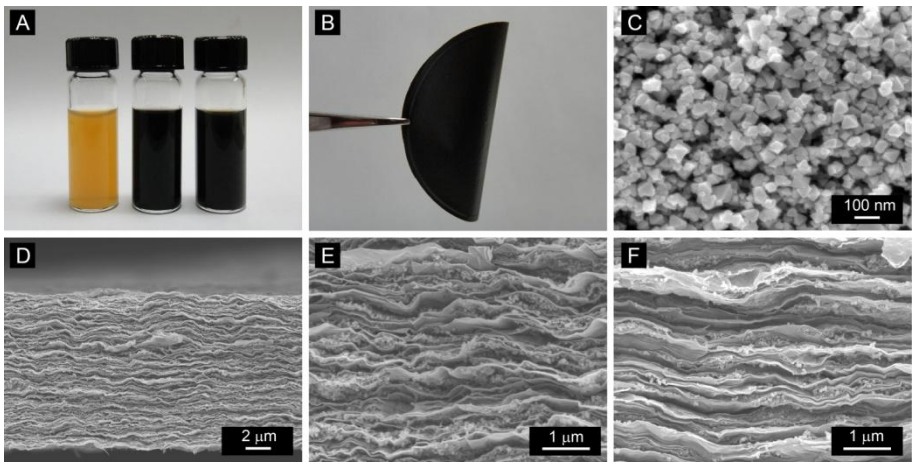

Figure 4.5 (A) Photographs of aqueous dispersions of Mn_3O_4 nanoparticles, rGO, and their mixture with a mass ratio of 1:1 (from left to right). (B)

Photograph of MG-50 paper with a diameter of 4 cm and flexible enough to be fold up. (C) SEM image of Mn_3O_4 nanoparticles. Cross-section SEM images of MG-50 paper with (D) low and (E) high magnifications, and (F) MG-25 paper.

All-solid-state symmetric supercapacitor of MG//MG, fabricated by using the free-standing MG paper electrodes and the polymer gel electrolyte of PAAK/KCl, exhibits ideal capacitive behavior as evidenced by the nearly rectangular CV curves (**Figure 4.6**A) and the linear galvanostatic charge/discharge profiles (**Figure 4.6**B and C). The specific capacitances (C_{sc}) of MG-50 and MG-25 increased to 321.1 and 252.7 F/g at 0.5 A/g. The layered rGO sheets in MG papers can provide efficient charge transport channels with improved electrical conductivity and utilization efficiency of Mn_3O_4 nanoparticles [281, 282], leading to the paper electrodes with remarkable rate capability. Especially, when the current density increased to 10 A/g, the specific capacitance of MG-50 still can reach 243.6 F/g (**Figure 4.6**D).

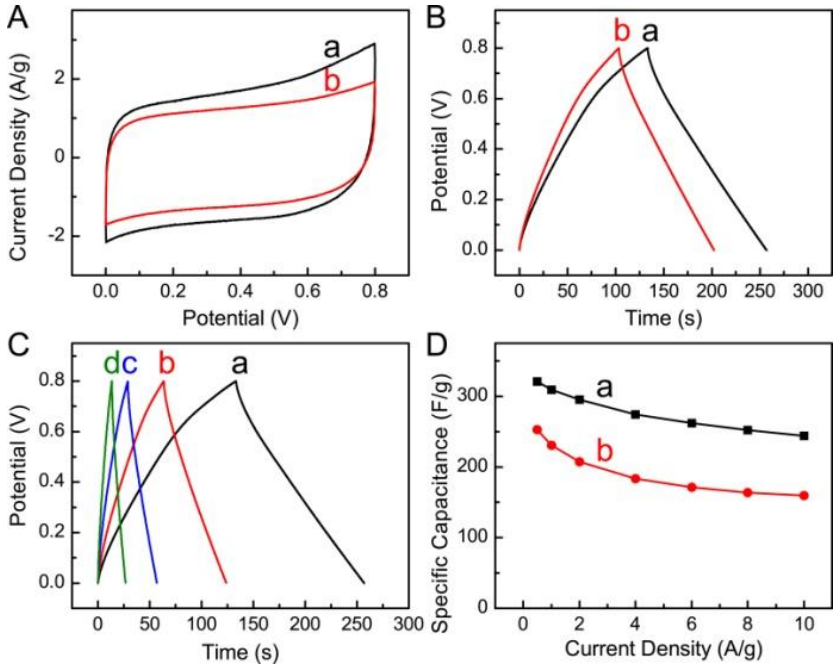

Figure 4.6 (A) Cyclic voltammograms of MG-50 (a) and MG-25 (b) papers at scan rate of 20 mV/s. (B) Charge/discharge curves of MG-50 (a) and MG-25

papers (b) at a current density of 0.5 A/g. (C) Charge/discharge curves of MG-50 paper at current densities of 0.5 (a), 1 (b), 2 (c), and 4 (d) A/g. (D) Specific capacitance of MG-50 (a) and MG-25 (b) papers as a function of discharge current densities.

4.3.3 All-solid state asymmetric supercapacitor

Taking advantage of the different stable potential windows of CNTG and MG paper electrodes (**Figure 4.7**A) [283], we fabricated asymmetric supercapacitor of CNTG-40//MG-50 with the mass ratio of the two electrodes fixed to 0.85, which is based on their specific capacitances and working electrochemical windows, in order to achieve a charge balance between the negative and positive electrodes [284]. As expected, the cell voltage of the asymmetric supercapacitor can research up to 1.8 V in the polymer gel electrolyte of PAAK/KCl (**Figure 4.7**B). In the whole potential range, the asymmetric supercapacitor exhibits excellent capacitive performance as revealed by the triangle shape of charge/discharge curves (**Figure 4.7**C). The specific capacitance (C_t) of CNTG-40//MG-50 can reach 72.6 F/g at 0.5 A/g, and 50.8 F/g at 10 A/g (**Figure 4.7**D). The asymmetric supercapacitor of CNTG-40//MG-50 possesses an energy density of 32.7 Wh/kg, nearly 3 or 4 times higher than the symmetric supercapacitors of CNTG-40//CNTG-40 (10.5 Wh/kg) and MG-50//MG-50 (7.1 Wh/kg) (**Figure 4.7**E). More importantly, when the power density increases to 9.0 kW/kg, the energy density of CNTG-40//MG-50 is still as high as 22.9 Wh/kg, suggesting that the asymmetric supercapacitor can provide a high energy density with a high power density concurrently. The asymmetric supercapacitor of CNTG-40//MG-50 also showed remarkable cycling stability and retained 86.0% of its initial capacitance after 10000 cycles (**Figure 4.7**F).

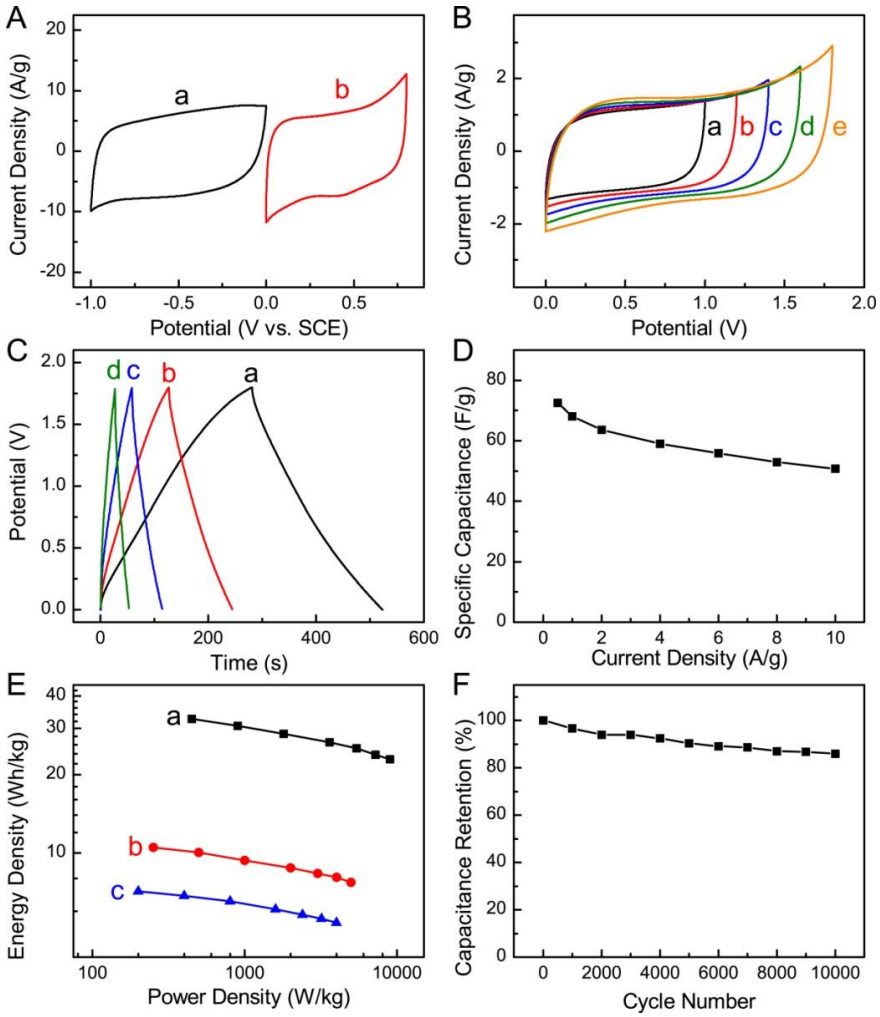

Figure 4.7 (A) Cyclic voltammograms of CNTG-40 (a) and MG-50 (b) in three-electrode systems. (B) Cyclic voltammograms of CNTG-40//MG-50 at cell voltages of 1.0 (a), 1.2 (b), 1.4 (c), 1.6 (d) and 1.8 (e) V. (C) Charge/discharge curves CNTG-40//MG-50 at current densities of 0.5 (a), 1 (b), 2 (c), and 4 (d) A/g. (D) Specific capacitance of CNTG-40//MG-50 as a function of current densities. (E) Ragone plots of CNTG-40//MG-50 (a), CNTG-40//CNTG-40 (b), and MG-50//MG-50 (c). (F) Cycling behavior of CNTG-40//MG-50 with a cell voltage of 1.8 V and scan rate of 50 mV/s.

We have also found that two asymmetric supercapacitors of CNTG-40//MG-50 connected in series can light a green light-emitting-diode, demonstrating its practical applications (**Figure 4.8**A). The maximum energy density (32.7 Wh/kg) of CNTG-40//MG-50 at the current density of 0.5 A/g is

higher or comparable to the manganese oxide based asymmetric supercapacitors in aqueous electrolytes reported previously, including activated carbon//mesoporous MnO_2 (10.4 Wh/kg at 0.3 A/g) [285], activated carbon//$NaMnO_2$ (19.5 Wh/kg at 0.04 A/g) [286], activated carbon//MnO_2 (17.3 Wh/kg at 0.55 A/g) [287], CNT//graphene-MnO_2 (12.5 Wh/kg at 0.45 A/g) [288], and graphene//graphene-MnO_2 (21.27 Wh/kg at 0.223 A/g) [289]. Moreover, different from the supercapacitors packed with aqueous or organic electrolytes, the all-solid-state asymmetric supercapacitor of CNTG-40//MG-50 using the polymer gel electrolytes of PAAK/KCl exhibits excellent flexibility (**Figure 4.8**B). In addition, galvanostatic charge/discharge curves reveal that repeated bending and twisting had nearly no effect on the capacitive performance of the device (**Figure 4.8**C and D).

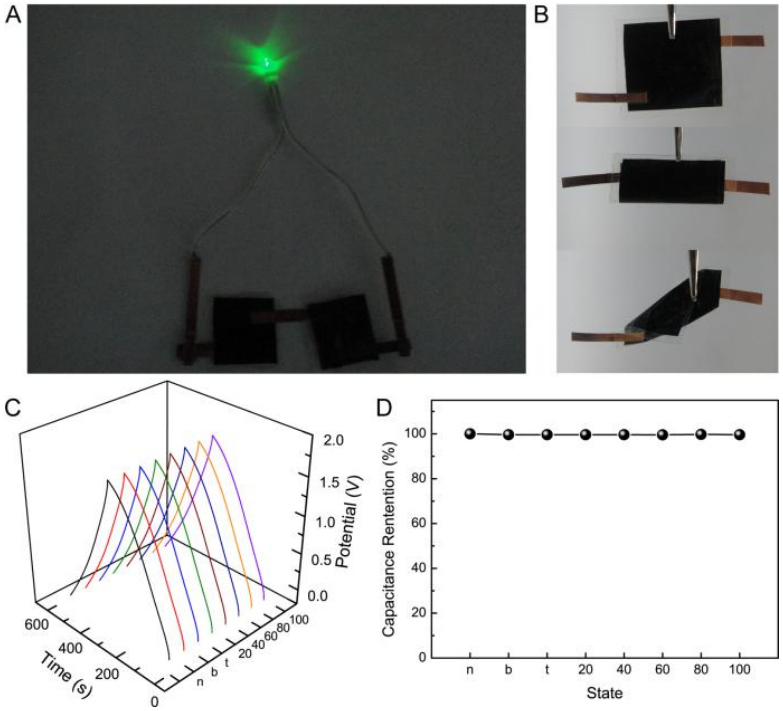

Figure 4.8 (A) A green LED lighted by two asymmetric supercapacitors of CNTG-40//MG-50 connected in series. (B) Photographs of the asymmetric supercapacitor at normal, bending, and twisting states (from top to bottom). (C)

Charge/discharge curves, and (D) specific capacitance retention ratio of the asymmetric supercapacitor at normal (n), bending (b), twisting (t) states, and after a number of repeated bending.

5. Graphene hydrogel and MnO_2 nanostructures for asymmetric supercapacitors

5.1 Introduction

Supercapacitors represent an emerging type of energy storage devices with increasing attentions arising from their important features including remarkable power density, rapid charging discharging rate, and outstanding cycle stability [243, 253, 290]. Nevertheless, the low energy density (normally less than 10 Wh/kg) of commercially available supercapacitors has imposed significant challenges in employing them as power sources to compete with batteries [252]. Recently, concentrated efforts have been made to tackle this problem by developing nanostructured electrode materials with improved specific capacitance and increasing the operating voltage of a supercapacitor [291-293]. In particular, two strategies are commonly explored for the design of high-voltage supercapacitors, i.e., replacing aqueous electrolytes with organic electrolytes [7, 140] or ionic liquids [294, 295] having wider potential windows and developing hybrid (asymmetric) supercapacitors with both capacitive electrode as power source and Faradic electrode as energy source [296-298]. However, non-aqueous electrolytes typically suffer from limited ionic conductivity and also raise safety concerns about the potential environmental impact in case of leakage. The construction of asymmetric supercapacitors is an effective approach to extend the cell potential window beyond the thermodynamic limit (~1.2 V) in aqueous electrolytes and thus significantly improve the energy density [245, 246, 251, 299]. The combination of appropriate electrode materials with complementary electrochemical potentials

in the same electrolyte is the key to achieve high energy density and power density simultaneously [265, 288, 300].

In this chapter, we reported the design of asymmetric supercapacitor employing graphene hydrogel (GH) with 3D interconnected pores and a hierarchical composite of vertically-aligned MnO_2 nanoplates on nickel foam (MnO_2-NF) as negative and positive electrodes respectively (**Figure 5.1**) [273]. Carbon materials, exhibiting complementary electrochemical windows to various pseudo-capacitive materials, are usually employed as negative electrodes in asymmetric supercapacitors [272, 301]. Graphene consisting of hexagonally-bonded sp^2 carbon atoms is extensively explored for supercapacitors arising from its high specific surface area, remarkable electrical conductivity and excellent chemical stability [279, 302]. However, the aggregation and restacking of graphene sheets during processing leads to significantly reduced surface areas and therefore becomes a serious obstacle to take the full advantage of the structural characteristics of graphene [146]. Our results have shown that assembling graphene sheets into GH with a 3D network structure in the chemical reduction process of graphene oxide (GO) can effectively prevent the aggregation of graphene sheets. Consequently, GH as electrode materials provides large active surface areas and facilitated electrolyte ion transportation and exhibited improved capacitance and remarkable rate capability. One interesting finding is that an eco-friendly reagent of L-glutathione allows for producing robust GH from GO dispersion under mild conditions, offering greater flexibility than the time-consuming hydrothermal method previously reported [105, 106].

MnO_2 with pseudocapacitance is highly attractive positive electrode materials, benefiting from its low cost, abundance and remarkable electrochemical behavior in aqueous electrolytes [248, 303, 304]. Varieties of wet-chemical and electrochemical methods have been developed to prepare nanostructured MnO_2 [305]. Structural parameters, such as crystal type, morphology and porosity, are the vital factors determining the electrochemical performance of MnO_2-based electrodes [306]. In this work, a hierarchical composite of MnO_2-NF was prepared by electrodeposition of MnO_2 nanoplates on highly-conductive porous nickel foam through cathodic electrodeposition and directly used as electrodes for supercapacitors without further processing. Importantly, the porous structure of nickel foam allows a higher mass loading of active materials per area, facilitates the electrolyte ion transportation and reaction with the active materials, and eventually leads to improved utilization efficiency of active materials. Compared with anodic deposition in which a positive potential is applied to oxidize starting Mn^{2+} into Mn^{4+} and deposit as MnO_2 [307, 308], cathodic deposition of MnO_2 can prevent the oxidation and dissolution of metal current collectors with low-cost [309, 310]. Moreover, a robust contact endowed by electrodeposition is formed between MnO_2 nanostructures and the highly conductive nickel foam, which can cope with the problems of poor electrical conductivity and rate capability of MnO_2 when used as electrode materials. Collectively, taking advantages of GH with 3D interconnected pores, vertically-aligned MnO_2 nanoplates with sufficient free spaces, and robust contact between MnO_2 and nickel foam, we have found that the fabricated asymmetric supercapacitor of GH//MnO_2-NF can be cycled reversibly in a wide potential window of 0-2.0 V and exhibits a much higher

energy density of 23.2 Wh/kg than that of the symmetric supercapacitors of GH//GH (5.5 Wh/kg) and MnO_2-NF//MnO_2-NF (6.7 Wh/kg) at current density of 1 A/g. Furthermore, the asymmetric supercapacitor displays remarkable cycling stability with capacitance retention of 83.4% after 5000 continuous charge/discharge cycles.

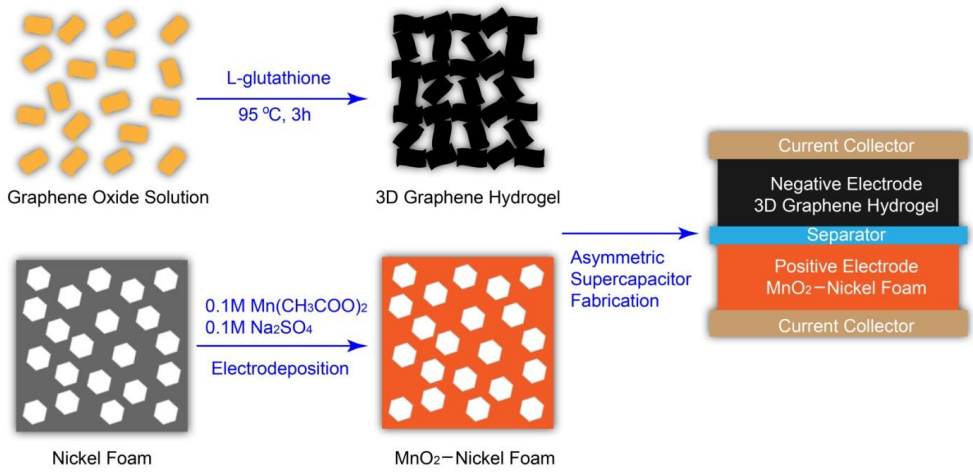

Figure 5.1 The fabrication process of the asymmetric supercapacitor with GH as the negative electrode and MnO_2-NF as the positive electrode [273].

5.2 Experimental section

Preparation of Samples. GH was prepared by the following procedure using L-glutathione as the reducing agent. Briefly, GO aqueous dispersion (2.0 mg/mL) was loaded in a glass vial. Then, L-glutathione was added to get a concentration of 4.0 mg/mL. After stirring for 60 min to dissolve the L-glutathione, the as-prepared dispersion was heated at 95 ℃ for 3 h without any disturbance to produce GH. The dispersion of reduced GO (RGO) was also prepared using L-glutathione as a reducing agent at the same temperature under continuous stirring. After the chemical reduction, the excess L-glutathione was removed by dialysis.

MnO_2-NF was prepared by electrodeposition of MnO_2 on nickel foam (1 cm × 1 cm) with platinum wire and saturated calomel electrode (SCE) as the counter and reference electrodes, respectively. Cathodic electrodeposition of MnO_2 nanoplate arrays was carried out in aqueous solution containing 0.1 M manganese acetate and 0.1 M sodium sulfate according to a method previously reported with some modification [311]. Typically, the deposition was carried out at a constant potential of -1.6 V for different time to control the amount of MnO_2. After deposition, the nickel foam was rinsed in deionized water for several times and then dried at ambient temperature. The accurate weight of electrodeposited MnO_2 was read by a high-precision balance with sensitivity of 0.01 mg (Denver Instrument).

Electrochemical Measurements. The obtained GH can be directly used as electrode to fabricate symmetric supercapacitor of GH//GH. MnO_2-NF was also directly used to fabricate symmetric supercapacitor of MnO_2-NF//MnO_2-NF. To construct the asymmetric supercapacitor of GH//MnO_2-NF, the mass ratio of GH and MnO_2 was estimated to be 1.2 based on their specific capacitances. And each electrode contained about 1.0 mg active material. The two electrodes were assembled in a Swagelok-type cell with a glass-fiber separator. The electrolyte was 0.5 M aqueous Na_2SO_4 solution.

5.3 Results and discussion

5.3.1 Negative electrode materials

Homogenous GO solution, synthesized from graphite powder according to the modified Hummers' method, was deposited on silicon wafer by spin-coating for AFM observation. As shown in **Figure 5.2**A, GO sheets are flat

with a typical thickness of about 1.0 nm, indicating the complete exfoliation of graphite oxide into single-layered GO sheets [158]. L-glutathione, an eco-friendly reducing agent, was selected for the chemical reduction of GO. Because of the capping effect of the oxidation products of L-glutathione, a stable dispersion of graphene was obtained previously when a low concentration (0.1 mg/mL) of GO was reduced with L-glutathione under continuous stirring [38]. In this article, we found that the use of concentrated GO dispersion (2.0 mg/mL) and the elimination of physical disturbance are essential for the self-assembly of graphene sheets into 3D structures of GH in this reaction system. A series of GO and L-glutathione dispersion were reacted at 95 ℃ for different spans of time to investigate the gelation process (**Figure 5.2**B). Before the chemical reduction, GO was well dispersed in water forming a stable dark-brown colloidal suspension. After the addition of L-glutathione, gelation cannot take place if the reaction time was less than 30 min. Further prolonging the reaction time to 60 min, a black cylinder of GH was obtained. After treated for 180 min, the apparent size of the black cylinder decreased, and little change was observed subsequently.

The formation of 3D structured GH is attributed to the partial overlapping or coalescing of flexible reduced GO sheets via different supramolecular interactions, such as hydrogen bonding, electrostatic interaction, coordination and π-π stacking [107, 312]. Reduction degree is also an important factor contributing to formation of GH [106]. As the reduction proceeding, the graphene sheets assembled more tightly leading to GH with 3D interconnected network structures. The well-defined and interconnected 3D network of the resulting GH was revealed by typical SEM images (**Figure 5.2**D and E) of its

freeze-dried sample after reduction of 180 min. A plenty of pores with a wide size distribution are observed, and the solid walls of these pores are composed by randomly cross-linked and inter-twisted graphene sheets. The BET specific surface areas of GH after reduction of 30, 60, and 180 min were measured to be 230.4, 259.8, and 315.2 m^2/g, respectively. Most pores of GH prepared at different time are in the mesoporous range with peaks centered at 2-10 nm. The increase of BET specific surface areas with prolonging the reaction time indicates that the formation of 3D network of GH is an effective approach to prevent the aggregation of graphene sheets. In addition, this unique 3D structure of GH enables the fabrication of self-supported supercapacitor electrodes, which is beneficial for improving the overall energy density of the supercapacitor by avoiding the utilization of conducting additives and polymer binders [313]. For comparison, a common strategy was employed to prepare the dispersion of reduced GO (RGO) using L-glutathione as a reducing agent but under continuous stirring. After filtration and freeze-drying, serious aggregation was observed due to the strong interactions between RGO sheets (**Figure 5.2**F), and the BET specific surface area of RGO is 210.9 m^2/g, significantly smaller than that of GH (315.2 m^2/g).

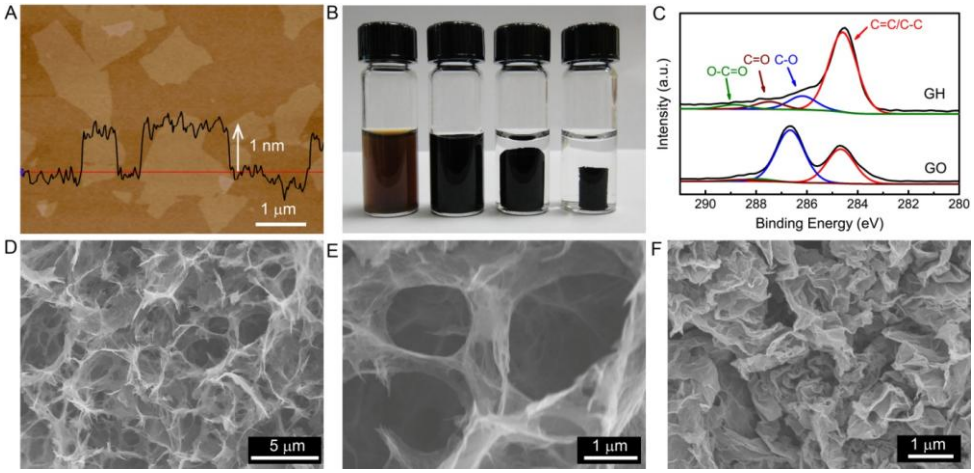

Figure 5.2 (A) AFM images of GO dispersion spin-coated on silicon wafer; (B) Photograph of aqueous mixture of GO and L-glutathione at different reaction time of 0, 30, 60 and 180 min (from left to right); (C) C 1s XPS spectra of GO and GH; (D and E) SEM images of freeze-dried GH with low and high magnification; (F) SEM images of free-dried RGO.

The successful reduction of GO by L-glutathione was confirmed by high resolution XPS spectra of C1s and FT-IR Spectra. The XPS peaks of oxygen functionalities decreased significantly after the chemical reduction for 180 min, revealing that most of oxygen functionalities on GO were removed (**Figure 5.2**C). The mechanism for the reduction of GO by L-glutathione is possibly based on a two-step S_N^2 nucleophilic reaction [314]. The proton released from the oxidation product of thiol group in L-glutathione acts as a nuceophile, has a high binding affinity to oxygen functionalities, including hydroxyl and epoxide groups on GO, leads to the formation of water molecules [40]. Eventually, L-glutathione is oxidized into glutathione disulfide leading to the formation of RGO sheets. In the FT-IR spectra (**Figure 5.3**A), we could not detect the characteristic stretching vibration peaks of C-S bonds in the range of 710-580 cm^{-1} [315]. And no peaks from sulfur are observed in the EDS spectra of GH. These results suggest the excess L-glutathione and glutathione disulfide were successfully removed by dialysis.

The structure of GO and GH was also studied by X-ray diffraction (XRD). According to the XRD patterns (**Figure 5.3**B), GO has a large interlayer distance of 0.85 nm ($2\theta = 10.3°$) because of the presence of hydroxyl, epoxy and carboxyl groups. After chemical reduction for 180 min, a broad peak centered at $2\theta = 24.4°$ corresponding to an interlayer distance of 0.37 nm

emerged, suggesting the poor ordering of graphene sheets along their stacking direction in GH [43]. The change of structure after the reduction process is further reflected in Raman spectra (**Figure 5.3**C). Both of the spectra of GO and GH display the existence of D and G bonds located at 1352 and 1594 cm^{-1}. The bands intensity ratio (I_D/I_G) is 0.8 in GO and increases to 1.2 in GH, demonstrating that the chemical reduction altered the structure of GO and introduced a high quantity of structural defects [35, 316].

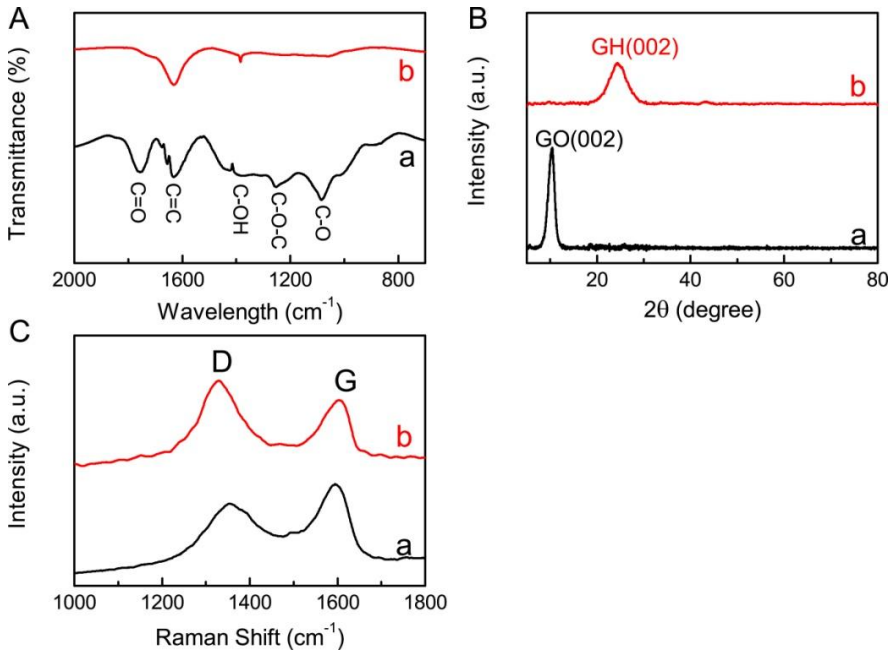

Figure 5.3 (A) FT-IR spectra; (B) XRD patterns; and (B) Rama spectra of GO (a) and GH (b).

The electrical conductivity of GH was measured to be ~2 S/m base on a two-probe method [105]. This remarkable conductivity and its mechanically stable nature enable GH to be directly used as electrodes to fabricate supercapacitors without the need of polymer binder and conducting additives [140]. The performance of the symmetric supercapacitor of GH//GH were tested in aqueous Na_2SO_4 electrolyte. The nearly rectangular CV curves

manifest the ideal capacitive behavior of the supercapacitor (**Figure 5.4**A) [283]. Even at a high scan rate of 100 mV/s, the shapes of CV curves remain undistorted, implying low contact resistance in the supercapacitor. From the slope of galvanostatic charge/discharge curves, we obtained the capacitance of GH is 157.7 F/g at 1 A/g (**Figure 5.4**B). GH can still deliver 92.0 F/g when the current density increases to 10 A/g (**Figure 5.4**C). The high-rate capability is possibly due to the 3D porous structure and improved conductivity of the L-glutathione reduced GH. The aggregated RGO was mixed with carbon black as the conducting agent and PVDF as the binder in a mass ratio of 8:1:1 to fabricate symmetric supercapacitor of RGO//RGO. The aggregation of graphene sheets lead to reduced active sites for electrolyte ions, and consequently, and consequently, in comparison with GH, RGO exhibits a much lower capacitance of 114.5 F/g at 1 A/g (**Figure 5.4**D).

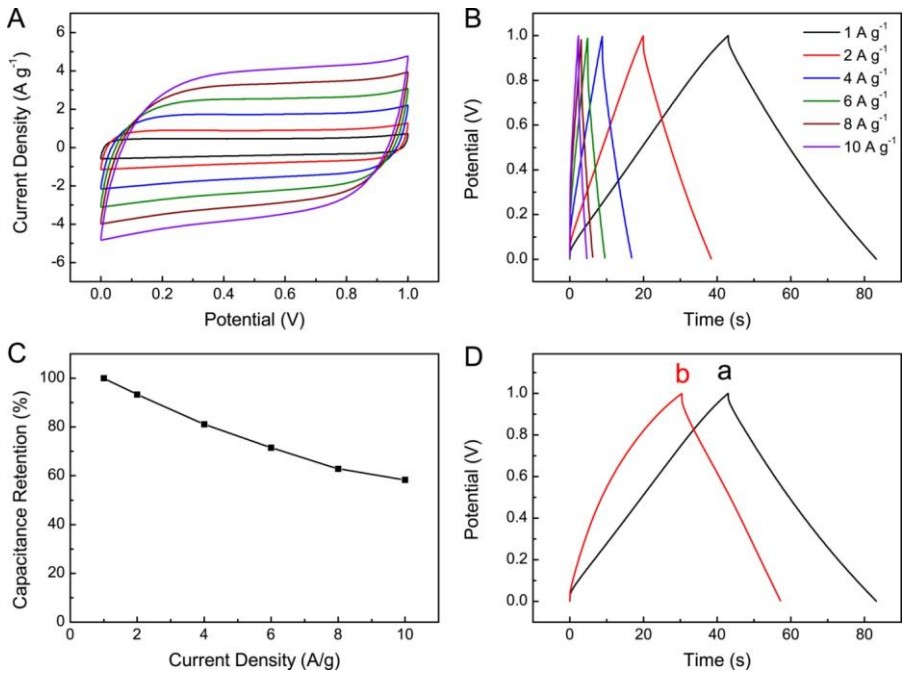

Figure 5.4 Electrochemical performance of the symmetric supercapacitor of GH//GH: (A) Cyclic voltammograms at scan rates from 10 to 100 mV/s (from inner to outer); (B) Charge/discharge curves at current densities from 1 to 10

A/g; (C) Capacitance retention ratio as a function of discharge current densities; (D) Charge/discharge curves of symmetric supercapacitors of GH//GH (a) and RGO//RGO (b) at current density of 1 A/g.

5.3.2 Positive electrode materials

Nickel foam, with excellent electrical conductivity, is featured of cross-linked grids, providing higher porosity and surface area than conventional metal plates (**Figure 5.5**A and B) [317, 318]. After electrodeposition in aqueous manganese acetate solution at -1.6 V for 100 s, the smooth surface of the nickel foam skeleton (**Figure 5.5**C) became decorated with a dark brown thin film of MnO_2. The deposited MnO_2 with nanoplate structure are the uniformly coated on the grid of nickel foam and build up an interconnected network with highly porous structures (**Figure 5.5**D, E and F). The formation of nanoplate structure is probably due to the generation of H_2 bubbles at negative enough potential (-1.6 V), which function as dynamic template for the electrodeposition [319, 320]. Importantly, the hierarchical structure of MnO_2-NF is beneficial for improved electrochemical performance of the active materials. The unique network structure constituted of vertically-aligned MnO_2 nanoplates can also provide necessary free spaces between the individual nanostructures to relax the volume change during continuous charge/discharge reactions.

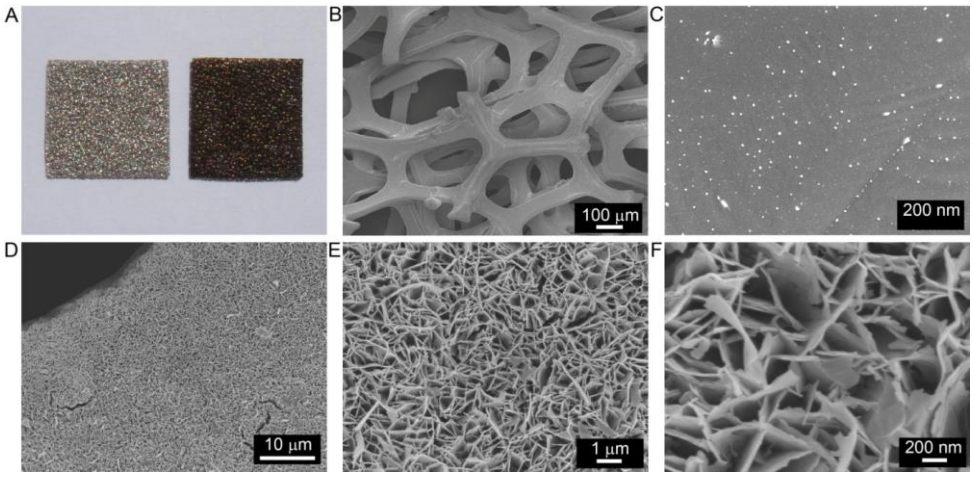

Figure 5.5 (A) Photographs of nickel foam before (left) and after (right) electrodeposition of MnO_2; (B and C) SEM images of bare nickel foam with low and high magnification; (D, E and F) SEM images of MnO_2 nanoplates electrodeposited on nickel foam at -1.6 V for 100 s with different magnifications.

Energy dispersive X-ray spectroscopy (EDS) confirms the presence of the elements of manganese and oxygen in the deposited materials, whereas no other chemical elements, such as sodium and sulfur present in the salt precursors, were detectable (**Figure 5.6**A). There are two XPS peaks for the deposited materials, i.e., Mn $2p_{3/2}$ at 641.9 eV and Mn $2p_{1/2}$ at 653.4 eV, with spin-energy separation of 11.5 eV (**Figure 5.6**B), in accordance with the reported value in MnO_2 [259]. The XRD pattern of MnO_2-NF exhibits several broad peaks with low intensity (except the peaks from the nickel substrate), which can be assigned to ε-MnO_2 (**Figure 5.6**C) [321]. The electrolysis of water and electro-reduction of O_2 at negative potentials result in increased local pH value. Mn^{2+} was first precipitated as $Mn(OH)_2$, and then oxidized into MnO_2 by air [52].

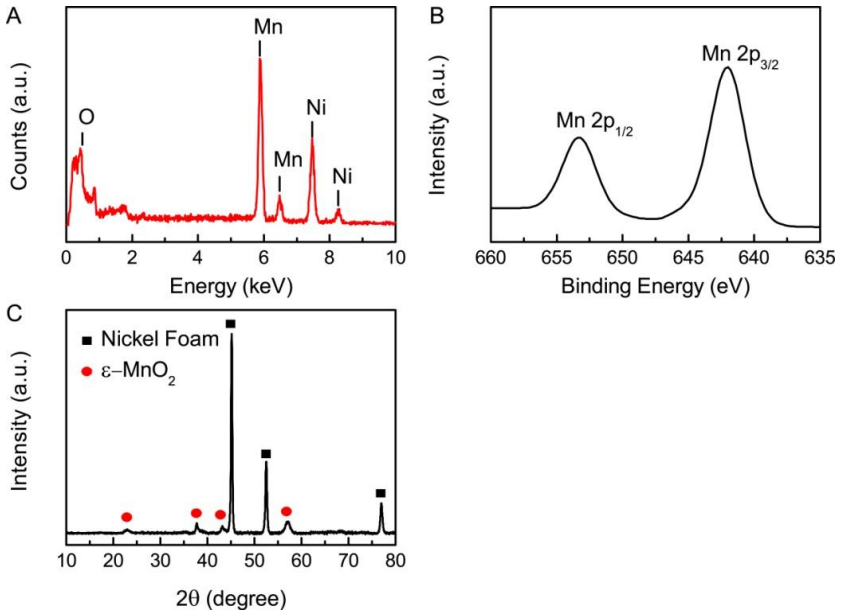

Figure 5.6 (A) EDS spectra of MnO_2-NF; (B) High resolution XPS spectra of MnO_2-NF for Mn $2p_{1/2}$ and Mn $2p_{3/2}$; (C) XRD pattern of MnO_2-NF.

MnO_2-NF can also be directly used to fabricate supercapacitors by eliminating the need of polymer binder and conducting additives. The specific capacitance is dependent on the amount and morphology of MnO_2 on nickel foam. With increasing the electrodeposition time from 50 to 200 s, MnO_2 with multilayer evolved from monolayer nanoplates, the weight of MnO_2 increased from 0.6 to 1.7 mg, and the specific capacitance decreased from 226.8 to 110.8 F/g. The formation of thick nanoplates could reduce the specific surface area of MnO_2 exposed to electrolyte ions and result in the decrease of the specific capacitance. Taking into account of the mass and specific capacitance of MnO_2, the electrodeposition time was fixed at 100 s for further investigations. MnO_2 electrodeposited after 100 s exhibits a large BET surface area (59 m^2/g). **Figure 5.7**A shows the CV and charge/discharge curves of MnO_2-NF//MnO_2-NF in aqueous Na_2SO_4 electrolyte. The typical rectangular shape of all CV curves measured indicates the perfect capacitive behavior of the supercapacitor. The

oxidation of nickel foam can be neglected, because of the absence of the typical oxidation and reduction peaks of nickel oxide in the CV curves [322]. The charge/discharge curves are very symmetrical in the total range of potential (**Figure 5.7**B and C). The specific capacitance of MnO_2 deposited for 100 s is 194.6 F/g at 1 A/g. Resulting from the unique hierarchical structure of MnO_2-NF and the robust contact between MnO_2 nanoplates and nickel foam endowed by electrodeposition method, the supercapacitor possesses superior rate capability. When the current density increased to 10 A/g, the capacitance still reaches 120.0 F/g, about 62 % of that at 1 A/g (**Figure 5.7**D).

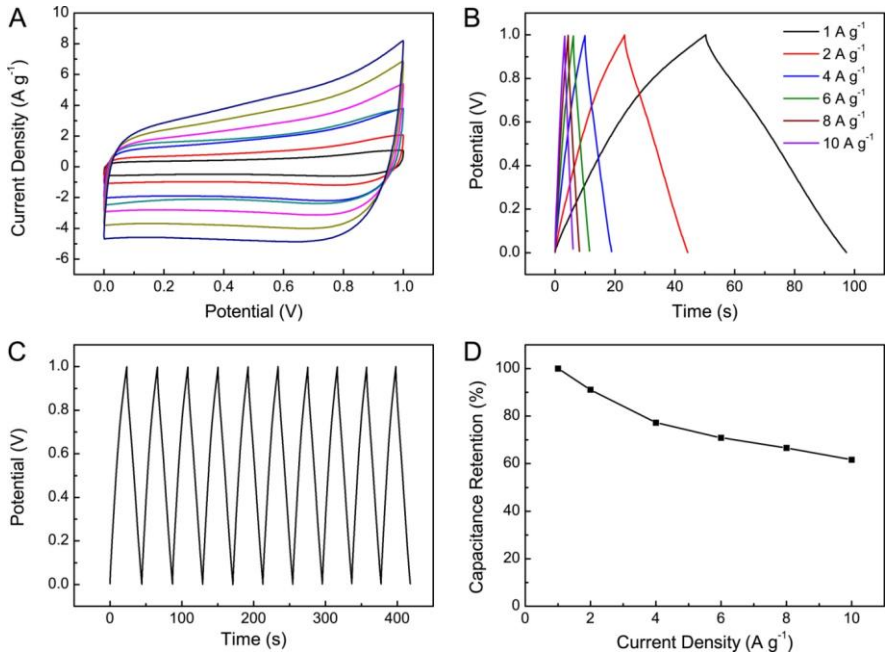

Figure 5.7 Electrochemical performance of the symmetric supercapacitor of MnO_2-NF//MnO_2-NF: (A) Cyclic voltammograms at scan rates from 10 to 100 mV/s (from inner to outer); (B) Charge/discharge curves at current densities from 1 to 10 A/g; (C) Charge/discharge curves at a constant current density of 2 A/g; (D) Capacitance as a function of discharge currents.

5.3.3 Asymmetric hybrid supercapacitor

We then fabricated the asymmetric supercapacitor using MnO_2-NF and GH as the positive and negative electrodes, respectively. Cyclic voltammetry was first used to estimate the electrochemical potential windows of the electrodes (**Figure 5.8**A). GH exhibits the stable potential window between -1.0 and 0 V, while MnO_2-NF between 0 and 1.0 V. The cell voltage will be the sum of the potential windows of GH and MnO_2-NF, and consequently it can be enlarged up to 2.0 V in 0.5 M aqueous Na_2SO_4 solution for the asymmetric supercapacitor of GH//MnO_2-NF [323, 324]. To obtain a 2.0 V operating potential window, it is necessary to balance the charges stored in two electrodes. The stored charges (q) are related with the specific capacitance (C_{sc}), the potential window (ΔV), and the mass (m) of the electrode according to $q = C_{sc} \times \Delta V \times m$ [283]. Therefore, based on the capacitances and the potential windows of the two materials, the mass ratio between GH and MnO_2 of m(GH)/m(MnO_2) = 1.2 was selected in the asymmetric supercapacitor cell. And indeed the fabricated asymmetric supercapacitor of GH//MnO_2-NF exhibits a stable potential window up to 2.0 V (**Figure 5.8**B). The enlarged potential window would give rise to a remarkably enhanced energy density of supercapacitors.

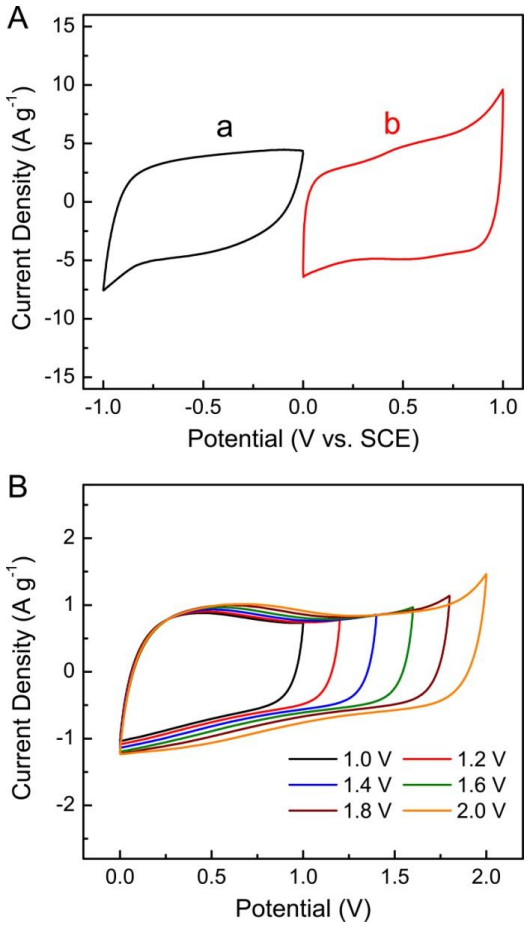

Figure 5.8 (A) Comparative cyclic voltammograms of GH (a) and MnO_2-NF (b) electrodes in a three-electrode cell at a scan rate of 20 mV/s; (B) Cyclic voltammograms of the asymmetric supercapacitor of GH//MnO_2-NF measured at different potential windows at a scan rate of 20 mV/s.

The asymmetric supercapacitor shows relatively rectangular CV curves at scan rates up to 100 mV/s, indicating a good supercapacitor performance and a desirable fast charge/discharge property (**Figure 5.9**A). Charge/discharge measurements were also performed at different current densities in a potential window of 0-2.0 V (**Figure 5.9**B). The symmetric charge/discharge curves and the linear potential-time profile in the whole potential range also demonstrate a remarkable capacitive performance with a rapid *I-V* response of our asymmetric supercapacitor. The capacitance of the asymmetric supercapacitor is calculated

to be 41.7 F/g at 1 A/g, and still reaches 26.8 F/g at 10 A/g (**Figure 5.9**C). We than use Ragone plots, depicting the relationship of power densities (*P*) and energy densities (*E*), to compare the performance of three types of supercapacitors (**Figure 5.9**D). The energy density of GH//MnO_2-NF with a cell voltage of 2.0 V is much higher than that of the symmetric supercapacitors of MnO_2-NF//MnO_2-NF and GH//GH with a cell voltage of 1.0 V at the same power density. Especially, compared with the symmetric supercapacitors of MnO_2-NF//MnO_2-NF (6.7 Wh/kg) and GH//GH (5.5 Wh/kg), an about three-folds increase of energy density is obtained for the asymmetric supercapacitor of GH//MnO_2-NF (23.2 Wh/kg) at 1 A/g. More importantly, the asymmetric supercapacitor can provide a high energy density without sacrificing power density. When the power density increases to 10.0 kW/kg, the energy density of GH//MnO_2-NF still reaches 14.9 Wh/kg at 10 A/g. The maximum energy density obtained for the asymmetric supercapacitor of GH//MnO_2-NF at current density of 1 A/g is comparable or higher than MnO_2 based asymmetric supercapacitors in aqueous electrolytes, including PEDOT//MnO_2 (13.5 Wh/kg at 0.25 A/g) [284], FeOOH//MnO_2 (24 Wh/kg at 0.5 A/g) [325], activated carbon//MnO_2 (17.3 Wh/kg at 0.55 A/g) [287], activated carbon//$NaMnO_2$ (19.5 Wh/kg at ~0.04 A/g) [286], activated carbon//mesoporous MnO_2 (10.4 Wh/kg at ~0.3 A/g) [285], and activated carbon//$K_{0.}$27MnO2 0.6H_2O (25.3 Wh/kg at ~0.06 A/g) [326].

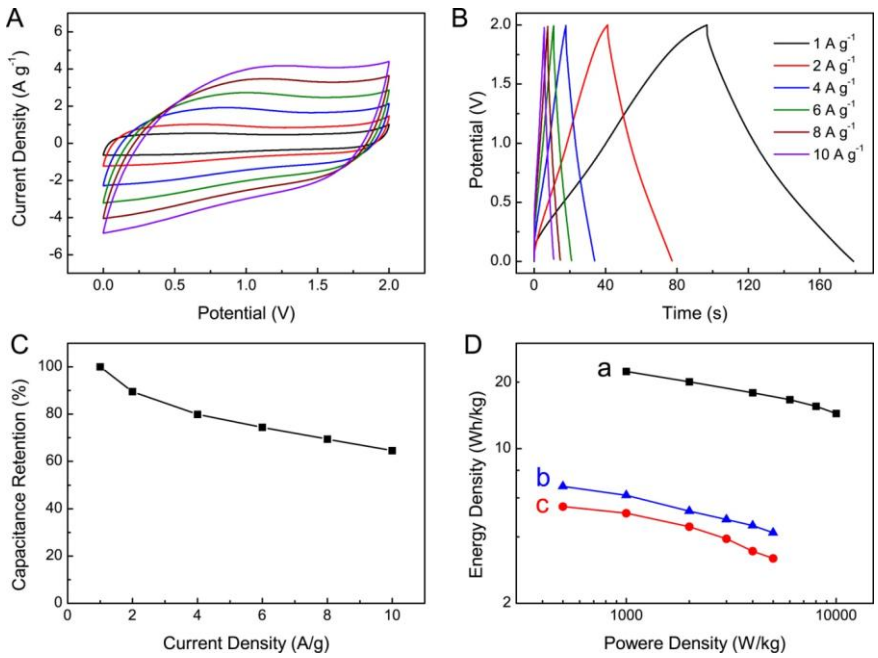

Figure 5.9 Electrochemical performance of GH//MnO_2-NF: (A) Cyclic voltammograms at scan rates from 10 to 100 mV/s (from inner to outer); (B) Charge/discharge curves at current densities from 1 to 10 A/g; (C) Capacitance retention ratio as a function of discharge currents; (D) Ragone plots of the asymmetric supercapacitor of GH//MnO_2-NF (a), and symmetric supercapacitors of MnO_2-NF//MnO_2-NF (b) and GH//GH (c).

The cycling test of our device exhibits a capacitance retention of 83.4 % over 5000 cycles (**Figure 5.10**A). Although occasional cracks were observed in MnO_2-NF electrode after the cycling test, MnO_2 is still uniformly coated on the branches of nickel foam and maintains its nanoplate structure. The resistance change of the asymmetric supercapacitor was monitored by electrochemical impedance spectroscopy (EIS). Nyquist plots were analyzed by the software of ZSimpWin on the basis of the equivalent circuit (**Figure 5.10**B). In the low-frequency region, the impedance plot increases sharply and tends to become vertical lines, which are the characteristics of pure capacitive behavior. At the high frequencies, the intercept at real axis (Z') represents the combined

resistance (R_s) including the resistance of electrolyte, the resistance of substrate, and contact resistance at the interface of active material and metal current collector. The charge transfer resistance (R_{ct}) at the electrode and electrolyte interface can be obtained from the semicircle part [327]. After 5000 cycles, we observed nearly no change for R_s (4.9 Ω), and only a slight increase of R_{ct} from 2.0 Ω to 3.7 Ω was observed, manifesting the exceptional stability of the asymmetric supercapacitor.

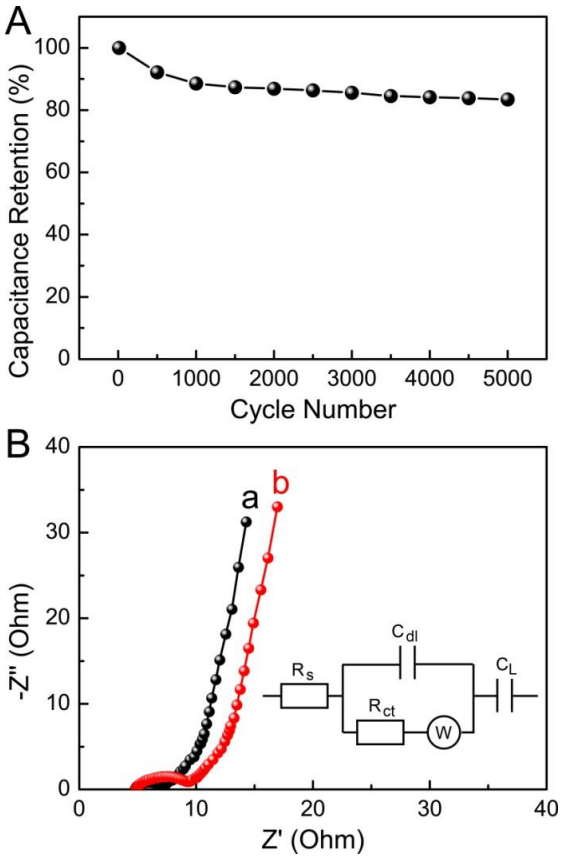

Figure 5.10 Cycle performance of GH//MnO_2-NF: (A) Capacitance retention with cycle numbers; (B) Nyquist plots in the frequency range of 0.1 Hz to 10 kHz before (a) and after (b) 5000 cycles, and the electrical equivalent circuit used for fitting impedance spectra.

6. Conclusions and outlook

6.1 Conclusions

Since the exfoliation of monolayer graphene sheets from graphite by Scotch-tape method in 2004, tremendous efforts have been devoted to explore its properties and applications of various fields. This material is a promising candidate in a wide range of electrochemical applications, arising from its unique properties including high surface areas, good electrical conductivity, and excellent chemical stability. Due to its flexible monolayer structure, graphene sheets also provide a versatile building block for macroscopic 2D and 3D materials with unique structures and functions while preserving the inherent properties of individual graphene sheets. We prepared this kind of macroscopic materials by several approaches and demonstrated their electrochemical applications as biosensors, fuel cells, and supercapacitors.

Firstly, PtNi alloy nanoparticles-graphene composite was developed through a facile and green one-step electrochemical reduction process from GO and metal precursors, by which well-dispersed alloy nanoparticles with high density can be loaded on the electrochemically reduced GO. As compared with PtNi alloy nanoparticles, PtNi-CRGO, and PtNi-SWNT nanocomposites, PtNi-ERGO modified electrode exhibits smaller electron transfer resistances and larger electrochemically active surface area, which makes it an ideal electrode material for electrocatalytic application. When used for glucose sensing, we found that the PtNi-ERGO nanocomposite based nonenzymatic sensor possesses many merits in terms of high selectivity, superior resistance to poisoning, low detection limit, rapid response, excellent reproducibility and

stability, which outmatches the performance of other nonenzymatic Pt-based glucose sensor that have been reported. The combination of these unique characters has enabled the application of this new type of nanoelectrocatalyst loaded electrodes for real human samples.

The one-step electrochemical strategy we developed, taking advantage of reduction of GO and deposition of metal nanoparticles at the cathodic conditions, opens the way for further preparation and screening of graphene supported electrocatalyst with different compositions and morphologies. An important feature of this approach is its feasibility to prepare multi-metallic nanoparticles by sampling varying the components of the solutions for electrodeposition. The multi-metallic nanoparticles, binary or ternary alloy, usually exhibit superior catalytic stability and activity compared with the mono-metallic nanoparticles as manifested in our work and other reports [328, 329]. Our strategy, metal nanoparticles modified graphene was obtained through the transfer of electrons directly to the GO and metal ion precursors immobilized on the surface of electrode, will also make a contribution to the developments of the environmentally-friendly methods for the preparation of carbon supported metal nanoparticles by avoiding the utilization of toxic chemical agents.

Secondly, a free-standing electrode is obtained by electrodeposition of Cu nanocubes on graphene paper (GP). The resultant Cu-GP, taking advantage of the high electrical conductivity of GP, well-dispersed Cu nanocubes, and the strong interaction between Cu nanocubes and GP substrate endowed by the electrodeposition method, exhibits high catalytic activity and stability towards the oxidation of hydrazine. An in-situ formed thin layer of Cu hydroxide/oxide

on Cu nanocube surfaces can lower the overpotential and stabilize the catalyst in alkaline conditions. A totally-irreversible and diffusion-controlled oxidation of hydrazine occurs on Cu-GP with nitrogen and water as the reaction products. The use of free-standing Cu-GP electrodes as the catalyst layer for DHFC applications would greatly simplify the manufacturing of electrode assemblies of fuel cells and offers new possibilities for the development of flexible power sources.

The utilization of free-standing graphene paper with superior electrical conductivity and mechanical strength as carbon support for metal electrocatalysts can make an important contribution towards the development of flexible electrodes for portable and wearable electronic devices [237, 330]. Our direct electrodeposition strategy to load metal nanoparticles on graphene paper also simplified the traditional procedure to prepare catalyst layer in fuel cells, where the electrodes are prepared by slurry coating of a mixture containing metal nanoparticles, conducting agents and polymer binders on carbon cloths. Another advantage of direct electrodeposition of metal nanoparticles on graphene paper is that the active surface of nanoparticles will not be possibly blocked by the polymer binders. The flexible nature of graphene paper also enables it to be coupled with other functionalization techniques. For example, by transferring a monolayer of gold nanoparticles at the liquid interface, a layer of close-packed gold nanoparticles was successfully dip-coated on the graphene paper in our group [91]. We also extended the application of graphene paper based electrodes to electrochemical biosensors, which holds great promise for development of portable biomedical devices towards point-of-care applications [331, 332].

Thirdly, we fabricated flexible asymmetric supercapacitors with free-standing graphene composite paper electrodes and a polymer gel electrolyte. The flexible device, benefiting from the mechanical and electrical properties of graphene papers, the functionalities of CNTs and Mn_3O_4 nanoparticles, and the excellent electrochemical properties of polymer gel electrolyte, have demonstrated extraordinary performance for supercapacitor applications, such as significantly improved energy density and excellent cycling performance. The integration of chemically tunable components of graphene, CNTs, functional nanoparticles, and polymer gel electrolytes opens the possibility for further screening of functional nanomaterials towards flexible and portable supercapacitors, batteries, fuel cells, biosensors, and other electronic devices.

At last, graphene hydrogel (GH) with 3D interconnected pores was successfully prepared by reducing GO with an eco-friendly reagent of L-glutathione under mild conditions. Vertically-aligned MnO_2 nanoplates were uniformly deposited on porous nickel foam under cathodic conditions. Asymmetric supercapacitor was fabricated by using these two materials as negative and positive electrodes, respectively. Benefitting from 3D GH with well-preserved graphene sheets, vertically-aligned MnO_2 nanoplates with sufficient free spaces, and the robust contact between MnO_2 and nickel foam, the asymmetric supercapacitor of GH//MnO_2-NF exhibits stable cycling performance and remarkable energy density. Such asymmetric supercapacitor offers great promise in the application of high-performance energy storage systems because of its advantages of low-cost, facile fabrication process, high energy and power density, and eco-friendly nature.

The incorporation of functional materials into graphene paper with the formation of sandwiched structures and the construction of graphene hydrogel provide some efficient approaches to prevent the restacking of graphene sheets that is commonly encountered in the graphene power materials. In order to successfully prepare these materials, we should pay some attention to the following points. First, it is crucial to tune the surface charge of rGO and the functional materials in order to get their stable mixtures, if we want to incorporate different functional materials into graphene paper. Second, the mass ratio of rGO and functional materials must be adjusted carefully when they are mixed together, to ensure the uniformly distribution of the functional materials in graphene paper without significantly loss of mechanical strength. Third, in order to preserve the porous structures of graphene hydrogel and retain the high surface area of this material, free-drying method is necessary, and supercritical CO_2 drying is preferred [110]. Finally, it is necessary to avoid any physical disturbance when preparing the graphene hydrogel by chemical reduction method; otherwise, it will be precipitated as aggregated rGO powers. Nevertheless, due to its mechanical integrity, both the graphene paper and the graphene hydrogel can be used as monolithic electrode materials, by eliminating the need for polymer binders and current collectors. It will improve the performance of a device when the overall weight is considered [333, 334]. Another important feature of graphene paper and graphene hydrogel (when pressed as film) is that they can offer the possibility to construct flexible electrochemical energy storage device, especially when combined with polymer gel electrolytes [244, 335].

6.2 Outlook and future directions

The flexible 2D structures and tunable functionalities enable graphene sheets as an attractive type of building blocks for macroscopic 2D and 3D materials which may not be accessible from other carbon nanomaterials. A number of approaches have been developed to fabricate these materials, while some excellent works have revealed that the 2D and 3D graphene materials can not only preserve the inherent properties of individual graphene sheets, but also possess additional functions arising from their hierarchical structures. Despite the considerable achievements in this area during the last few years, their successful implementation into practical applications will require further research efforts from different areas combining multiple disciplines including chemistry, physics, engineering, and material science. We consider that the research of hierarchical structures based on graphene sheets is still in its infancy and some issues and challenges remain for further studies.

First, the building blocks of graphene sheets determine the structures and properties of 2D and 3D graphene architectures, but it is still challenging to synthesize monodisperse graphene sheets with controlled sizes, shapes and number of layers in a large-scale through convenient approaches [336]. Several factors, such as the starting materials, the oxidation procedure, and the forms of exfoliation energy, play important roles in controlling the size or number of GO layers through the chemical oxidation and exfoliation process. For example, with increasing the oxidation time or the amount of oxidants, the average sizes of GO deceased from ~59,000 to ~550 nm^2 [337]. Sonication can produce smaller GO sheets than the mechanical shaking applied in the exfoliation process. By choosing different starting graphite materials with varied lateral

size and crystallinity, ~80% of the final GO products were tuned as single-layer, single- and double-layer, double- and triple-layer, and few-layer (4-10 layers) from artificial graphite, flake graphite power, Kish graphite, and natural flake graphite, respectively [338]. Therefore, it is anticipated that mono-dispersed graphene sheets with controlled number of layers can be obtained by selecting the proper starting materials, adjusting the oxidation conditions, and applying suitable mechanical energy for exfoliation or to decrease the lateral size.

Second, the electrical conductivity of graphene sheets is a crucial factor that determines the performances of the macroscopic graphene materials. However, there is still a lack of approaches to efficiently restore the aromatic framework with the production of graphene sheets with less defects and low oxygen to carbon ratio through environmentally friendly approaches. It was found that the temperature plays a more important role in removing the oxygen functionalities than the temperature when hydrazine was used as the reducing agents. For example, the carbon to oxygen atomic ratio in rGO increased from 3.0 after the reduction at 15 for 100 h to 15.1 after reduction at 95 for 3h ℃ [339]. The chemical reduction mechanism of GO and the influence of reaction parameters by other reducing agents, especially the environmentally friendly agents, and by other reducing methods such as electrochemical reduction, is still not fully investigated. Another challenge arises from the lack of efficient strategy to repair the defects and restore the honeycomb lattice in the reduction of GO. The alternative approach to produce GO with less defects would be more promising. It was found that the oxidation at low-temperature (below 10 ℃) can lead to the formation of GO with carbon skeleton preserved in tens

of nanometers, however, the yield is quite low compared with the conventional oxidation method [340].

Third, the shape or morphology of metal, metal oxide, or polymer nanoparticles may exert a great influence on their electrochemical performance. Nevertheless, it is still challenging to precisely tune the shape or morphology of the functional components loaded graphene sheets, especially on the 2D and 3D graphene materials. Due to its feasibility, the one-step strategy, reduction of GO and growth of functional materials, have been actively investigated. The application of surfactant can lead to the formation of functional materials with certain morphology [151, 341]. However, the one-step strategy lacks the ability to precisely control and/or adjust the composition and structure of the functional materials. On the other hand, the chemical methods for the synthesis of different nanomaterials, for example, metal, semiconductor, and polymer nanomaterials, with controlled properties have been well established. Two-step strategy, i.e., synthesis of the two components independently followed by combination of them, may be a promising approach to address the above-mentioned issues, but the challenge is how to attach the as-synthesized nanomaterials onto graphene sheets, while preserving their intrinsic properties.

Finally, the application of 2D and 3D graphene materials is not restricted to the above-mentioned research areas, and it is possible to introduce novel functional building blocks into the 2D and 3D graphene materials with enhanced performance in other fields through the existing and newly-developed methods. For example, due to the high specific surface areas, graphene sheets hold great potential as adsorbents to remove different pollutants from water, including dyes, pesticides, hormones, and heavy metals [342]. Especially, the

application of 3D graphene materials for waste water treatment would be more promising, because its monolithic structure enables the feasible post-treatment and can avoid the possible contamination induced by the adsorbents themselves if they are not fully removed from water after the adsorption of pollutants. Another promising field may be the antibacterial applications of graphene materials. The antibacterial materials have been widely used in our daily life to protect the public and human health. The conventional antibacterial materials typically include antibiotics, metal ions, and quaternary ammonium compounds. The successful application of graphene materials in the antibacterial field can avoid the concerns usually encountered by the traditional antibacterial materials, such as antibiotic resistance, environmental pollution, and relatively high cost [343]. Therefore, graphene materials may represent an emerging type of antibacterial materials and need more research work to promote the advancement of this interesting topic.

LIST OF REFERENCES

[1] Dreyer DR, Ruoff RS, Bielawski CW. From Conception to Realization: An Historial Account of Graphene and Some Perspectives for Its Future. *Angew Chem, Int Ed*. 2010, 49: 9336-9344.

[2] Boehm HP. Graphene-How a Laboratory Curiosity Suddenly Became Extremely Interesting. *Angew Chem, Int Ed*. 2010, 49: 9332-9335.

[3] Blakely JM, Kim JS, Potter HC. Segregation of Carbon to the (100) Surface of Nickel. *J Appl Phys*. 1970, 41: 2693-2697.

[4] Land TA, Michely T, Behm RJ, Hemminger JC, Comsa G. STM investigation of single layer graphite structures produced on Pt(111) by hydrocarbon decomposition. *Surf Sci*. 1992, 264: 261-270.

[5] Novoselov KS, Geim AK, Morozov SV, Jiang D, Zhang Y, Dubonos SV, Grigorieva IV, Firsov AA. Electric field effect in atomically thin carbon films. *Science*. 2004, 306: 666-669.

[6] Morozov SV, Novoselov KS, Katsnelson MI, Schedin F, Elias DC, Jaszczak JA, Geim AK. Giant intrinsic carrier mobilities in graphene and its bilayer. *Phys Rev Lett*. 2008, 100: 016602.

[7] Stoller MD, Park SJ, Zhu YW, An JH, Ruoff RS. Graphene-Based Ultracapacitors. *Nano Lett*. 2008, 8: 3498-3502.

[8] Kim K, Regan W, Geng BS, Aleman B, Kessler BM, Wang F, Crommie MF, Zettl A. High-temperature stability of suspended single-layer graphene. *Phys Status Solidi-Rapid Res Lett*. 2010, 4: 302-304.

[9] Ghosh S, Calizo I, Teweldebrhan D, Pokatilov EP, Nika DL, Balandin AA, Bao W, Miao F, Lau CN. Extremely high thermal conductivity of graphene: Prospects for thermal management applications in nanoelectronic circuits. *Appl Phys Lett*. 2008, 92: 151911.

[10] Lee C, Wei XD, Kysar JW, Hone J. Measurement of the elastic properties and intrinsic strength of monolayer graphene. *Science*. 2008, 321: 385-388.

[11] Zhu YW, Murali S, Cai WW, Li XS, Suk JW, Potts JR, Ruoff RS. Graphene and Graphene Oxide: Synthesis, Properties, and Applications. *Adv Mater*. 2010, 22: 3906-3924.

[12] Sutter PW, Flege JI, Sutter EA. Epitaxial graphene on ruthenium. *Nat Mater*. 2008, 7: 406-411.

[13] Hernandez Y, Nicolosi V, Lotya M, Blighe FM, Sun ZY, De S, McGovern IT, Holland B, Byrne M, Gun'ko YK, Boland JJ, Niraj P, Duesberg G, Krishnamurthy S, Goodhue R, Hutchison J, Scardaci V, Ferrari AC, Coleman JN. High-yield production of graphene by liquid-phase exfoliation of graphite. *Nat Nanotechnol*. 2008, 3: 563-568.

[14] Dreyer DR, Park S, Bielawski CW, Ruoff RS. The chemistry of graphene oxide. *Chem Soc Rev*. 2010, 39: 228-240.

[15] Mattevi C, Kim H, Chhowalla M. A review of chemical vapour deposition of graphene on copper. *J Mater Chem*. 2011, 21: 3324-3334.

[16] Wu JS, Pisula W, Mullen K. Graphenes as potential material for electronics. *Chem Rev*. 2007, 107: 718-747.

[17] Park S, Ruoff RS. Chemical methods for the production of graphenes. *Nat Nanotechnol*. 2009, 4: 217-224.

[18] Bai H, Li C, Shi GQ. Functional Composite Materials Based on Chemically Converted Graphene. *Adv Mater*. 2011, 23: 1089-1115.

[19] Brodie BC. On the atomic weight of graphite. *Phil Trans R Soc Lond*. 1859, 149: 249-259.
[20] Compton OC, Nguyen ST. Graphene Oxide, Highly Reduced Graphene Oxide, and Graphene: Versatile Building Blocks for Carbon-Based Materials. *Small*. 2010, 6: 711-723.
[21] Hummers WS, Offeman RE. Preparation of Graphitic Oxide. *J Am Chem Soc*. 1958, 80: 1339-1339.
[22] Stankovich S, Dikin DA, Piner RD, Kohlhaas KA, Kleinhammes A, Jia Y, Wu Y, Nguyen ST, Ruoff RS. Synthesis of graphene-based nanosheets via chemical reduction of exfoliated graphite oxide. *Carbon*. 2007, 45: 1558-1565.
[23] Pan SY, Aksay IA. Factors Controlling the Size of Graphene Oxide Sheets Produced via the Graphite Oxide Route. *ACS Nano*. 2011, 5: 4073-4083.
[24] Gao W, Alemany LB, Ci LJ, Ajayan PM. New insights into the structure and reduction of graphite oxide. *Nat Chem*. 2009, 1: 403-408.
[25] Li D, Muller MB, Gilje S, Kaner RB, Wallace GG. Processable aqueous dispersions of graphene nanosheets. *Nat Nanotechnol*. 2008, 3: 101-105.
[26] Zhou YG, Chen JJ, Wang FB, Sheng ZH, Xia XH. A facile approach to the synthesis of highly electroactive Pt nanoparticles on graphene as an anode catalyst for direct methanol fuel cells. *Chem Commun*. 2010, 46: 5951-5953.
[27] Sridhar V, Jeon JH, Oh IK. Synthesis of graphene nano-sheets using eco-friendly chemicals and microwave radiation. *Carbon*. 2010, 48: 2953-2957.
[28] Williams G, Seger B, Kamat PV. TiO2-graphene nanocomposites. UV-assisted photocatalytic reduction of graphene oxide. *ACS Nano*. 2008, 2: 1487-1491.
[29] Cote LJ, Cruz-Silva R, Huang JX. Flash Reduction and Patterning of Graphite Oxide and Its Polymer Composite. *J Am Chem Soc*. 2009, 131: 11027-11032.
[30] Wang GM, Qian F, Saltikov C, Jiao YQ, Li Y. Microbial reduction of graphene oxide by Shewanella. *Nano Res*. 2011, 4: 563-570.
[31] Croft RC. Lamellar compounds of graphite. *Q Rev Chem Soc*. 1960, 14: 1-45.
[32] Kotov NA, Dekany I, Fendler JH. Ultrathin graphite oxide-polyelectrolyte composites prepared by self-assembly: Transition between conductive and non-conductive states. *Adv Mater*. 1996, 8: 637-641.
[33] Stankovich S, Piner RD, Chen XQ, Wu NQ, Nguyen ST, Ruoff RS. Stable aqueous dispersions of graphitic nanoplatelets via the reduction of exfoliated graphite oxide in the presence of poly(sodium 4-styrenesulfonate). *J Mater Chem*. 2006, 16: 155-158.
[34] Fernandez-Merino MJ, Guardia L, Paredes JI, Villar-Rodil S, Solis-Fernandez P, Martinez-Alonso A, Tascon JMD. Vitamin C Is an Ideal Substitute for Hydrazine in the Reduction of Graphene Oxide Suspensions. *J Phys Chem C*. 2010, 114: 6426-6432.
[35] Pei SF, Zhao JP, Du JH, Ren WC, Cheng HM. Direct reduction of graphene oxide films into highly conductive and flexible graphene films by hydrohalic acids. *Carbon*. 2010, 48: 4466-4474.
[36] Zhang JL, Yang HJ, Shen GX, Cheng P, Zhang JY, Guo SW. Reduction of graphene oxide via L-ascorbic acid. *Chem Commun*. 2010, 46: 1112-1114.
[37] Park S, An JH, Piner RD, Jung I, Yang DX, Velamakanni A, Nguyen ST, Ruoff RS. Aqueous Suspension and Characterization of Chemically Modified Graphene Sheets. *Chem Mater*. 2008, 20: 6592-6594.

[38] Pham TA, Kim JS, Kim JS, Jeong YT. One-step reduction of graphene oxide with L-glutathione. *Colloid Surf A: Physicochem Eng Aspects*. 2011, 384: 543-548.
[39] Lei ZB, Lu L, Zhao XS. The electrocapacitive properties of graphene oxide reduced by urea. *Energy Environ Sci*. 2012, 5: 6391-6399.
[40] Chen DZ, Li LD, Guo L. An environment-friendly preparation of reduced graphene oxide nanosheets via amino acid. *Nanotechnology*. 2011, 22: 325601.
[41] Xu LQ, Yang WJ, Neoh KG, Kang ET, Fu GD. Dopamine-Induced Reduction and Functionalization of Graphene Oxide Nanosheets. *Macromolecules*. 2010, 43: 8336-8339.
[42] Fan ZJ, Kai W, Yan J, Wei T, Zhi LJ, Feng J, Ren YM, Song LP, Wei F. Facile Synthesis of Graphene Nanosheets via Fe Reduction of Exfoliated Graphite Oxide. *ACS Nano*. 2010, 5: 191-198.
[43] Fan ZJ, Wang K, Wei T, Yan J, Song LP, Shao B. An environmentally friendly and efficient route for the reduction of graphene oxide by aluminum powder. *Carbon*. 2010, 48: 1686-1689.
[44] Mei XG, Zheng HQ, Ouyang JY. Ultrafast reduction of graphene oxide with Zn powder in neutral and alkaline solutions at room temperature promoted by the formation of metal complexes. *J Mater Chem*. 2012, 22: 9109-9116.
[45] Xue YH, Chen H, Yu DS, Wang SY, Yardeni M, Dai QB, Guo MM, Liu Y, Lu F, Qu J, Dai LM. Oxidizing metal ions with graphene oxide: the in situ formation of magnetic nanoparticles on self-reduced graphene sheets for multifunctional applications. *Chem Commun*. 2011, 47: 11689-11691.
[46] Zhu CZ, Guo SJ, Fang YX, Dong SJ. Reducing Sugar: New Functional Molecules for the Green Synthesis of Graphene Nanosheets. *ACS Nano*. 2010, 4: 2429-2437.
[47] Wang Y, Shi ZX, Yin J. Facile Synthesis of Soluble Graphene via a Green Reduction of Graphene Oxide in Tea Solution and Its Biocomposites. *ACS Appl Mater Interfaces*. 2011, 3: 1127-1133.
[48] Kuila T, Bose S, Khanra P, Mishra AK, Kim NH, Lee JH. A green approach for the reduction of graphene oxide by wild carrot root. *Carbon*. 2012, 50: 914-921.
[49] Zhou Y, Bao QL, Tang LAL, Zhong YL, Loh KP. Hydrothermal Dehydration for the "Green" Reduction of Exfoliated Graphene Oxide to Graphene and Demonstration of Tunable Optical Limiting Properties. *Chem Mater*. 2009, 21: 2950-2956.
[50] Zhou M, Wang YL, Zhai YM, Zhai JF, Ren W, Wang FA, Dong SJ. Controlled Synthesis of Large-Area and Patterned Electrochemically Reduced Graphene Oxide Films. *Chem-Eur J*. 2009, 15: 6116-6120.
[51] Shao YY, Wang J, Engelhard M, Wang CM, Lin YH. Facile and controllable electrochemical reduction of graphene oxide and its applications. *J Mater Chem*. 2010, 20: 743-748.
[52] Zhu CZ, Guo SJ, Fang YX, Han L, Wang EK, Dong SJ. One-step electrochemical approach to the synthesis of Graphene/MnO2 nanowall hybrids. *Nano Res*. 2011, 4: 648-657.
[53] Jimenez PSV. Thermal decomposition of graphite oxidation products DSC studies of internal combustion of graphite oxide. *Mater Res Bull*. 1987, 22: 601-608.
[54] Matuyama E. Pyrolysis of graphitic acid. *J Phys Chem*. 1954, 58: 215-219.

[55] Schniepp HC, Li JL, McAllister MJ, Sai H, Herrera-Alonso M, Adamson DH, Prud'homme RK, Car R, Saville DA, Aksay IA. Functionalized single graphene sheets derived from splitting graphite oxide. *J Phys Chem B*. 2006, 110: 8535-8539.
[56] Wang ZL, Xu D, Huang Y, Wu Z, Wang LM, Zhang XB. Facile, mild and fast thermal-decomposition reduction of graphene oxide in air and its application in high-performance lithium batteries. *Chem Commun*. 2012, 48: 976-978.
[57] McAllister MJ, Li JL, Adamson DH, Schniepp HC, Abdala AA, Liu J, Herrera-Alonso M, Milius DL, Car R, Prud'homme RK, Aksay IA. Single sheet functionalized graphene by oxidation and thermal expansion of graphite. *Chem Mater*. 2007, 19: 4396-4404.
[58] Zhu YW, Murali S, Stoller MD, Velamakanni A, Piner RD, Ruoff RS. Microwave assisted exfoliation and reduction of graphite oxide for ultracapacitors. *Carbon*. 2010, 48: 2118-2122.
[59] Kim F, Luo JY, Cruz-Silva R, Cote LJ, Sohn K, Huang JX. Self-Propagating Domino-like Reactions in Oxidized Graphite. *Adv Funct Mater*. 2010, 20: 2867-2873.
[60] Krishnan D, Kim F, Luo JY, Cruz-Silva R, Cote LJ, Jang HD, Huang JX. Energetic graphene oxide: Challenges and opportunities. *Nano Today*. 2012, 7: 137-152.
[61] Williams G, Kamat PV. Graphene-semiconductor nanocomposites: Excited-state interactions between ZnO nanoparticles and graphene oxide. *Langmuir*. 2009, 25: 13869-13873.
[62] Wu TS, Liu S, Luo YL, Lu WB, Wang L, Sun XP. Surface plasmon resonance-induced visible light photocatalytic reduction of graphene oxide: Using Ag nanoparticles as a plasmonic photocatalyst. *Nanoscale*. 2011, 3: 2142-2144.
[63] Zhang HH, Liu Q, Feng K, Chen B, Tung CH, Wu LZ. Facile Photoreduction of Graphene Oxide by an NAD(P)H Model: Hantzsch 1,4-Dihydropyridine. *Langmuir*. 2012, 28: 8224-8229.
[64] Salas EC, Sun ZZ, Luttge A, Tour JM. Reduction of Graphene Oxide via Bacterial Respiration. *ACS Nano*. 2010, 4: 4852-4856.
[65] Akhavan O, Ghaderi E. Escherichia coil bacteria reduce graphene oxide to bactericidal graphene in a self-limiting manner. *Carbon*. 2012, 50: 1853-1860.
[66] Wu DQ, Zhang F, Liang HW, Feng XL. Nanocomposites and macroscopic materials: assembly of chemically modified graphene sheets. *Chem Soc Rev*. 2012, 41: 6160-6177.
[67] Park JY, Advincula RC. Nanostructuring polymers, colloids, and nanomaterials at the air-water interface through Langmuir and Langmuir-Blodgett techniques. *Soft Matter*. 2011, 7: 9829-9843.
[68] Tao AR, Huang JX, Yang PD. Langmuir-Blodgettry of Nanocrystals and Nanowires. *Accounts Chem Res*. 2008, 41: 1662-1673.
[69] Cote LJ, Kim F, Huang JX. Langmuir-Blodgett Assembly of Graphite Oxide Single Layers. *J Am Chem Soc*. 2009, 131: 1043-1049.
[70] Cote LJ, Kim J, Zhang Z, Sun C, Huang JX. Tunable assembly of graphene oxide surfactant sheets: wrinkles, overlaps and impacts on thin film properties. *Soft Matter*. 2010, 6: 6096-6101.

[71] Zheng QB, Ip WH, Lin XY, Yousefi N, Yeung KK, Li ZG, Kim JK. Transparent Conductive Films Consisting of Ultra large Graphene Sheets Produced by Langmuir-Blodgett Assembly. *ACS Nano*. 2011, 5: 6039-6051.
[72] Li XL, Zhang GY, Bai XD, Sun XM, Wang XR, Wang E, Dai HJ. Highly conducting graphene sheets and Langmuir-Blodgett films. *Nat Nanotechnol*. 2008, 3: 538-542.
[73] Kim J, Cote LJ, Kim F, Yuan W, Shull KR, Huang JX. Graphene Oxide Sheets at Interfaces. *J Am Chem Soc*. 2010, 132: 8180-8186.
[74] Zheng QB, Zhang B, Lin XY, Shen X, Yousefi N, Huang ZD, Li ZG, Kim JK. Highly transparent and conducting ultralarge graphene oxide/single-walled carbon nanotube hybrid films produced by Langmuir-Blodgett assembly. *J Mater Chem*. 2012, 22: 25072-25082.
[75] Byon HR, Lee SW, Chen S, Hammond PT, Shao-Horn Y. Thin films of carbon nanotubes and chemically reduced graphenes for electrochemical micro-capacitors. *Carbon*. 2011, 49: 457-467.
[76] Yu DS, Dai LM. Self-Assembled Graphene/Carbon Nanotube Hybrid Films for Supercapacitors. *J Phys Chem Lett*. 2010, 1: 467-470.
[77] Zhao X, Zhang QH, Hao YP, Li YZ, Fang Y, Chen DJ. Alternate Multilayer Films of Poly(vinyl alcohol) and Exfoliated Graphene Oxide Fabricated via a Facial Layer-by-Layer Assembly. *Macromolecules*. 2010, 43: 9411-9416.
[78] Li ZP, Wang JQ, Liu XH, Liu S, Ou JF, Yang SR. Electrostatic layer-by-layer self-assembly multilayer films based on graphene and manganese dioxide sheets as novel electrode materials for supercapacitors. *J Mater Chem*. 2011, 21: 3397-3403.
[79] Kulkarni DD, Choi I, Singamaneni S, Tsukruk VV. Graphene Oxide-Polyelectrolyte Nanomembranes. *ACS Nano*. 2010, 4: 4667-4676.
[80] Ballard DGH, Rideal GR. Flexible inorganic films and coatings. *J Mater Sci*. 1983, 18: 545-561.
[81] Dikin DA, Stankovich S, Zimney EJ, Piner RD, Dommett GHB, Evmenenko G, Nguyen ST, Ruoff RS. Preparation and characterization of graphene oxide paper. *Nature*. 2007, 448: 457-460.
[82] Yang XW, Qiu L, Cheng C, Wu YZ, Ma ZF, Li D. Ordered Gelation of Chemically Converted Graphene for Next-Generation Electroconductive Hydrogel Films. *Angew Chem, Int Ed*. 2011, 50: 7325-7328.
[83] Chen H, Muller MB, Gilmore KJ, Wallace GG, Li D. Mechanically strong, electrically conductive, and biocompatible graphene paper. *Adv Mater*. 2008, 20: 3557-3561.
[84] Park S, Mohanty N, Suk JW, Nagaraja A, An JH, Piner RD, Cai WW, Dreyer DR, Berry V, Ruoff RS. Biocompatible, Robust Free-Standing Paper Composed of a TWEEN/Graphene Composite. *Adv Mater*. 2010, 22: 1736-1740.
[85] Wu Q, Xu YX, Yao ZY, Liu AR, Shi GQ. Supercapacitors Based on Flexible Graphene/Polyaniline Nanofiber Composite Films. *ACS Nano*. 2010, 4: 1963-1970.
[86] Wang DH, Kou R, Choi D, Yang ZG, Nie ZM, Li J, Saraf LV, Hu DH, Zhang JG, Graff GL, Liu J, Pope MA, Aksay IA. Ternary Self-Assembly of Ordered Metal Oxide-Graphene Nanocomposites for Electrochemical Energy Storage. *ACS Nano*. 2010, 4: 1587-1595.

[87] Li ZP, Mi YJ, Liu XH, Liu S, Yang SR, Wang JQ. Flexible graphene/MnO2 composite papers for supercapacitor electrodes. *J Mater Chem*. 2011, 21: 14706-14711.
[88] Chen CM, Yang QH, Yang YG, Lv W, Wen YF, Hou PX, Wang MZ, Cheng HM. Self-Assembled Free-Standing Graphite Oxide Membrane. *Adv Mater*. 2009, 21: 3007-3011.
[89] Zhu YW, Cai WW, Piner RD, Velamakanni A, Ruoff RS. Transparent self-assembled films of reduced graphene oxide platelets. *Appl Phys Lett*. 2009, 95: 103104.
[90] Shao JJ, Lv W, Guo QG, Zhang C, Xu Q, Yang QH, Kang FY. Hybridization of graphene oxide and carbon nanotubes at the liquid/air interface. *Chem Commun*. 2012, 48: 3706-3708.
[91] Xiao F, Song JB, Gao HC, Zan XL, Xu R, Duan HW. Coating Graphene Paper with 2D-Assembly of Electrocatalytic Nanoparticles: A Modular Approach toward High-Performance Flexible Electrodes. *ACS Nano*. 2012, 6: 100-110.
[92] Cong HP, Ren XC, Wang P, Yu SH. Flexible graphene-polyaniline composite paper for high-performance supercapacitor. *Energy Environ Sci*. 2013, 6: 1185-1191.
[93] Van der Biest OO, Vandeperre LJ. Electrophoretic deposition of materials. *Annu Rev Mater Sci*. 1999, 29: 327-352.
[94] Chavez-Valdez A, Shaffer MSP, Boccaccini AR. Applications of graphene electrophoretic deposition. A review. *J Phys Chem B*. 2013, 117: 1502-1515.
[95] Zhang ZB, Yuan SJ, Zhu XL, Neoh KG, Kang ET. Enzyme-mediated amperometric biosensors prepared via successive surface-initiated atom-transfer radical polymerization. *Biosens Bioelectron*. 2010, 25: 1102-1108.
[96] Ata MS, Sun Y, Li X, Zhitomirsky I. Electrophoretic deposition of graphene, carbon nanotubes and composites using aluminon as charging and film forming agent. *Colloid Surf A: Physicochem Eng Aspects*. 2012, 398: 9-16.
[97] Chen Y, Zhang X, Yu P, Ma YW. Electrophoretic deposition of graphene nanosheets on nickel foams for electrochemical capacitors. *J Power Sources*. 2010, 195: 3031-3035.
[98] Lin JY, Chan CY, Chou SW. Electrophoretic deposition of transparent MoS2-graphene nanosheet composite films as counter electrodes in dye-sensitized solar cells. *Chem Commun*. 2013, 49: 1440-1442.
[99] Zhu G, Pan LK, Lu T, Xu T, Sun Z. Electrophoretic deposition of reduced graphene-carbon nanotubes composite films as counter electrodes of dye-sensitized solar cells. *J Mater Chem*. 2011, 21: 14869-14875.
[100] Guo CX, Yang HB, Sheng ZM, Lu ZS, Song QL, Li CM. Layered Graphene/Quantum Dots for Photovoltaic Devices. *Angew Chem, Int Ed*. 2010, 49: 3014-3017.
[101] Chen LY, Tang YH, Wang K, Liu CB, Luo SL. Direct electrodeposition of reduced graphene oxide on glassy carbon electrode and its electrochemical application. *Electrochem Commun*. 2011, 13: 133-137.
[102] Hilder M, Winther-Jensen B, Li D, Forsyth M, MacFarlane DR. Direct electro-deposition of graphene from aqueous suspensions. *Phys Chem Chem Phys*. 2011, 13: 9187-9193.

[103] Liu CB, Wang K, Luo SL, Tang YH, Chen LY. Direct Electrodeposition of Graphene Enabling the One-Step Synthesis of Graphene-Metal Nanocomposite Films. *Small*. 2011, 7: 1203-1206.
[104] Tang YH, Wu N, Luo SL, Liu CB, Wang K, Chen LY. One-Step Electrodeposition to Layer-by-Layer Graphene-Conducting-Polymer Hybrid Films. *Macromol Rapid Commun*. 2012, 33: 1780-1786.
[105] Xu YX, Sheng KX, Li C, Shi GQ. Self-Assembled Graphene Hydrogel via a One-Step Hydrothermal Process. *ACS Nano*. 2010, 4: 4324-4330.
[106] Sheng KX, Xu YX, Li C, Shi GQ. High-performance self-assembled graphene hydrogels prepared by chemical reduction of graphene oxide. *New Carbon Mater*. 2011, 26: 9-15.
[107] Chen WF, Yan LF. In situ self-assembly of mild chemical reduction graphene for three-dimensional architectures. *Nanoscale*. 2011, 3: 3132-3137.
[108] Qiu L, Yang XW, Gou XL, Yang WR, Ma ZF, Wallace GG, Li D. Dispersing Carbon Nanotubes with Graphene Oxide in Water and Synergistic Effects between Graphene Derivatives. *Chem-Eur J*. 2010, 16: 10653-10658.
[109] Sui ZY, Meng QH, Zhang XT, Ma R, Cao B. Green synthesis of carbon nanotube-graphene hybrid aerogels and their use as versatile agents for water purification. *J Mater Chem*. 2012, 22: 8767-8771.
[110] Sui ZY, Zhang XT, Lei Y, Luo YJ. Easy and green synthesis of reduced graphite oxide-based hydrogels. *Carbon*. 2011, 49: 4314-4321.
[111] Cong HP, Ren XC, Wang P, Yu SH. Macroscopic Multifunctional Graphene-Based Hydrogels and Aerogels by a Metal Ion Induced Self-Assembly Process. *ACS Nano*. 2012, 6: 2693-2703.
[112] Choi BG, Yang M, Hong WH, Choi JW, Huh YS. 3D Macroporous Graphene Frameworks for Supercapacitors with High Energy and Power Densities. *ACS Nano*. 2012, 6: 4020-4028.
[113] Sohn K, Na YJ, Chang H, Roh KM, Jang HD, Huang JX. Oil absorbing graphene capsules by capillary molding. *Chem Commun*. 2012, 48: 5968-5970.
[114] Huang XD, Qian K, Yang J, Zhang J, Li L, Yu CZ, Zhao DY. Functional Nanoporous Graphene Foams with Controlled Pore Sizes. *Adv Mater*. 2012, 24: 4419-4423.
[115] Chen ZP, Ren WC, Gao LB, Liu BL, Pei SF, Cheng HM. Three-dimensional flexible and conductive interconnected graphene networks grown by chemical vapour deposition. *Nat Mater*. 2011, 10: 424-428.
[116] Cao XH, Shi YM, Shi WH, Lu G, Huang X, Yan QY, Zhang QC, Zhang H. Preparation of Novel 3D Graphene Networks for Supercapacitor Applications. *Small*. 2011, 7: 3163-3168.
[117] Bi H, Huang FQ, Liang J, Tang YF, Lu XJ, Xie XM, Jiang MH. Large-scale preparation of highly conductive three dimensional graphene and its applications in CdTe solar cells. *J Mater Chem*. 2011, 21: 17366-17370.
[118] Dong XC, Xu H, Wang XW, Huang YX, Chan-Park MB, Zhang H, Wang LH, Huang W, Chen P. 3D Graphene-Cobalt Oxide Electrode for High-Performance Supercapacitor and Enzymeless Glucose Detection. *ACS Nano*. 2012, 6: 3206-3213.
[119] Yong YC, Dong XC, Chan-Park MB, Song H, Chen P. Macroporous and Monolithic Anode Based on Polyaniline Hybridized Three-Dimensional Graphene for High-Performance Microbial Fuel Cells. *ACS Nano*. 2012, 6: 2394-2400.

[120] Maiyalagan T, Dong XC, Chen P, Wang X. Electrodeposited Pt on three-dimensional interconnected graphene as a free-standing electrode for fuel cell application. *J Mater Chem*. 2012, 22: 5286-5290.
[121] Choi BG, Park H, Park TJ, Yang MH, Kim JS, Jang SY, Heo NS, Lee SY, Kong J, Hong WH. Solution Chemistry of Self-Assembled Graphene Nanohybrids for High-Performance Flexible Biosensors. *ACS Nano*. 2010, 4: 2910-2918.
[122] Guo CX, Ng SR, Khoo SY, Zheng XT, Chen P, Li CM. RGD-Peptide Functionalized Graphene Biomimetic Live-Cell Sensor for Real-Time Detection of Nitric Oxide Molecules. *ACS Nano*. 2012, 6: 6944-6951.
[123] Xiao F, Li YQ, Zan XL, Liao K, Xu R, Duan HW. Growth of Metal-Metal Oxide Nanostructures on Freestanding Graphene Paper for Flexible Biosensors. *Adv Funct Mater*. 2012, 22: 2487-2494.
[124] Chen L, Wang XJ, Zhang XT, Zhang HM. 3D porous and redox-active prussian blue-in-graphene aerogels for highly efficient electrochemical detection of H2O2. *J Mater Chem*. 2012, 22: 22090-22096.
[125] Xiao XY, Michael JR, Beechem T, McDonald A, Rodriguez M, Brtunbach MT, Lambert TN, Washburn CM, Wang J, Brozik SM, Wheeler DR, Burckel DB, Polsky R. Three dimensional nickel-graphene core-shell electrodes. *J Mater Chem*. 2012, 22: 23749-23754.
[126] Sattayasamitsathit S, Gu YE, Kaufmann K, Jia WZ, Xiao XY, Rodriguez M, Minteer S, Cha J, Burckel DB, Wang CM, Polsky R, Wang J. Highly ordered multilayered 3D graphene decorated with metal nanoparticles. *J Mater Chem A*. 2013, 1: 1639-1645.
[127] Hu YJ, Zhang H, Wu P, Zhang H, Zhou B, Cai CX. Bimetallic Pt-Au nanocatalysts electrochemically deposited on graphene and their electrocatalytic characteristics towards oxygen reduction and methanol oxidation. *Phys Chem Chem Phys*. 2011, 13: 4083-4094.
[128] Zarrin H, Higgins D, Jun Y, Chen ZW, Fowler M. Functionalized Graphene Oxide Nanocomposite Membrane for Low Humidity and High Temperature Proton Exchange Membrane Fuel Cells. *J Phys Chem C*. 2011, 115: 20774-20781.
[129] Tseng CY, Ye YS, Cheng MY, Kao KY, Shen WC, Rick J, Chen JC, Hwang BJ. Sulfonated Polyimide Proton Exchange Membranes with Graphene Oxide show Improved Proton Conductivity, Methanol Crossover Impedance, and Mechanical Properties. *Adv Energy Mater*. 2011, 1: 1220-1224.
[130] Ravikumar, Scott K. Freestanding sulfonated graphene oxide paper: a new polymer electrolyte for polymer electrolyte fuel cells. *Chem Commun*. 2012, 48: 5584-5586.
[131] Wu ZS, Yang SB, Sun Y, Parvez K, Feng XL, Mullen K. 3D Nitrogen-Doped Graphene Aerogel-Supported Fe3O4 Nanoparticles as Efficient Eletrocatalysts for the Oxygen Reduction Reaction. *J Am Chem Soc*. 2012, 134: 9082-9085.
[132] Fu XG, Jin JT, Liu YR, Liu Q, Niu KX, Zhang JY, Cao XP. Graphene-xerogel-based non-precious metal catalyst for oxygen reduction reaction. *Electrochem Commun*. 2013, 28: 5-8.
[133] Qiu HJ, Dong XC, Sana B, Peng T, Paramelle D, Chen P, Lim S. Ferritin-Templated Synthesis and Self-Assembly of Pt Nanoparticles on a Monolithic Porous Graphene Network for Electrocatalysis in Fuel Cells. *ACS Appl Mater Interfaces*. 2013, 5: 782-787.

[134] Hu CG, Cheng HH, Zhao Y, Hu Y, Liu Y, Dai LM, Qu LT. Newly-Designed Complex Ternary Pt/PdCu Nanoboxes Anchored on Three-Dimensional Graphene Framework for Highly Efficient Ethanol Oxidation. *Adv Mater*. 2012, 24: 5493-5498.
[135] Wang DW, Li F, Zhao JP, Ren WC, Chen ZG, Tan J, Wu ZS, Gentle I, Lu GQ, Cheng HM. Fabrication of Graphene/Polyaniline Composite Paper via In Situ Anodic Electropolymerization for High-Performance Flexible Electrode. *ACS Nano*. 2009, 3: 1745-1752.
[136] Yuan CZ, Yang L, Hou LR, Li JY, Sun YX, Zhang XG, Shen LF, Lu XJ, Xiong SL, Lou XW. Flexible Hybrid Paper Made of Monolayer Co3O4 Microsphere Arrays on rGO/CNTs and Their Application in Electrochemical Capacitors. *Adv Funct Mater*. 2012, 22: 2560-2566.
[137] Zhao X, Hayner CM, Kung MC, Kung HH. Flexible Holey Graphene Paper Electrodes with Enhanced Rate Capability for Energy Storage Applications. *ACS Nano*. 2011, 5: 8739-8749.
[138] Gwon H, Kim HS, Lee KU, Seo DH, Park YC, Lee YS, Ahn BT, Kang K. Flexible energy storage devices based on graphene paper. *Energy Environ Sci*. 2011, 4: 1277-1283.
[139] Lee JW, Lim SY, Jeong HM, Hwang TH, Kang JK, Choi JW. Extremely stable cycling of ultra-thin V2O5 nanowire-graphene electrodes for lithium rechargeable battery cathodes. *Energy Environ Sci*. 2012, 5: 9889-9894.
[140] Sun YQ, Wu Q, Shi GQ. Supercapacitors based on self-assembled graphene organogel. *Phys Chem Chem Phys*. 2011, 13: 17249-17254.
[141] Wu ZS, Winter A, Chen L, Sun Y, Turchanin A, Feng XL, Mullen K. Three-Dimensional Nitrogen and Boron Co-doped Graphene for High-Performance All-Solid-State Supercapacitors. *Adv Mater*. 2012, 24: 5130-5135.
[142] Zhao Y, Liu J, Hu Y, Cheng HH, Hu CG, Jiang CC, Jiang L, Cao AY, Qu LT. Highly compression-tolerant supercapacitor based on polypyrrole-mediated graphene foam electrodes. *Adv Mater*. 2013, 25: 591-595.
[143] Li N, Chen ZP, Ren WC, Li F, Cheng HM. Flexible graphene-based lithium ion batteries with ultrafast charge and discharge rates. *Proc Natl Acad Sci U S A*. 2012, 109: 17360-17365.
[144] Ji HX, Zhang LL, Pettes MT, Li HF, Chen SS, Shi L, Piner R, Ruoff RS. Ultrathin Graphite Foam: A Three-Dimensional Conductive Network for Battery Electrodes. *Nano Lett*. 2012, 12: 2446-2451.
[145] Shen LF, Zhang XG, Li HS, Yuan CZ, Cao GZ. Design and Tailoring of a Three-Dimensional TiO2-Graphene-Carbon Nanotube Nanocomposite for Fast Lithium Storage. *J Phys Chem Lett*. 2011, 2: 3096-3101.
[146] Luo JY, Zhao X, Wu JS, Jang HD, Kung HH, Huang JX. Crumpled Graphene-Encapsulated Si Nanoparticles for Lithium Ion Battery Anodes. *J Phys Chem Lett*. 2012, 3: 1824-1829.
[147] Matsumoto Y, Koinuma M, Kim SY, Watanabe Y, Taniguchi T, Hatakeyama K, Tateishi H, Ida S. Simple Photoreduction of Graphene Oxide Nanosheet under Mild Conditions. *ACS Appl Mater Interfaces*. 2010, 2: 3461-3466.
[148] Kamat PV. Graphene-Based Nanoarchitectures. Anchoring Semiconductor and Metal Nanoparticles on a Two-Dimensional Carbon Support. *J Phys Chem Lett*. 2010, 1: 520-527.

[149] Wang XL, Han WQ. Graphene Enhances Li Storage Capacity of Porous Single-Crystalline Silicon Nanowires. *ACS Appl Mater Interfaces*. 2010, 2: 3709-3713.
[150] Wu ZS, Ren WC, Wen L, Gao LB, Zhao JP, Chen ZP, Zhou GM, Li F, Cheng HM. Graphene Anchored with Co3O4 Nanoparticles as Anode of Lithium Ion Batteries with Enhanced Reversible Capacity and Cyclic Performance. *ACS Nano*. 2010, 4: 3187-3194.
[151] Guo SJ, Dong SJ, Wang EK. Three-Dimensional Pt-on-Pd Bimetallic Nanodendrites Supported on Graphene Nanosheet: Facile Synthesis and Used as an Advanced Nanoelectrocatalyst for Methanol Oxidation. *ACS Nano*. 2010, 4: 547-555.
[152] Fan GF, Zhu HW, Wang KL, Wei JQ, Li XM, Shu QK, Guo N, Wu DH. Graphene/Silicon Nanowire Schottky Junction for Enhanced Light Harvesting. *ACS Appl Mater Interfaces*. 2011, 3: 721-725.
[153] Shan CS, Yang HF, Han DX, Zhang QX, Ivaska A, Niu L. Graphene/AuNPs/chitosan nanocomposites film for glucose biosensing. *Biosens Bioelectron*. 2010, 25: 1070-1074.
[154] Goncalves G, Marques P, Granadeiro CM, Nogueira HIS, Singh MK, Gracio J. Surface Modification of Graphene Nanosheets with Gold Nanoparticles: The Role of Oxygen Moieties at Graphene Surface on Gold Nucleation and Growth. *Chem Mater*. 2009, 21: 4796-4802.
[155] Zhang S, Shao YY, Liao HG, Liu J, Aksay IA, Yin GP, Lin YH. Graphene Decorated with PtAu Alloy Nanoparticles: Facile Synthesis and Promising Application for Formic Acid Oxidation. *Chem Mater*. 2011, 23: 1079-1081.
[156] Xu C, Wang X, Zhu JW. Graphene-Metal Particle Nanocomposites. *J Phys Chem C*. 2008, 112: 19841-19845.
[157] Jasuja K, Linn J, Melton S, Berry V. Microwave-Reduced Uncapped Metal Nanoparticles on Graphene: Tuning Catalytic, Electrical, and Raman Properties. *J Phys Chem Lett*. 2010, 1: 1853-1860.
[158] Gao HC, Xiao F, Ching CB, Duan HW. One-Step Electrochemical Synthesis of PtNi Nanoparticle-Graphene Nanocomposites for Nonenzymatic Amperometric Glucose Detection. *ACS Appl Mater Interfaces*. 2011, 3: 3049-3057.
[159] Compton RG, Eklund JC, Marken F, Rebbitt TO, Akkermans RP, Waller DN. Dual activation: coupling ultrasound to electrochemistry - an overview. *Electrochim Acta*. 1997, 42: 2919-2927.
[160] Tang XZ, Cao ZW, Zhang HB, Liu J, Yu ZZ. Growth of silver nanocrystals on graphene by simultaneous reduction of graphene oxide and silver ions with a rapid and efficient one-step approach. *Chem Commun*. 2011, 47: 3084-3086.
[161] Vinodgopal K, Neppolian B, Lightcap IV, Grieser F, Ashokkumar M, Kamat PV. Sonolytic Design of Graphene-Au Nanocomposites. Simultaneous and Sequential Reduction of Graphene Oxide and Au(III). *J Phys Chem Lett*. 2010, 1: 1987-1993.
[162] Guo SJ, Wen D, Zhai YM, Dong SJ, Wang EK. Platinum Nanoparticle Ensemble-on-Graphene Hybrid Nanosheet: One-Pot, Rapid Synthesis, and Used as New Electrode Material for Electrochemical Sensing. *ACS Nano*. 2010, 4: 3959-3968.

[163] Guo HL, Wang XF, Qian QY, Wang FB, Xia XH. A Green Approach to the Synthesis of Graphene Nanosheets. *ACS Nano*. 2009, 3: 2653-2659.
[164] Wan D, Yuan SJ, Li GL, Neoh KG, Kang ET. Glucose Biosensor from Covalent Immobilization of Chitosan-Coupled Carbon Nanotubes on Polyaniline-Modified Gold Electrode. *ACS Appl Mater Interfaces*. 2010, 2: 3083-3091.
[165] Yehezkeli O, Tel-Vered R, Reichlin S, Willner I. Nano-engineered Flavin-Dependent Glucose Dehydrogenase/Gold Nanoparticle-Modified Electrodes for Glucose Sensing and Biofuel Cell Applications. *ACS Nano*. 2011, 5: 2385-2391.
[166] Uehara H, Kakiage M, Sekiya M, Sakuma D, Yamonobe T, Takano N, Barraud A, Meurville E, Ryser P. Size-Selective Diffusion in Nanoporous but Flexible Membranes for Glucose Sensors. *ACS Nano*. 2009, 3: 924-932.
[167] Lu J, Do I, Drzal LT, Worden RM, Lee I. Nanometal-decorated exfoliated graphite nanoplatelet based glucose biosensors with high sensitivity and fast response. *ACS Nano*. 2008, 2: 1825-1832.
[168] Cheng TM, Huang TK, Lin HK, Tung SP, Chen YL, Lee CY, Chiu HT. (110)-Exposed Gold Nanocoral Electrode as Low Onset Potential Selective Glucose Sensor. *ACS Appl Mater Interfaces*. 2010, 2: 2773-2780.
[169] Fang B, Gu AX, Wang GF, Wang W, Feng YH, Zhang CH, Zhang XJ. Silver Oxide Nanowalls Grown on Cu Substrate as an Enzymeless Glucose Sensor. *ACS Appl Mater Interfaces*. 2009, 1: 2829-2834.
[170] Jena BK, Raj CR. Enzyme-free amperometric sensing of glucose by using gold nanoparticles. *Chem-Eur J*. 2006, 12: 2702-2708.
[171] Wang JP, Thomas DF, Chen AC. Nonenzymatic electrochemical glucose sensor based on nanoporous PtPb networks. *Anal Chem*. 2008, 80: 997-1004.
[172] Park S, Chung TD, Kim HC. Nonenzymatic glucose detection using mesoporous platinum. *Anal Chem*. 2003, 75: 3046-3049.
[173] Song YY, Zhang D, Gao W, Xia XH. Nonenzymatic glucose detection by using a three-dimensionally ordered, macroporous platinum template. *Chem-Eur J*. 2005, 11: 2177-2182.
[174] Yuan JH, Wang K, Xia XH. Highly ordered platinum-nanotubule arrays for amperometric glucose sensing. *Adv Funct Mater*. 2005, 15: 803-809.
[175] Shen QM, Jiang LP, Zhang H, Min QH, Hou WH, Zhu JJ. Three-dimensional Dendritic Pt Nanostructures: Sonoelectrochemical Synthesis and Electrochemical Applications. *J Phys Chem C*. 2008, 112: 16385-16392.
[176] Cui HF, Ye JS, Zhang WD, Li CM, Luong JHT, Sheu FS. Selective and sensitive electrochemical detection of glucose in neutral solution using platinum-lead alloy nanoparticle/carbon nanotube nanocomposites. *Anal Chim Acta*. 2007, 594: 175-183.
[177] Bai Y, Sun YY, Sun CQ. Pt-Pb nanowire array electrode for enzyme-free glucose detection. *Biosens Bioelectron*. 2008, 24: 579-585.
[178] Holt-Hindle P, Nigro S, Asmussen M, Chen AC. Amperometric glucose sensor based on platinum-iridium nanomaterials. *Electrochem Commun*. 2008, 10: 1438-1441.
[179] Xiao F, Zhao FQ, Mei DP, Mo ZR, Zeng BZ. Nonenzymatic glucose sensor based on ultrasonic-electrode position of bimetallic PtM (M = Ru, Pd and Au) nanoparticles on carbon nanotubes-ionic liquid composite film. *Biosens Bioelectron*. 2009, 24: 3481-3486.

[180] Xiao F, Zhao FQ, Zhang YF, Guo GP, Zeng BZ. Ultrasonic Electrodeposition of Gold-Platinum Alloy Nanoparticles on Ionic Liquid-Chitosan Composite Film and Their Application in Fabricating Nonenzyme Hydrogen Peroxide Sensors. *J Phys Chem C*. 2009, 113: 849-855.
[181] Yang D, Velamakanni A, Bozoklu G, Park S, Stoller M, Piner RD, Stankovich S, Jung I, Field DA, Ventrice CA, Ruoff RS. Chemical analysis of graphene oxide films after heat and chemical treatments by X-ray photoelectron and Micro-Raman spectroscopy. *Carbon*. 2009, 47: 145-152.
[182] Xiao F, Mo ZR, Zhao FQ, Zeng BZ. Ultrasonic-electrodeposition of gold-platinum alloy nanoparticles on multi-walled carbon nanotubes - ionic liquid composite film and their electrocatalysis towards the oxidation of nitrite. *Electrochem Commun*. 2008, 10: 1740-1743.
[183] Geim AK, Novoselov KS. The rise of graphene. *Nat Mater*. 2007, 6: 183-191.
[184] Sen F, Gokagac G. Different sized platinum nanoparticles supported on carbon: An XPS study on these methanol oxidation catalysts. *J Phys Chem C*. 2007, 111: 5715-5720.
[185] Xiao F, Zhao FQ, Zeng JJ, Zeng BZ. Novel alcohol sensor based on PtRuNi ternary alloy nanoparticles-multi-walled carbon nanotube-ionic liquid composite coated electrode. *Electrochem Commun*. 2009, 11: 1550-1553.
[186] Radmilovic V, Gasteiger HA, Ross PN. Structure and Chemical Composition of a Supported Pt-Ru Electrocatalyst for Methanol Oxidation. *J Catal*. 1995, 154: 98-106.
[187] Babu PK, Kim HS, Oldfield E, Wieckowski A. Electronic alterations caused by ruthenium in Pt-Ru alloy nanoparticles as revealed by electrochemical NMR. *J Phys Chem B*. 2003, 107: 7595-7600.
[188] Shao YY, Liu J, Wang Y, Lin YH. Novel catalyst support materials for PEM fuel cells: current status and future prospects. *J Mater Chem*. 2009, 19: 46-59.
[189] Girishkumar G, Hall TD, Vinodgopal K, Kamat PV. Single wall carbon nanotube supports for portable direct methanol fuel cells. *J Phys Chem B*. 2006, 110: 107-114.
[190] Yin WX, Li ZP, Zhu JK, Qin HY. Effects of NaOH addition on performance of the direct hydrazine fuel cell. *J Power Sources*. 2008, 182: 520-523.
[191] Bard AJ. Chronopotentiometric Oxidation of Hydrazine at a Platinum Electrode. *Anal Chem*. 1963, 35: 1602-1607.
[192] Evans GE, Kordesch KV. Hydrazine-air fuel cells. Hydrazine-air fuel cells emerge from the laboratory. *Science*. 1967, 158: 1148-1152.
[193] Yamada K, Asazawa K, Yasuda K, Ioroi T, Tanaka H, Miyazaki Y, Kobayashi T. Investigation of PEM type direct hydrazine fuel cell. *J Power Sources*. 2003, 115: 236-242.
[194] Asazawa K, Yamada K, Tanaka H, Taniguchi M, Oguro K. Electrochemical oxidation of hydrazine and its derivatives on the surface of metal electrodes in alkaline media. *J Power Sources*. 2009, 191: 362-365.
[195] Sakamoto T, Asazawa K, Yamada K, Tanaka H. Study of Pt-free anode catalysts for anion exchange membrane fuel cells. *Catal Today*. 2011, 164: 181-185.

[196] Rees NV, Compton RG. Carbon-free energy: a review of ammonia- and hydrazine-based electrochemical fuel cells. *Energy Environ Sci*. 2011, 4: 1255-1260.
[197] Serov A, Kwak C. Direct hydrazine fuel cells: A review. *Appl Catal B: Environ*. 2010, 98: 1-9.
[198] Asazawa K, Yamada K, Tanaka H, Oka A, Taniguchi M, Kobayashi T. A platinum-free zero-carbon-emission easy fuelling direct hydrazine fuel cell for vehicles. *Angew Chem, Int Ed*. 2007, 46: 8024-8027.
[199] Ramesh P, Itkis ME, Tang JM, Haddon RC. SWNT-MWNT hybrid architecture for proton exchange membrane fuel cell cathodes. *J Phys Chem C*. 2008, 112: 9089-9094.
[200] Seger B, Kamat PV. Electrocatalytically Active Graphene-Platinum Nanocomposites. Role of 2-D Carbon Support in PEM Fuel Cells. *J Phys Chem C*. 2009, 113: 7990-7995.
[201] Girishkumar G, Vinodgopal K, Kamat PV. Carbon nanostructures in portable fuel cells: Single-walled carbon nanotube electrodes for methanol oxidation and oxygen reduction. *J Phys Chem B*. 2004, 108: 19960-19966.
[202] Xie X, Ye M, Hu LB, Liu N, McDonough JR, Chen W, Alshareef HN, Criddle CS, Cui Y. Carbon nanotube-coated macroporous sponge for microbial fuel cell electrodes. *Energy Environ Sci*. 2012, 5: 5265-5270.
[203] Chen AC, Holt-Hindle P. Platinum-Based Nanostructured Materials: Synthesis, Properties, and Applications. *Chem Rev*. 2010, 110: 3767-3804.
[204] Zhu W, Zeng CC, Zheng JP, Liang R, Zhang C, Wang B. Preparation of Buckypaper Supported Pt Catalyst for PEMFC Using a Supercritical Fluid Method. *Electrochem Solid State Lett*. 2011, 14: B81-B83.
[205] Kim J, Lee SW, Hammond PT, Shao-Horn Y. Electrostatic Layer-by-Layer Assembled Au Nano particle/MWNT Thin Films: Microstructure, Optical Property, and Electrocatalytic Activity for Methanol Oxidation. *Chem Mater*. 2009, 21: 2993-3001.
[206] Wang SY, Iyyamperumal E, Roy A, Xue YH, Yu DS, Dai LM. Vertically Aligned BCN Nanotubes as Efficient Metal-Free Electrocatalysts for the Oxygen Reduction Reaction: A Synergetic Effect by Co-Doping with Boron and Nitrogen. *Angew Chem, Int Ed*. 2011, 50: 11756-11760.
[207] Davies A, Audette P, Farrow B, Hassan F, Chen ZW, Choi JY, Yu AP. Graphene-Based Flexible Supercapacitors: Pulse-Electropolymerization of Polypyrrole on Free-Standing Graphene Films. *J Phys Chem C*. 2011, 115: 17612-17620.
[208] Yang XW, Zhu JW, Qiu L, Li D. Bioinspired Effective Prevention of Restacking in Multilayered Graphene Films: Towards the Next Generation of High-Performance Supercapacitors. *Adv Mater*. 2011, 23: 2833-2838.
[209] Zhao X, Hayner CM, Kung MC, Kung HH. In-Plane Vacancy-Enabled High-Power Si-Graphene Composite Electrode for Lithium-Ion Batteries. *Adv Energy Mater*. 2011, 1: 1079-1084.
[210] Ferrin P, Mavrikakis M. Structure Sensitivity of Methanol Electrooxidation on Transition Metals. *J Am Chem Soc*. 2009, 131: 14381-14389.
[211] Ye LQ, Li ZP, Qin HY, Zhu JK, Liu BH. Hydrazine electrooxidation on a composite catalyst consisting of nickel and palladium. *J Power Sources*. 2011, 196: 956-961.

[212] Gao HC, Wang YX, Xiao F, Ching CB, Duan HW. Growth of Copper Nanocubes on Graphene Paper as Free-Standing Electrodes for Direct Hydrazine Fuel Cells. *J Phys Chem C*. 2012, 116: 7719-7725.
[213] Yang J, Jiang LC, Zhang WD, Gunasekaran S. A highly sensitive non-enzymatic glucose sensor based on a simple two-step electrodeposition of cupric oxide (CuO) nanoparticles onto multi-walled carbon nanotube arrays. *Talanta*. 2010, 82: 25-33.
[214] Zhu W, Ku D, Zheng JP, Liang Z, Wang B, Zhang C, Walsh S, Au G, Plichta EJ. Buckypaper-based catalytic electrodes for improving platinum utilization and PEMFC's performance. *Electrochim Acta*. 2010, 55: 2555-2560.
[215] Kang XH, Mai ZB, Zou XY, Cai PX, Mo JY. A sensitive nonenzymatic glucose sensor in alkaline media with a copper nanocluster/multiwall carbon nano tube-modified glassy carbon electrode. *Anal Biochem*. 2007, 363: 143-150.
[216] Suni, II. Impedance methods for electrochemical sensors using nanomaterials. *Trac-Trends in Analytical Chemistry*. 2008, 27: 604-611.
[217] Zhou GM, Wang DW, Li F, Zhang LL, Li N, Wu ZS, Wen L, Lu GQ, Cheng HM. Graphene-Wrapped Fe3O4 Anode Material with Improved Reversible Capacity and Cyclic Stability for Lithium Ion Batteries. *Chem Mater*. 2010, 22: 5306-5313.
[218] Sanabria-Chinchilla J, Asazawa K, Sakamoto T, Yamada K, Tanaka H, Strasser P. Noble Metal-Free Hydrazine Fuel Cell Catalysts: EPOC Effect in Competing Chemical and Electrochemical Reaction Pathways. *J Am Chem Soc*. 2011, 133: 5425-5431.
[219] Ding Y, Wang Y, Zhang LC, Zhang H, Li CM, Lei Y. Preparation of TiO2-Pt hybrid nanofibers and their application for sensitive hydrazine detection. *Nanoscale*. 2011, 3: 1149-1157.
[220] Wang GF, Zhang CH, He XP, Li ZJ, Zhang XJ, Wang L, Fang B. Detection of hydrazine based on Nano-Au deposited on Porous-TiO2 film. *Electrochim Acta*. 2010, 55: 7204-7210.
[221] Ye WC, Yang B, Cao GY, Duan L, Wang CM. Electrocatalytic oxidation of hydrazine compound on electroplated Pd/WO3 film. *Thin Solid Films*. 2008, 516: 2957-2961.
[222] Ding Y, Hou CH, Li BK, Lei Y. Sensitive Hydrazine Detection Using a Porous Mn2O3 Nanofibers-Based Sensor. *Electroanalysis*. 2011, 23: 1245-1251.
[223] Sljukic B, Banks CE, Crossley A, Compton RG. Iron(III) oxide graphite composite electrodes: Application to the electroanalytical detection of hydrazine and hydrogen peroxide. *Electroanalysis*. 2006, 18: 1757-1762.
[224] Tominaka S, Nishizeko H, Mizuno J, Osaka T. Bendable fuel cells: on-chip fuel cell on a flexible polymer substrate. *Energy Environ Sci*. 2009, 2: 1074-1077.
[225] Gelves GA, Murakami ZTM, Krantz MJ, Haber JA. Multigram synthesis of copper nanowires using ac electrodeposition into porous aluminium oxide templates. *J Mater Chem*. 2006, 16: 3075-3083.
[226] Gonzalez S, Perez M, Barrera M, Elipe ARG, Souto RM. Mechanism of copper passivation in aqueous sodium carbonate-bicarbonate solution derived from combined X-ray photoelectron spectroscopic and electrochemical data. *J Phys Chem B*. 1998, 102: 5483-5489.

[227] Yin ZJ, Liu LP, Yang ZS. An amperometric sensor for hydrazine based on nano-copper oxide modified electrode. *J Solid State Electrochem*. 2011, 15: 821-827.
[228] Le WZ, Liu YQ. Preparation of nano-copper oxide modified glassy carbon electrode by a novel film plating/potential cycling method and its characterization. *Sens Actuator B-Chem*. 2009, 141: 147-153.
[229] Karim-Nezhad G, Jafarloo R, Dorraji PS. Copper (hydr)oxide modified copper electrode for electrocatalytic oxidation of hydrazine in alkaline media. *Electrochim Acta*. 2009, 54: 5721-5726.
[230] Koper MTM. Temperature dependence of the transfer coefficient of simple electrochemical redox reactions due to slow solvent dynamics. *J Phys Chem B*. 1997, 101: 3168-3173.
[231] Devanath MAV. Kinetics of multiple-electron-transfer reactions. 1. The transfer coefficient. *Electrochim Acta*. 1972, 17: 1683-1697.
[232] Guo DJ, Li HL. High dispersion and electrocatalytic properties of palladium nanoparticles on single-walled carbon nanotubes. *J Colloid Interface Sci*. 2005, 286: 274-279.
[233] Xiao F, Zhao FQ, Li JW, Yan R, Yu JJ, Zeng BZ. Sensitive voltammetric determination of chloramphenicol by using single-wall carbon nanotube-gold nanoparticle-ionic liquid composite film modified glassy carbon electrodes. *Anal Chim Acta*. 2007, 596: 79-85.
[234] Aldous L, Compton RG. The mechanism of hydrazine electro-oxidation revealed by platinum microelectrodes: role of residual oxides. *Phys Chem Chem Phys*. 2011, 13: 5279-5287.
[235] Ferreira PJ, la O GJ, Shao-Horn Y, Morgan D, Makharia R, Kocha S, Gasteiger HA. Instability of Pt/C electrocatalysts in proton exchange membrane fuel cells - A mechanistic investigation. *J Electrochem Soc*. 2005, 152: A2256-A2271.
[236] Strehblow HH, Titze B. The investigation of the passive behaviour of copper in weakly acid and alkaline solutions and the examination of the passive film by ESCA and ISS. *Electrochim Acta*. 1980, 25: 839-850.
[237] Nyholm L, Nystrom G, Mihranyan A, Stromme M. Toward Flexible Polymer and Paper-Based Energy Storage Devices. *Adv Mater*. 2011, 23: 3751-3769.
[238] Liu F, Song SY, Xue DF, Zhang HJ. Folded Structured Graphene Paper for High Performance Electrode Materials. *Adv Mater*. 2012, 24: 1089-1094.
[239] Meng CZ, Liu CH, Chen LZ, Hu CH, Fan SS. Highly Flexible and All-Solid-State Paper like Polymer Supercapacitors. *Nano Lett*. 2010, 10: 4025-4031.
[240] Kang YJ, Chun SJ, Lee SS, Kim BY, Kim JH, Chung H, Lee SY, Kim W. All-Solid-State Flexible Supercapacitors Fabricated with Bacterial Nanocellulose Papers, Carbon Nanotubes, and Triblock-Copolymer Ion Gels. *ACS Nano*. 2012, 6: 6400-6406.
[241] Yuan LY, Lu XH, Xiao X, Zhai T, Dai JJ, Zhang FC, Hu B, Wang X, Gong L, Chen J, Hu CG, Tong YX, Zhou J, Wang ZL. Flexible Solid-State Supercapacitors Based on Carbon Nanoparticles/MnO2 Nanorods Hybrid Structure. *ACS Nano*. 2012, 6: 656-661.
[242] Choi BG, Hong J, Hong WH, Hammond PT, Park H. Facilitated Ion Transport in All-Solid-State Flexible Supercapacitors. *ACS Nano*. 2011, 5: 7205-7213.

[243] Hall PJ, Mirzaeian M, Fletcher SI, Sillars FB, Rennie AJR, Shitta-Bey GO, Wilson G, Cruden A, Carter R. Energy storage in electrochemical capacitors: designing functional materials to improve performance. *Energy Environ Sci*. 2010, 3: 1238-1251.
[244] Choudhury NA, Sampath S, Shukla AK. Hydrogel-polymer electrolytes for electrochemical capacitors: an overview. *Energy Environ Sci*. 2009, 2: 55-67.
[245] Pell WG, Conway BE. Peculiarities and requirements of asymmetric capacitor devices based on combination of capacitor and battery-type electrodes. *J Power Sources*. 2004, 136: 334-345.
[246] Long JW, Belanger D, Brousse T, Sugimoto W, Sassin MB, Crosnier O. Asymmetric electrochemical capacitors-Stretching the limits of aqueous electrolytes. *MRS Bull*. 2011, 36: 513-522.
[247] Zhang JT, Zhao XS. On the Configuration of Supercapacitors for Maximizing Electrochemical Performance. *ChemSusChem*. 2012, 5: 818-841.
[248] Hu LB, Chen W, Xie X, Liu NA, Yang Y, Wu H, Yao Y, Pasta M, Alshareef HN, Cui Y. Symmetrical MnO2-Carbon Nanotube-Textile Nanostructures for Wearable Pseudocapacitors with High Mass Loading. *ACS Nano*. 2011, 5: 8904-8913.
[249] Bao LH, Zang JF, Li XD. Flexible Zn2SnO4/MnO4 Core/Shell Nanocable-Carbon Microfiber Hybrid Composites for High-Performance Supercapacitor Electrodes. *Nano Lett*. 2011, 11: 1215-1220.
[250] Zheng GY, Hu LB, Wu H, Xie X, Cui Y. Paper supercapacitors by a solvent-free drawing method. *Energy Environ Sci*. 2011, 4: 3368-3373.
[251] Wang GP, Zhang L, Zhang JJ. A review of electrode materials for electrochemical supercapacitors. *Chem Soc Rev*. 2012, 41: 797-828.
[252] Frackowiak E. Carbon materials for supercapacitor application. *Phys Chem Chem Phys*. 2007, 9: 1774-1785.
[253] Simon P, Gogotsi Y. Materials for electrochemical capacitors. *Nat Mater*. 2008, 7: 845-854.
[254] Sun YQ, Wu Q, Shi GQ. Graphene based new energy materials. *Energy Environ Sci*. 2011, 4: 1113-1132.
[255] Huang Y, Liang JJ, Chen YS. An Overview of the Applications of Graphene-Based Materials in Supercapacitors. *Small*. 2012, 8: 1805-1834.
[256] Dai LM, Chang DW, Baek JB, Lu W. Carbon Nanomaterials for Advanced Energy Conversion and Storage. *Small*. 2012, 8: 1130-1166.
[257] Zhao X, Zhang LL, Murali S, Stoller MD, Zhang QH, Zhu YW, Ruoff RS. Incorporation of manganese dioxide within ultraporous activated graphene for high-performance electrochemical capacitors. *ACS Nano*. 2012, 6: 5404-5412.
[258] Lee JW, Hall AS, Kim JD, Mallouk TE. A Facile and Template-Free Hydrothermal Synthesis of Mn3O4 Nanorods on Graphene Sheets for Supercapacitor Electrodes with Long Cycle Stability. *Chem Mater*. 2012, 24: 1158-1164.
[259] Lu XH, Zheng DZ, Zhai T, Liu ZQ, Huang YY, Xie SL, Tong YX. Facile synthesis of large-area manganese oxide nanorod arrays as a high-performance electrochemical supercapacitor. *Energy Environ Sci*. 2011, 4: 2915-2921.
[260] Zhang LL, Zhao X, Stoller MD, Zhu YW, Ji HX, Murali S, Wu YP, Perales S, Clevenger B, Ruoff RS. Highly Conductive and Porous Activated

Reduced Graphene Oxide Films for High-Power Supercapacitors. *Nano Lett*. 2012, 12: 1806-1812.
[261] Luo JY, Jang HD, Huang JX. Effect of Sheet Morphology on the Scalability of Graphene-Based Ultracapacitors. *ACS Nano*. 2013, 7: 1464-1471.
[262] Chen J, Sheng KX, Luo PH, Li C, Shi GQ. Graphene Hydrogels Deposited in Nickel Foams for High-Rate Electrochemical Capacitors. *Adv Mater*. 2012, 24: 4569-4573.
[263] Wu ZS, Ren WC, Wang DW, Li F, Liu BL, Cheng HM. High-Energy MnO2 Nanowire/Graphene and Graphene Asymmetric Electrochemical Capacitors. *ACS Nano*. 2010, 4: 5835-5842.
[264] Chen Z, Augustyn V, Wen J, Zhang YW, Shen MQ, Dunn B, Lu YF. High-Performance Supercapacitors Based on Intertwined CNT/V2O5 Nanowire Nanocomposites. *Adv Mater*. 2011, 23: 791-795.
[265] Chen PC, Shen GZ, Shi Y, Chen HT, Zhou CW. Preparation and Characterization of Flexible Asymmetric Supercapacitors Based on Transition-Metal-Oxide Nanowire/Single-Walled Carbon Nanotube Hybrid Thin-Film Electrodes. *ACS Nano*. 2010, 4: 4403-4411.
[266] Choi BG, Chang SJ, Kang HW, Park CP, Kim HJ, Hong WH, Lee S, Huh YS. High performance of a solid-state flexible asymmetric supercapacitor based on graphene films. *Nanoscale*. 2012, 4: 4983-4988.
[267] Gao HC, Xiao F, Ching CB, Duan HW. Flexible All-Solid-State Asymmetric Supercapacitors Based on Free-Standing Carbon Nanotube/Graphene and Mn3O4 Nanoparticle/Graphene Paper Electrodes. *ACS Appl Mater Interfaces*. 2012, 4: 7019-7025.
[268] Yu AP, Su CCL, Roes I, Fan B, Haddon RC. Gram-Scale Preparation of Surfactant-Free, Carboxylic Acid Groups Functionalized, Individual Single-Walled Carbon Nanotubes in Aqueous Solution. *Langmuir*. 2010, 26: 1221-1225.
[269] Hao XL, Zhao JZ, Li YL, Zhao Y, Ma DC, Li LZ. Mild aqueous synthesis of octahedral Mn3O4 nanocrystals with varied oxidation states. *Colloid Surf A: Physicochem Eng Asp*. 2011, 374: 42-47.
[270] Lee KT, Wu NL. Manganese oxide electrochemical capacitor with potassium poly(acrylate) hydrogel electrolyte. *J Power Sources*. 2008, 179: 430-434.
[271] Stoller MD, Ruoff RS. Best practice methods for determining an electrode material's performance for ultracapacitors. *Energy Environ Sci*. 2010, 3: 1294-1301.
[272] Brousse T, Toupin M, Belanger D. A hybrid activated carbon-manganese dioxide capacitor using a mild aqueous electrolyte. *J Electrochem Soc*. 2004, 151: A614-A622.
[273] Gao HC, Xiao F, Ching CB, Duan HW. High-Performance Asymmetric Supercapacitor Based on Graphene Hydrogel and Nanostructured MnO2. *ACS Appl Mater Interfaces*. 2012, 4: 2801-2810.
[274] Park S, An JH, Jung IW, Piner RD, An SJ, Li XS, Velamakanni A, Ruoff RS. Colloidal Suspensions of Highly Reduced Graphene Oxide in a Wide Variety of Organic Solvents. *Nano Lett*. 2009, 9: 1593-1597.
[275] Aboutalebi SH, Chidembo AT, Salari M, Konstantinov K, Wexler D, Liu HK, Dou SX. Comparison of GO, GO/MWCNTs composite and MWCNTs as potential electrode materials for supercapacitors. *Energy Environ Sci*. 2011, 4: 1855-1865.

[276] Huang ZD, Zhang BA, Oh SW, Zheng QB, Lin XY, Yousefi N, Kim JK. Self-assembled reduced graphene oxide/carbon nanotube thin films as electrodes for supercapacitors. *J Mater Chem*. 2012, 22: 3591-3599.
[277] Cote LJ, Kim J, Tung VC, Luo JY, Kim F, Huang JX. Graphene oxide as surfactant sheets. *Pure Appl Chem*. 2011, 83: 95-110.
[278] Khan U, O'Connor I, Gun'ko YK, Coleman JN. The preparation of hybrid films of carbon nanotubes and nano-graphite/graphene with excellent mechanical and electrical properties. *Carbon*. 2010, 48: 2825-2830.
[279] Wang Y, Shi ZQ, Huang Y, Ma YF, Wang CY, Chen MM, Chen YS. Supercapacitor Devices Based on Graphene Materials. *J Phys Chem C*. 2009, 113: 13103-13107.
[280] Murray JW. The surface chemistry of hydrous manganese dioxide. *J Colloid Interface Sci*. 1974, 46: 357-371.
[281] Wang GK, Sun X, Lu FY, Sun HT, Yu MP, Jiang WL, Liu CS, Lian J. Flexible pillared graphene-paper electrodes for high-performance electrochemical supercapacitors. *Small*. 2012, 8: 452-459.
[282] Cheng YW, Lu ST, Zhang HB, Varanasi CV, Liu J. Synergistic Effects from Graphene and Carbon Nanotubes Enable Flexible and Robust Electrodes for High-Performance Supercapacitors. *Nano Lett*. 2012, 12: 4206-4211.
[283] Fan ZJ, Yan J, Wei T, Zhi LJ, Ning GQ, Li TY, Wei F. Asymmetric Supercapacitors Based on Graphene/MnO2 and Activated Carbon Nanofiber Electrodes with High Power and Energy Density. *Adv Funct Mater*. 2011, 21: 2366-2375.
[284] Khomenko V, Raymundo-Pinero E, Frackowiak E, Beguin F. High-voltage asymmetric supercapacitors operating in aqueous electrolyte. *Appl Phys A: Mater Sci Process*. 2006, 82: 567-573.
[285] Wang YT, Lu AH, Zhang HL, Li WC. Synthesis of Nanostructured Mesoporous Manganese Oxides with Three-Dimensional Frameworks and Their Application in Supercapacitors. *J Phys Chem C*. 2011, 115: 5413-5421.
[286] Qu QT, Shi Y, Tian S, Chen YH, Wu YP, Holze R. A new cheap asymmetric aqueous supercapacitor: Activated carbon//NaMnO2. *J Power Sources*. 2009, 194: 1222-1225.
[287] Cottineau T, Toupin M, Delahaye T, Brousse T, Belanger D. Nanostructured transition metal oxides for aqueous hybrid electrochemical supercapacitors. *Appl Phys A: Mater Sci Process*. 2006, 82: 599-606.
[288] Yu GH, Hu LB, Vosgueritchian M, Wang HL, Xie X, McDonough JR, Cui X, Cui Y, Bao ZN. Solution-Processed Graphene/MnO2 Nanostructured Textiles for High-Performance Electrochemical Capacitors. *Nano Lett*. 2011, 11: 2905-2911.
[289] Deng LJ, Zhu G, Wang JF, Kang LP, Liu ZH, Yang ZP, Wang ZL. Graphene-MnO2 and graphene asymmetrical electrochemical capacitor with a high energy density in aqueous electrolyte. *J Power Sources*. 2011, 196: 10782-10787.
[290] Kotz R, Carlen M. Principles and applications of electrochemical capacitors. *Electrochim Acta*. 2000, 45: 2483-2498.
[291] Lee SW, Gallant BM, Byon HR, Hammond PT, Shao-Horn Y. Nanostructured carbon-based electrodes: bridging the gap between thin-film lithium-ion batteries and electrochemical capacitors. *Energy Environ Sci*. 2011, 4: 1972-1985.

[292] Zhang LL, Zhou R, Zhao XS. Graphene-based materials as supercapacitor electrodes. *J Mater Chem*. 2010, 20: 5983-5992.
[293] Du F, Yu DS, Dai LM, Ganguli S, Varshney V, Roy AK. Preparation of Tunable 3D Pillared Carbon Nanotube-Graphene Networks for High-Performance Capacitance. *Chem Mater*. 2011, 23: 4810-4816.
[294] Chen Y, Zhang XO, Zhang DC, Yu P, Ma YW. High performance supercapacitors based on reduced graphene oxide in aqueous and ionic liquid electrolytes. *Carbon*. 2011, 49: 573-580.
[295] Vivekchand SRC, Rout CS, Subrahmanyam KS, Govindaraj A, Rao CNR. Graphene-based electrochemical supercapacitors. *J Chem Sci*. 2008, 120: 9-13.
[296] Wang YG, Xia YY. A new concept hybrid electrochemical surpercapacitor: Carbon/LiMn2O4 aqueous system. *Electrochem Commun*. 2005, 7: 1138-1142.
[297] Zhao X, Sanchez BM, Dobson PJ, Grant PS. The role of nanomaterials in redox-based supercapacitors for next generation energy storage devices. *Nanoscale*. 2011, 3: 839-855.
[298] Demarconnay L, Raymundo-Pinero E, Beguin F. Adjustment of electrodes potential window in an asymmetric carbon/MnO2 supercapacitor. *J Power Sources*. 2011, 196: 580-586.
[299] Conway BE, Pell WG. Double-layer and pseudocapacitance types of electrochemical capacitors and their applications to the development of hybrid devices. *J Solid State Electrochem*. 2003, 7: 637-644.
[300] Zhang JT, Jiang JW, Li HL, Zhao XS. A high-performance asymmetric supercapacitor fabricated with graphene-based electrodes. *Energy Environ Sci*. 2011, 4: 4009-4015.
[301] Jiang H, Li CZ, Sun T, Ma J. A green and high energy density asymmetric supercapacitor based on ultrathin MnO2 nanostructures and functional mesoporous carbon nanotube electrodes. *Nanoscale*. 2012, 4: 807-812.
[302] Mishra AK, Ramaprabhu S. Functionalized Graphene-Based Nanocomposites for Supercapacitor Application. *J Phys Chem C*. 2011, 115: 14006-14013.
[303] Qu QT, Zhang P, Wang B, Chen YH, Tian S, Wu YP, Holze R. Electrochemical Performance of MnO2 Nanorods in Neutral Aqueous Electrolytes as a Cathode for Asymmetric Supercapacitors. *J Phys Chem C*. 2009, 113: 14020-14027.
[304] Ghodbane O, Pascal JL, Favier F. Microstructural Effects on Charge-Storage Properties in MnO2-Based Electrochemical Supercapacitors. *ACS Appl Mater Interfaces*. 2009, 1: 1130-1139.
[305] Chou SL, Wang JZ, Chew SY, Liu HK, Dou SX. Electrodeposition of MnO2 nanowires on carbon nanotube paper as free-standing, flexible electrode for supercapacitors. *Electrochem Commun*. 2008, 10: 1724-1727.
[306] Wei WF, Cui XW, Chen WX, Ivey DG. Manganese oxide-based materials as electrochemical supercapacitor electrodes. *Chem Soc Rev*. 2011, 40: 1697-1721.
[307] Wu MS, Chiang PCJ. Fabrication of nanostructured manganese oxide electrodes for electrochemical capacitors. *Electrochem Solid State Lett*. 2004, 7: A123-A126.

[308] Wei WF, Cui XW, Mao XH, Chen WX, Ivey DG. Morphology evolution in anodically electrodeposited manganese oxide nanostructures for electrochemical supercapacitor applications-Effect of supersaturation ratio. *Electrochim Acta*. 2011, 56: 1619-1628.
[309] Zhao DD, Yang Z, Zhang LY, Feng XL, Zhang YF. Electrodeposited Manganese Oxide on Nickel Foam-Supported Carbon Nanotubes for Electrode of Supercapacitors. *Electrochem Solid State Lett*. 2011, 14: A93-A96.
[310] Wang YH, Zhitomirsky I. Cathodic electrodeposition of Ag-doped manganese dioxide films for electrodes of electrochemical supercapacitors. *Mater Lett*. 2011, 65: 1759-1761.
[311] Liu DW, Zhang QF, Xiao P, Garcia BB, Guo Q, Champion R, Cao GZ. Hydrous manganese dioxide nanowall arrays growth and their Li+ ions intercalation electrochemical properties. *Chem Mater*. 2008, 20: 1376-1380.
[312] Bai H, Li C, Wang XL, Shi GQ. On the Gelation of Graphene Oxide. *J Phys Chem C*. 2011, 115: 5545-5551.
[313] Zhang XT, Sui ZY, Xu B, Yue SF, Luo YJ, Zhan WC, Liu B. Mechanically strong and highly conductive graphene aerogel and its use as electrodes for electrochemical power sources. *J Mater Chem*. 2011, 21: 6494-6497.
[314] Gao J, Liu F, Liu YL, Ma N, Wang ZQ, Zhang X. Environment-Friendly Method To Produce Graphene That Employs Vitamin C and Amino Acid. *Chem Mater*. 2010, 22: 2213-2218.
[315] Kulakov VA, Shishlyannikova NY, Virnik AD. IR spectroscopic study of structure of cellulose derivatives containing chemically bound antimicrobial compounds. *J Appl Spectrosc*. 1987, 46: 619-625.
[316] Moon IK, Lee J, Ruoff RS, Lee H. Reduced graphene oxide by chemical graphitization. *Nat Commun*. 2010, 1: 73.
[317] Xue LG, Hao H, Wei Z, Huang T, Yu AS. A hierarchical porous MnO2-based electrode for electrochemical capacitor. *J Solid State Electrochem*. 2011, 15: 485-491.
[318] Wang YL, Zhao YQ, Xu CL. May 3D nickel foam electrode be the promising choice for supercapacitors? *J Solid State Electrochem*. 2012, 16: 829-834.
[319] Xiao W, Xia H, Fuh JYH, Lu L. Electrochemical Synthesis and Supercapacitive Properties of epsilon-MnO2 with Porous/Nanoflaky Hierarchical Architectures. *J Electrochem Soc*. 2009, 156: A627-A633.
[320] Liu DW, Garcia BB, Zhang QF, Guo Q, Zhang YH, Sepehri S, Cao GZ. Mesoporous Hydrous Manganese Dioxide Nanowall Arrays with Large Lithium Ion Energy Storage Capacities. *Adv Funct Mater*. 2009, 19: 1015-1023.
[321] Kim CH, Akase Z, Zhang LC, Heuer AH, Newman AE, Hughes PJ. The structure and ordering of epsilon-MnO2. *J Solid State Chem*. 2006, 179: 753-774.
[322] Yuan YF, Xia XH, Wu JB, Yang JL, Chen YB, Guo SY. Nickel foam-supported porous Ni(OH)(2)/NiOOH composite film as advanced pseudocapacitor material. *Electrochim Acta*. 2011, 56: 2627-2632.
[323] Brousse T, Taberna PL, Crosnier O, Dugas R, Guillemet P, Scudeller Y, Zhou Y, Favier F, Belanger D, Simon P. Long-term cycling behavior of asymmetric activated carbon/MnO2 aqueous electrochemical supercapacitor. *J Power Sources*. 2007, 173: 633-641.

[324] Khomenko V, Raymundo-Pinero E, Beguin F. Optimisation of an asymmetric manganese oxide/activated carbon capacitor working at 2 V in aqueous medium. *J Power Sources*. 2006, 153: 183-190.
[325] Jin WH, Cao GT, Sun JY. Hybrid supercapacitor based on MnO2 and columned FeOOH using Li2SO4 electrolyte solution. *J Power Sources*. 2008, 175: 686-691.
[326] Qu QT, Li L, Tian S, Guo WL, Wu YP, Holze R. A cheap asymmetric supercapacitor with high energy at high power: Activated carbon//K(0.27)MnO(2) center dot 0.6H(2)O. *J Power Sources*. 2010, 195: 2789-2794.
[327] Fic K, Lota G, Meller M, Frackowiak E. Novel insight into neutral medium as electrolyte for high-voltage supercapacitors. *Energy Environ Sci*. 2012, 5: 5842-5850.
[328] Wang C, van der Vliet D, More KL, Zaluzec NJ, Peng S, Sun SH, Daimon H, Wang GF, Greeley J, Pearson J, Paulikas AP, Karapetrov G, Strmcnik D, Markovic NM, Stamenkovic VR. Multimetallic Au/FePt3 Nanoparticles as Highly Durable Electrocatalyst. *Nano Lett*. 2011, 11: 919-926.
[329] Cui CH, Li HH, Yu JW, Gao MR, Yu SH. Ternary Heterostructured Nanoparticle Tubes: A Dual Catalyst and Its Synergistic Enhancement Effects for O-2/H2O2 Reduction. *Angew Chem, Int Ed*. 2010, 49: 9149-9152.
[330] Hu LB, Cui Y. Energy and environmental nanotechnology in conductive paper and textiles. *Energy Environ Sci*. 2012, 5: 6423-6435.
[331] Xiao F, Li YQ, Gao HC, Ge SB, Duan HW. Growth of coral-like PtAu-MnO2 binary nanocomposites on free-standing graphene paper for flexible nonenzymatic glucose sensors. *Biosens Bioelectron*. 2013, 41: 417-423.
[332] Zan XL, Fang Z, Wu J, Xiao F, Huo FW, Duan HW. Freestanding graphene paper decorated with 2D-assembly of Au@Pt nanoparticles as flexible biosensors to monitor live cell secretion of nitric oxide. *Biosens Bioelectron*. 2013, 49: 71-78.
[333] Pushparaj VL, Shaijumon MM, Kumar A, Murugesan S, Ci L, Vajtai R, Linhardt RJ, Nalamasu O, Ajayan PM. Flexible energy storage devices based on nanocomposite paper. *Proc Natl Acad Sci U S A*. 2007, 104: 13574-13577.
[334] Jia XL, Chen Z, Suwarnasarn A, Rice L, Wang XL, Sohn H, Zhang Q, Wu BM, Wei F, Lu YF. High-performance flexible lithium-ion electrodes based on robust network architecture. *Energy Environ Sci*. 2012, 5: 6845-6849.
[335] Wang ZL, Xu D, Wang HG, Wu Z, Zhang XB. In Situ Fabrication of Porous Graphene Electrodes for High-Performance Energy Storage. *ACS Nano*. 2013, 7: 2422-2430.
[336] Kelly KF, Billups WE. Synthesis of of Soluble Graphite and Graphene. *Accounts Chem Res*. 2013, 46: 4-13.
[337] Zhang L, Liang JJ, Huang Y, Ma YF, Wang Y, Chen YS. Size-controlled synthesis of graphene oxide sheets on a large scale using chemical exfoliation. *Carbon*. 2009, 47: 3365-3368.
[338] Wu ZS, Ren WC, Gao LB, Liu BL, Jiang CB, Cheng HM. Synthesis of high-quality graphene with a pre-determined number of layers. *Carbon*. 2009, 47: 493-499.
[339] Ren PG, Yan DX, Ji X, Chen T, Li ZM. Temperature dependence of graphene oxide reduced by hydrazine hydrate. *Nanotechnology*. 2011, 22: 055705.

[340] Eigler S, Enzelberger-Heim M, Grimm S, Hofmann P, Kroener W, Geworski A, Dotzer C, Rockert M, Xiao J, Papp C, Lytken O, Steinruck HP, Muller P, Hirsch A. Wet chemical synthesis of graphene. *Adv Mater*. 2013, 25: 3583-3587.
[341] Huang X, Li SZ, Wu SX, Huang YZ, Boey F, Gan CL, Zhang H. Graphene Oxide-Templated Synthesis of Ultrathin or Tadpole-Shaped Au Nanowires with Alternating hcp and fcc Domains. *Adv Mater*. 2012, 24: 979-983.
[342] Xu J, Wang L, Zhu YF. Decontamination of Bisphenol A from Aqueous Solution by Graphene Adsorption. *Langmuir*. 2012, 28: 8418-8425.
[343] Sanchez VC, Jachak A, Hurt RH, Kane AB. Biological Interactions of Graphene-Family Nanomaterials: An Interdisciplinary Review. *Chem Res Toxicol*. 2012, 25: 15-34.